Enhanced Heat Transfer Catalyst Structures for Fischer-Tropsch Synthesis

by

Min Sheng

A dissertation submitted to the Graduate Faculty of
Auburn University
in partial fulfillment of the
requirements for the Degree of
Doctor of Philosophy

Auburn, Alabama
May 7, 2011

Keywords: Microfibrous entrapped catalyst, Fischer-Tropsch synthesis, Effective thermal conductivity, Packed bed, Computational fluid dynamics, Junction factor

Approved by

Bruce J. Tatarchuk, Chair, Professor of Chemical Engineering
Yoon Y. Lee, Professor of Chemical Engineering
William Ashurst, Professor of Chemical Engineering
Daniel Harris, Professor of Mechanical Engineering

Abstract

Highly exothermic catalytic reactions are problematic from a thermal management perspective and often dictate the type of reactor, heat exchanger, level of conversion/recycle and contacting schemes employed. Those reactions, such as Fischer-Tropsch synthesis (FTS), require catalyst beds with enhanced heat transfer characteristics. Novel catalyst structures, microfibrous entrapped catalyst (MFEC) structures, made of highly conductive metals were compared with traditional packed beds (PB) based on the experimental determinations of thermal parameters and performances in FTS process. Conductive metal MFECs had higher effective thermal conductivities and higher inside wall heat transfer coefficients than PBs including those made of pure copper particles. The radial effective thermal conductivity of copper MFEC was 56-fold higher than that of alumina PB in a stagnant gas, while the inside wall heat transfer coefficient was 10 times higher.

A modified resistance network model, the junction factor model, is developed to predict the effective thermal conductivity of sintered microfibrous materials (MFM) made of conductive metals. It contains two characteristic variables: metal volume fraction (y) and junction factor (∅). The junction factor representing the fibers' connection quality can be easily determined by the measurement of electrical resistance, so this model provides a practical and convenient method to estimate the effective thermal conductivity of sintered MFM. Moreover,

various methods to improve the junction factor and the effective thermal conductivity of copper MFM are investigated. High sintering temperatures and long sintering times increase both the junction factor and effective thermal conductivity of MFM. Electroplating and impregnation methods were also employed to enhance the junction conductivity. Electroplating provides a significant improvement in the junction factor and the effective thermal conductivity of the media.

Computational Fluid Dynamics (CFD) was used to compare the micro scale heat transfer inside a packed bed and a MFEC structure. Simulations conducted in stagnant gas determined the thermal resistance of the gas in the micro gaps between the particle-to-particle contact points in the resistance network model of a packed bed. It was shown that thermal resistance at the contact points accounted for 90% of the thermal resistance of the solid path. In the MFEC, the thermal resistance of the continuous metal fibers was relatively smaller than that of contact points. As a result, 97.2% of the total heat flux was transported by continuous fiber cylinders, which was the fundamental function of fibers on improving the heat transfer of MFEC structures. Enhanced heat transfer characteristics of MFEC were further demonstrated by simulations performed in flowing gas, where both heat conduction and heat convection were significant.

To investigate the performance of the enhanced heat transfer characteristics of MFEC, 15wt% Co/Al_2O_3 catalyst particles (149-177μm dia.) were examined in both a packed bed configuration and after being entrapped within a 7.4 vol.% network of sintered Cu fibers (12μm dia.). FTS at 225-255°C, 20bar, H_2/CO of 2.0, was utilized as the probe reaction due to

its exothermicity and temperature dependent selectivity. Both the hot spot and runaway state were prevented by utilizing metal MFEC compared to the packed bed. In a 41mm ID reactor, the maximum temperature deviation from the centerline to the reactor wall was only 6.4°C for the copper MFEC. In contrast, the packed bed diluted to the same catalyst density and operated at an equivalent condition had a centerline temperature deviation of 460°C indicating ignition. The more isothermal temperature profile through the catalyst bed of the copper MFEC led to a higher selectivity of heavy products than that of the packed bed. Also, it enabled a larger reactor diameter to be used with more precise and robust temperature control.

Acknowledgements

I would like to acknowledge the encouragement and guidance of my advisor Dr. Bruce J. Tatarchuk. I would like to address my sincere gratitude to Dr. Yoon Lee, Dr. Robert Ashurst and Dr. Daniel K. Harris for serving on my committee. This dissertation would not have been possible without the unwavering supports and excellent suggestions of Dr. Donald R. Cahela, Dr. Hongyun Yang from Intramicron Inc, and Troy Barron from Intramicron Inc. Also without the cooperation and support of my colleagues at the Center for Microfibrous Materials Manufacturing, especially William R. Yantz Jr., Carlos F. Gonzalez, Dwight Cahela, Kimberly Dennis, Benjamin Doty, Wenhua Zhu, Ying Zhu, Qiang Gu, Hussain, Amogh Karwa, Abhijeet Phalle, Priyanka P. Dhage and many others, this work would not have been possible. I am also grateful to Sue Abner and Karen Cochran for their administrative support throughout my tenure at Auburn.

Most importantly, I would like to thank my family. My sincere thanks go to my friends in Auburn, especially Huirong Li, Lingzhao Kong, Rui Xu, Sihe Zhang, Zhiyang Ding, Yixian Yang and many others.

Table of Contents

List of Tables

Lists of Figures

Nomenclature

A	crossing area, m^2
Bi	Biot number, $h_w d_t / k_{er}$
C_P	heat capacity, J/kg-K
d_t	diameter of reactor tube, m
D	diameter, m
E_a	activation energy for the catalytic reaction, J/mol
h	inside heat transfer coefficient, W/m2-K
ΔH	reaction heat, J/mol
k	thermal conductivity, W/m-K
L	length, m
Pr	Prandtl number
Q	heat flow rate, W
r	radial position, m
r_t	radius of reactor tube, m
R	thermal resistance, K/W
R^*	electrical resistance, Ω
Re	Reynolds number

R'	gas constant, 8.314J/mol-K
R_{FTS}	volumetric reaction rate of FTS, mol_CO/m^3-s
S	surface area, m^2
t	time, s
T	temperature, K
U	overall heat transfer coefficient, W/m^2-K
v	superficial velocity, m/s
V	volume, m^3
W	weight, kg
W'	weight fraction
x	mass fraction
x'	molar fraction
y	volume fraction
z	axial position, m

Greek symbols

ε	voidage
μ	gas viscosity, kg/m-s
ρ	density, kg/m^3
$\emptyset$	junction factor
φ	shape factor

$\Delta\zeta$	dimensionless radius, $\frac{\Delta r}{r_{id}}$
Δx	dimensionless Length, $\Delta z/L$

superscripts

n	n^{th} step

Subscripts

Al	alumina
e	effective
f	fluid
F	fiber
F_jun	junction between fibers
G	bulk gas
gas	gas in the micro-gap
i	i^{th} particle or i^{th} division
id	inside diameter
j	j^{th} division
m	metal
od	outside diameter
p	particle
r	radial

S	interstitial term of solid
$solid$	contact point of solid
w	wall
z	axial
∞	infinite

Chapter I: Introduction and Literature Survey

I.1 History of Fischer-Tropsch Synthesis

In 1923, Fischer-Tropsch Synthesis (FTS) was discovered by Franz Fischer (1877-1947) and Hans Tropsch (1889-1935) at the Kaiser-Wilhelm Institute for Coal Research (KWI) in Műlheim, Ruhr. They successfully produced hydrocarbons from a coal-derived gas by using nickel catalysts [1,2]. The German government encouraged the research of this alternative fuel resource because of the lack of domestic petroleum reservoirs in Germany. In 1935, the first industrial FTS reactor was built by Ruhrchemie A.G in Oberhausen, Germany. By the end of the 1940s, there were already 9 FTS plants with a total liquid fuel production capacity of 600kt/a in Germany in addition to one in France, one in Manchuria, and two in Japan [3,4].

A commercial cobalt catalyst (100 Co, 5 ThO_2, 8 MgO, 200 Kieselguhr) was developed by Ruhrchemie chemist Otto Roelen for low temperature, medium pressue Fischer-Tropsch (LTFT) operations with the main product being middle distillates and wax [5]. This catalyst became the standard FTS catalyst during World War II. Because of the high cost of cobalt, Fischer and Pichler developed an iron based catalyst for medium pressure operations [6]. It was commercialized by the Ruhrchemie and Lurgi companies in the Arge process. Sasol I, which used this new catalyst, was erected in Sasolburg, South Africa in 1955 [7]; it had 5 Arge

tubular fixed bed reactors. By using modern supported cobalt catalyst technology and advanced fixed bed reactors, Shell established a commercial gas to liquid (GTL) facility using multiple tubular fixed bed reactors in Bintulu, Malaysia in 1993, and another one in Qatar in 2006 [8,9].

Higher temperature Fischer-Tropsch (HTFT) was first developed by the hydrocarbon research in USA [10-12]. They utilized a fixed fluidized bed reactor with a fused iron catalyst and termed this mode of operation the "hydrocol process." A GTL plant with several large size reactors using the hydrocol process was built in Brownsville, Texas and started operating in 1951. However, due to the abundant oil reservoirs discovered in the Middle East and the high price of natural gas, GTL technology was not economical in the USA at that time, and the plant was shut down in 1957 [13]. This reactor design was extended by Kellogg to develop circulating fluidized bed reactors for Sasol I. Furthermore, the success of the circulating fluidized bed reactor in Sasol I ensured the development of other fluidized bed reactors utilized in Sasol II in 1980 and Sasol III in 1982 [14]. Guettel et al. [15] summarized the current running FTS plants in the world, as listed in Table I.1. Recently, as the reservoir of crude oil is being depleted and the price of crude oil rises, FTS has been garnering more interest.

Table I.1 Existing plants and plants under construction with FTS process in 2008 [15]

Company	Site	Capacity [bpd (kt/a)]	Raw material	Commissioning date
Existing plants				
Sasol	Sasolburg	2500 (120)	Coal	1955
Sasol	Secunda	85000 (4000)	Coal	1980
Sasol	Secunda	85000 (4000)	Coal	1982
MossGas	Mossel Bay	30000 (1400)	Nature gas	1993
Sasol/Qatar Petroleum	Qatar	34000 (1600)	Nature gas	2006
Under construction				
SasolChevron	Escravos	34000 (1600)	Nature gas	2007
Shell	Qatar	140000 (6500)	Nature gas	2009

I.2 Product distribution of FTS

By employing heterogeneous catalysts in a temperature of 200˚C to 350˚C under an elevated pressure, FTS produces a broad range of hydrocarbons from syngas (synthesis gas), a mixture of hydrogen and carbon monoxide derived from coal, natural gas or biomass. The products of FTS include paraffins, olefins, and alcohols [16,17].

Paraffins: $(2n+1)H_2 + n\,CO = C_nH_{2n+2} + nH_2O$ (I-1)

Olefins: $2nH_2 + n\,CO = C_nH_{2n} + nH_2O$ (I-2)

Alcohols: $2nH_2 + n\,CO = C_nH_{2n+1}OH + (n-1)H_2O$ (I-3)

where each reaction involves a wide range of substances with a different carbon atom number (n). The distribution of the paraffins that are the primary products for most of the FTS conditions is described by the Anderson-Schulz-Flory(ASF) equation [18-20]:

$$x'_n = (1-\alpha)\cdot\alpha^{n-1} \quad \text{or} \quad W'_n = n\cdot(1-\alpha)^2\cdot\alpha^{n-1} \tag{I-4}$$

where x'_n is the molar fraction, W'_n is the weight fraction, and α is the chain growth probability factor. Based on this equation, the relation between the weight fractions of the paraffinic products in different carbon ranges and the α value is presented in Figure I.1. It is shown that a high α value gives a high selectivity of heavy products for FTS reaction. The typical α value of ruthenium, cobalt and iron based catalyst is 0.85~0.95, 0.70~0.80, and 0.50~0.70, respectively [21].

Significant deviations from the ASF distribution are observed and diverse explanations are proposed in the literature. For example, writing about the high yield of methane from FTS, Wojciechowski [22] proposed that it results from the increased termination probability of C_1 precursors. Dry [21] mentioned that the mass transfer limitation results in an increase of thermodynamically favored products (i.e., methane). Dictor and Bell [23] concluded that the hot spots perhaps introduces a low chain growth probability factor and a high yield of methane. For the low yield of ethane and ethene, the secondary reaction was often mentioned as the most possible reason [24-26].

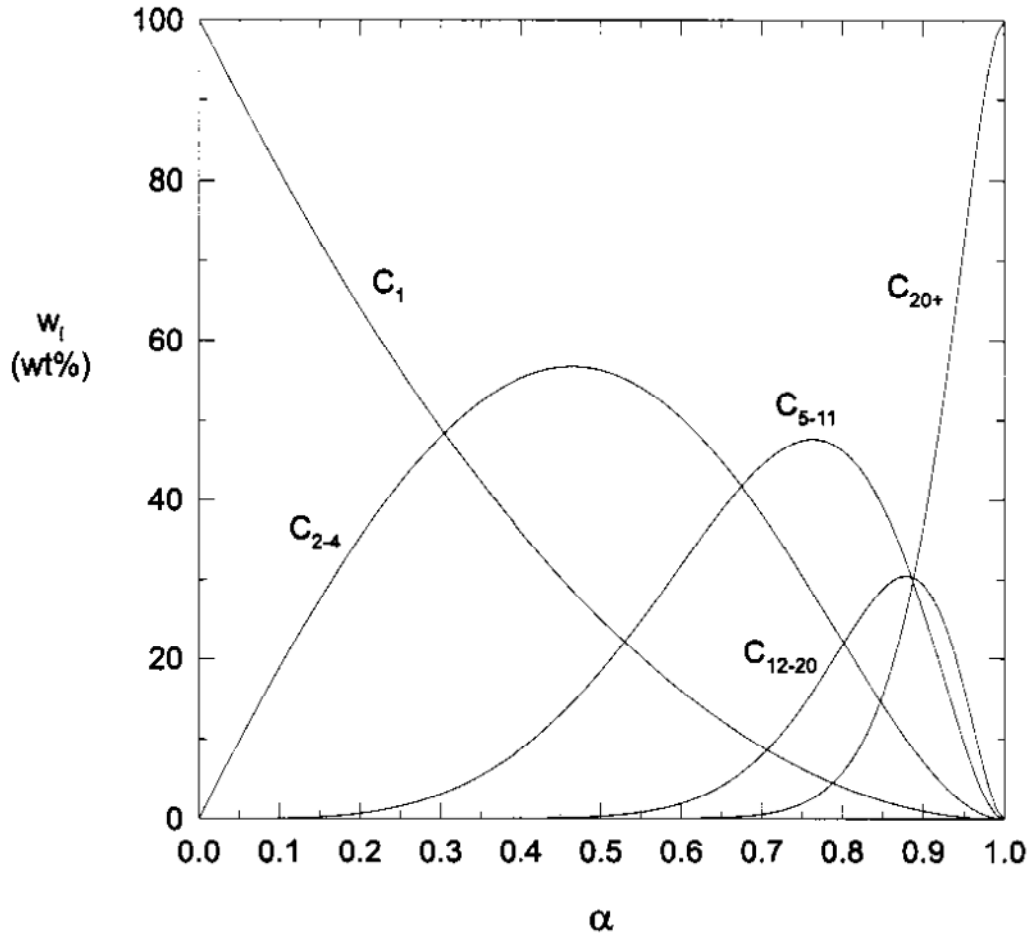

Figure I-1. Relation between the product distribution and the chain growth probability factor [8,9,27]

I.3 Highly exothermic nature of FTS process

The potential reactions involved in the FTS process are given as following [28]:

FTS: $CO + 2H_2 = \cdots CH_2 \cdots + H_2O \quad \Delta H_{r,227} = -165kJ/mol$ (I-5)

Water-Gas Shift (WGS): $CO + H_2O = H_2 + CO_2 \quad \Delta H_{r,227^{\circ}C} = -39.7kJ/mol$ (I-6)

Net reaction of WGS: $2CO + H_2 = \cdots CH_2 \cdots + CO_2 \quad \Delta H_{r,227^{\circ}C} = -204.7kJ/mol$ (I-7)

Methanation: $CO + 3H_2 = CH_4 + H_2O \quad \Delta H_{r,227^{\circ}C} = -214.5kJ/mol$ (I-8)

Boudouard reaction: $2CO = C + CO_2 \quad \Delta H_{r,227^{\circ}C} = -173.5kJ/mol$ (I-9)

As shown above, most of these reactions generate a large amount of reaction heat. The FTS reaction is a highly exothermic reaction with a reaction heat of -165kJ/mol of CO and an adiabatic temperature rise of 1600˚C [29]. Since a uniform temperature profile through the catalyst bed ensures a high selectivity of the desired heavy products and a low deactivation rate of the catalyst, a rapid removal of the reaction heat from the catalyst bed is the major consideration for a suitable reactor design [8, 14].

It was found that the highly exothermic nature of FTS limited the length of the path for heat transfer from catalyst granules to a cooling surface to less than 10mm, and preferably 7mm [30]. Therefore, a conventional tubular reactor with a large diameter is not suitable for this application. Generally, fluidized bed reactors, slurry phase reactors or multiple tubular fixed bed reactors have to be used for the pilot and industrial plants.

I.4 FTS reactors

Because they are simple to operate, easy to scale up, flexible to use over a wide temperature range and have no separation requirement for the products from the catalyst particles, fixed bed reactors are treated as the standard type of catalyst reactors for FTS.

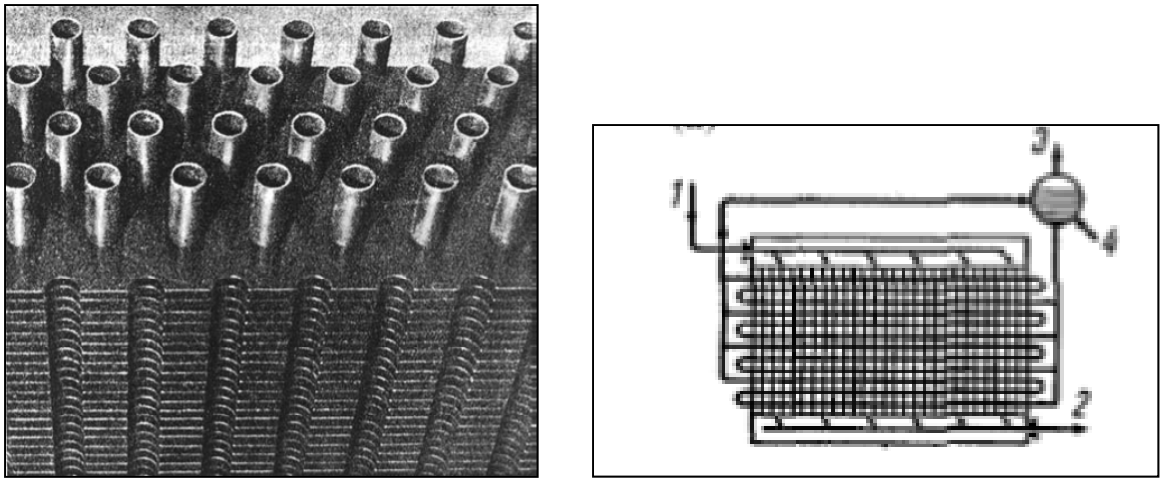

Figure I-2. Parallel plate reactor for FTS process: 1. syngas inlet; 2. product; 3. steam outlet, 4. water inlet [30,31].

During World War Π, a rectangular box reactor was used for FTS process under ambient pressure (1bar) in Germany [30,31]. It consisted of 600 parallel plates spaced 7mm apart and pierced by 600 cooling tubes where steam was produced from water. It was about 6×1.8×2.7m in total (Figure I.2). The catalyst particles were loaded between the plates, and the reaction heat was removed by the metal plates and the cooling tubes. Because of how difficult it is to manufacture this type of reactor for high pressure operation, and how time consuming loading and unloading the catalyst particles is, this design was eventually replaced by other designs of FTS reactors.

At the same period, a multiple tubular fixed bed reactor consisting of 2000 double wall tubes was also utilized for the FTS process under a middle pressure (10bar to 15bar) [32,33]. The double wall tubes were 48mm in OD, 24mm in ID and 4.5m in length (Figure I.3). The

catalyst, typically 100Co:5TnO_2:8MgO:200SiO_2, located in the annular section. Cooling water flowed through the inner tubes and surrounded outside the outer tubes. This reactor provided a high ratio of heat exchange surface area to catalyst volume and rapidly removed the reaction heat from the catalyst bed. However, it was expensive to manufacture the double wall tubes and extremely difficult to load and unload the catalyst particles.

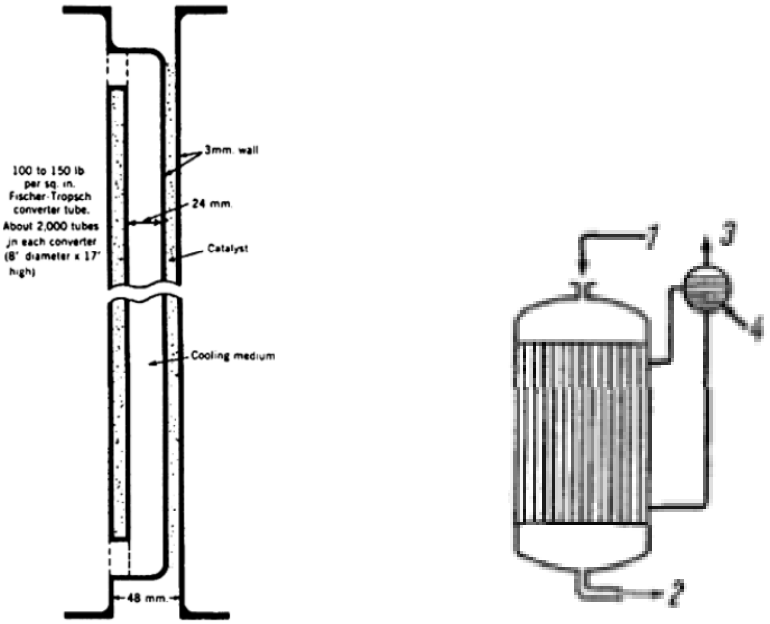

Figure I-3. Tubular reactor with double wall tubes; 1, syngas inlet; 2, product; 3, steam outlet, 4, water inlet [32,33].

Besides increasing the ratio of heat exchange surface area to catalyst volume by employing a complicated reactor design, another potential method to enhance the removal of reaction heat from the catalyst bed is to recycle a sufficiently large amount of residual gas, or

sometimes, liquid products. The high face velocity of the recycled gas results in a turbulent flow condition inside the catalyst bed. In this turbulent flow condition, more reaction heat can be removed by minimizing the thickness of the stagnant boundary layer, increasing the heat convection term and enhancing the heat transfer of the catalyst bed.

Based on this theory, a circulating-gas fixed bed reactor was developed by IG-Farben and Michael Verfahren in a pilot scale laboratory [34,35]. The reaction heat in this reactor was removed by a gas stream that was subsequently externally cooled. The catalyst bed, made of shallow particles, was 1.5m in diameter and 1.0m long, without any inside cooling tubes (Figure I.4). Generally, 100 volumes of the residual gas was recycled for every volume of the fresh syngas. However, due to overheating problems in some parts of the catalyst bed, this reactor design did not operate well at industrial scales.

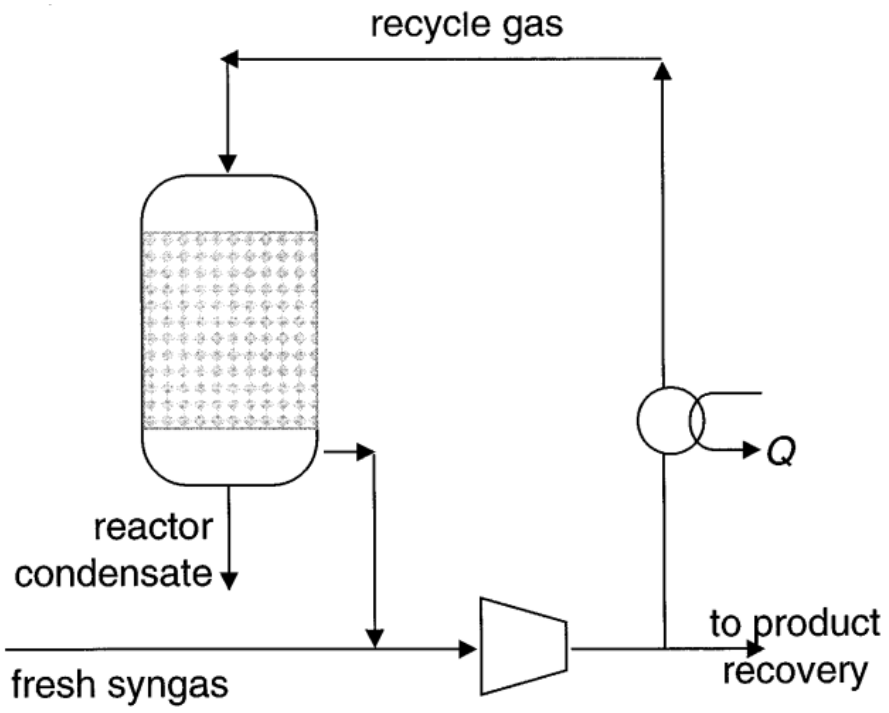

Figure I-4. Circulating-gas fixed bed [34]

A successful reactor design using recycled gas was the Arge reactor, developed by Lurgie and Ruhrchemie for Sasol I in 1955. These reactors are still in operation in Sasolburg, South Africa [36-38]. Five Arge reactors, four online and one on standby, are tubular fixed bed reactors with residual recycled gas. These Arge reactors are comprised of a shell with a diameter of 3m and a height of 13.1m, and 2000 tubes inside the shell, with a ID of 50mm and a length of 12m (Figure I.5). The tubes are loaded with an extruded iron based catalyst. The operation pressure is 25bar and the recycled gas ratio is in the range of 2.2 to 2.5. The product throughput per reactor is approximate 250kg/day. The temperature of the catalyst bed is controlled between 220°C and 225°C by water at the shell side that removes the reaction heat

by generating steam under pressure. This low temperature operation corresponds to a potential of product distribution to heavy hydrocarbon compounds. As a result, over 50% of the products from the Arge reactors are food grade wax. Another GTL plant with Arge reactors was built by Shell in Bintulu, Malaysia. The tube diameter of these Arge reactor is smaller (smaller than 50mm ID), because they used a cobalt based catalyst that has a higher activity than iron based catalyst used in the other Arge reactors.

The recycled gas enlarges the length of the path for heat transfer from catalyst granule to a cooling surface. However, even with the recycled gas, the poor effective thermal conductivity of the fixed bed made of catalyst granules limits the diameter of the tubular reactor. Van Vuuren [39] determned that the maximum diameter of the tubular fixed bed made of catalyst granules is 80mm. Since an enhanced heat transfer characteristic is required by the highly exothermic nature of the FTS process, several reactor designs have been developed to address this issue.

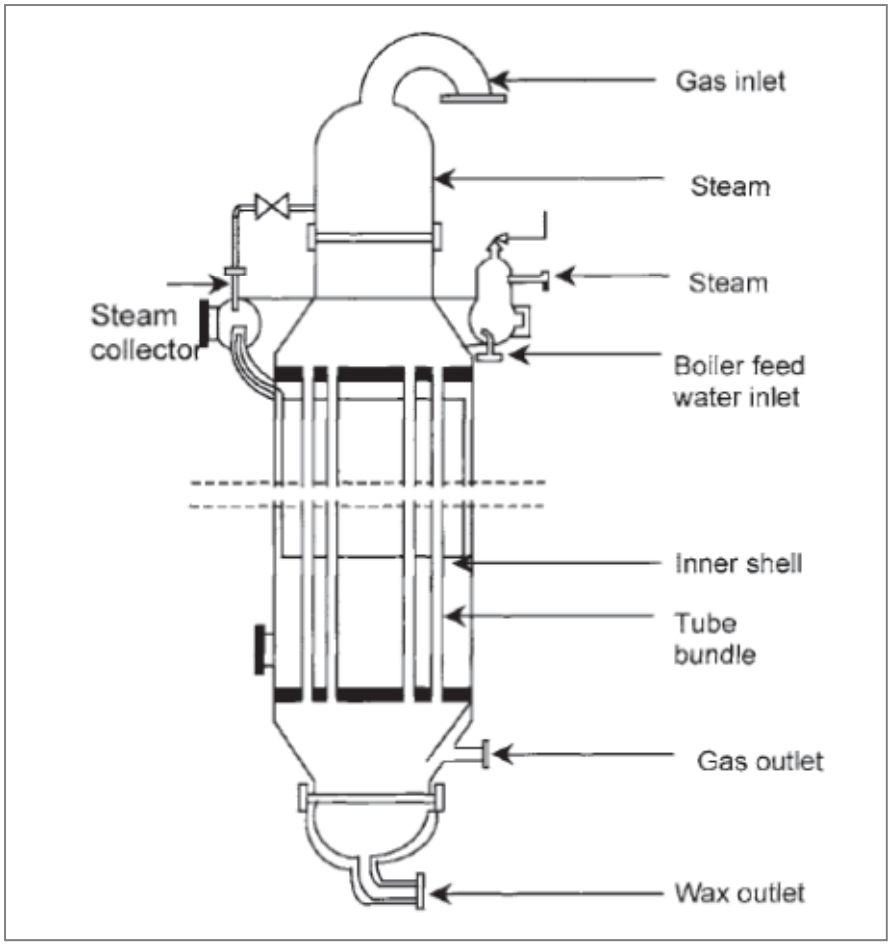

Figure I-5. Arge tubular fixed bed reactor [36]

Fluidized bed reactors for the FTS process were developed for this purpose. In a fluidized bed reactor, small catalyst particles move along with the high velocity gas. The turbulent flow of the gas and the catalyst particles increases heat convection and minimizes stagnant gas or liquid film collecting near the cooling surface. In addition, frequent physical contacts of the hot catalyst particles with the heat exchange surface also significantly increase the heat transfer efficiency of the reactors [8]. The fluidized bed reactor is a two phase reactor

with a gas phase and solid phase. The appearance of a liquid phase that will cause the agglomeration of the fine catalyst particles needs to be avoided. Generally, a high operating temperature is employed to prevent the formation of liquids inside the reactor. Consequently, the fluidized bed reactor is usually operated at high temperatures with light hydrocarbons as the major products. There are two types of fluidized bed reactors: circulating fluidized bed reactors and fixed fluidized bed reactors.

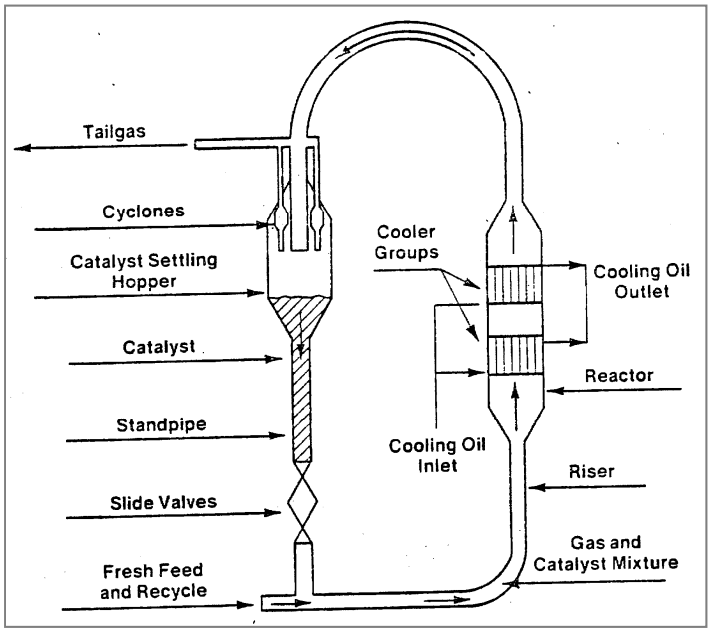

Figure I-6. Circulating fluidized bed reactor [40]

In a circulating fluidized bed reactor (Figure I.6), grounded catalyst particles are carried out by high velocity gas from the top of the reactor and caught in the disengaging section by

cyclones; then, the catalyst particles flow down along the standpipe to be swept back into the reactor by the incoming syngas [40,41]. Sasol I uses three circulating fluidized bed reactors that have a ID of 2.3m and a height of 36.6m. Based on the successful use of these reactors in Sasol I, Sasol Π and ΙΙΙ use only circulating fluidized bed reactors, without any Arge tubular fixed bed reactors. These circulating fluidized bed reactors have a 3-fold reactor capacity of those in Sasol I because of their greater operating pressure and catalyst size. However, the circulating fluidized bed reactor has a disadvantage. It is complex to operate, because the pressure control of the slide valve is very sensitive to the flowing stream and it is easy to cause a false flow of catalyst particles due to pressure variation.

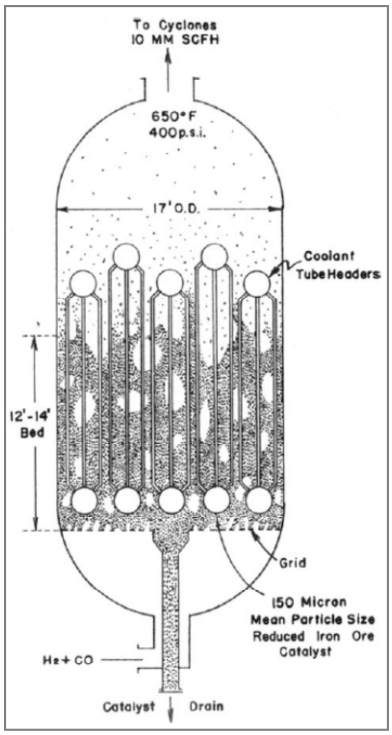

Figure I-7. Fixed fluidized bed reactor [17]

Without the circulation of catalyst particles outside the reactor, a fixed fluidized bed reactor is much simpler to operate. In a fixed fluidized bed reactor, syngas enters at the bottom of the reactor through a suitable distributor. Due to a large particle size and a relatively low gas velocity, catalyst granules in the fixed fluidized bed reactor are not transported outside of the reactor as in the circulating fluidized bed reactor. The catalyst bed that is "stationary" and very turbulent inside offers an enhanced heat transfer characteristic [10-12]. Such a fixed fluidized bed reactor plant was erected by Carthage Hydrocol in Brownsville, TX in 1951. The reactor was 18m in height and 5.2m in diameter with a nominal liquid fuel capacity of 180kt/a (Figure I.7). This plant was shut down in 1957 for economic reasons [13].

Another version of fluidized bed reactor is a slurry phase reactor. It is a three phase system usually operated to produce heavy wax [13,42]. In a slurry phase reactor, the fed gas is bubbled through a liquid phase in which catalyst particles are suspended (Figure I.8). The continuous liquid phase has a considerably higher thermal conductivity than that of the gas phase in a conventional fixed bed reactor. Also, the moving liquid offers a high convection contribution to the removal of reaction heat. So the enhanced heat transfer characteristic of the catalyst bed in a slurry phase reactor suppresses that of other reactor designs. Sasol completed the development of the slurry phase reactor in the 1990s [43]. One slurry phase reactor with a diameter of 5m was built in Qatar and now it has been operated successfully for more than 10 years without any problems.

To summarize there are three types of FTS reactors used in the industrial scale: Arge tubular fixed bed, fluidized bed and slurry phase reactor. Each one has own advantages

and disadvantages. Van Vuuren [39] summarized his comparison of these reactor types, as listed in Table I.2. Each type of reactor has its own advantage over the others. The selection of reactor type will depend on the desired product, the operating temperature range, the impurity of the syngas and other economic reasons. In addition, advanced technologies developed everyday for each type of reactor are also an important consideration for the design of a FTS reactor.

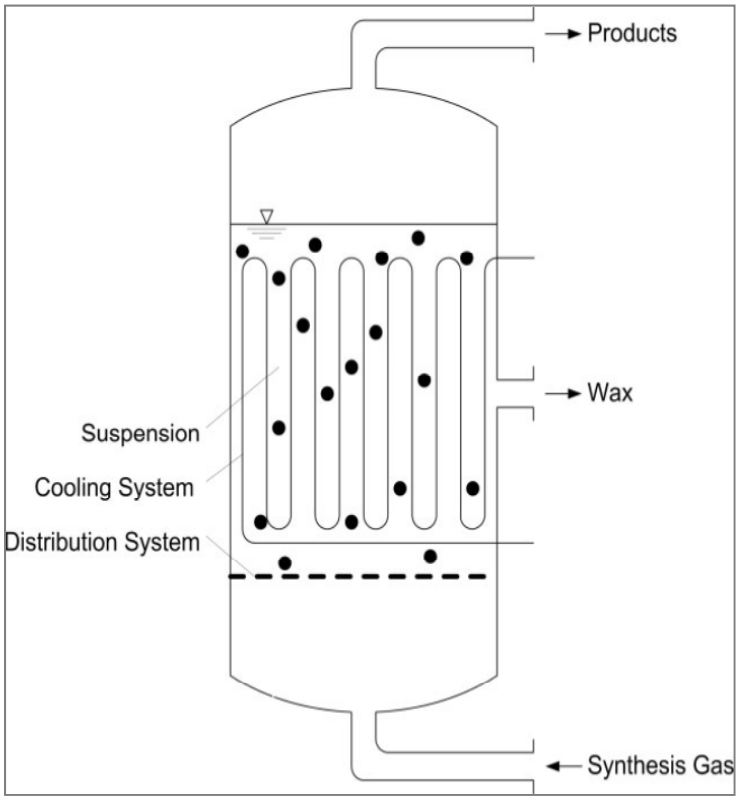

Figure I-8. Slurry phase bed reactor [15]

Table I.2 Comparison of reactor types [39]

Feature	Fixed bed	Fluidized bed(circulating)	Slurry phase
Operation	simple	complex	intermediate
Temperature control	poor	good	good
Heat exchanger surface	$240m^2$ per $1000m^3$ feed	$15\text{-}30m^2$ per $2000m^3$ feed	$50m^2$ per $1000m^3$ feed
Max. reactor diameter	<80mm	large	large
Ch_4 formation	low	high	as fixed bed or lower
Flexibility	high	little	intermediate
Product	full range	low mol. Weight	full range
Space-time yield(C_{2+})	$>1000kg/m^3$ day	$4000\text{-}12000kg/m^3$ day	$1000kg/m^3$ day
Catalyst effectivity	lowest	highest	intermediate
Back mixing	little	intermediate	large
Minimum H_2/CO feed	as slurry or higher	highest	lowest
Construction			simplest

I.5 Fixed bed reactors

As mentioned by Davis [14], the fixed bed reactors remain an attractive approach because they have the highest volumetric catalyst loading (catalyst loading/reactor volume), and hence the highest volumetric productivity.

Other advantages of a tubular fixed bed reactor are:

1) Simple operation;

2) Usable in a wide temperature range, with either gas or liquid as product, or both;

3) Requires no separation of the products from the catalyst particles;

4) They are well studied and there are many models to predict the mass transfer and heat transfer in them;

5) H_2S poison is absorbed by the top layers of the catalyst bed, and hence the reminder of the catalyst bed remains an unaffected high activity [8].

However, there are some disadvantages that limit a wide application of fixed bed reactors for the FTS process:

1) The poor effective thermal conductivity of a conventional fixed bed made of catalyst granules prevents the reactor from being scaled up to a large diameter;

2) High velocity gas through the fixed bed creates a high differential pressure drop over the reactor that consumes a considerable energy cost for the gas compression;

3) A larger diameter of the catalyst particles required to reduce the pressure drop always decreases the reaction effectiveness factor, because of the diffusion limitation from the mass transfer of the reactants and the products;

4) The complicated construction of the multiple tubular reactor is expensive to manufacture [13].

To improve or overcome these shortcomings of the fixed bed reactors, various techniques have been developed. For example, during the catalyst preparation, the catalytic active component is loaded only in the outer layer of support particles that can reduce the diffusion path and increase the reaction effectiveness.

Recently, other advanced technologies have been applied to the fixed bed reactors of the FTS process. Supercritical media is one of them. By investigating FTS in a supercritical hexane medium with silica-supported cobalt catalysts, Yokota and Fujimoto [44] demonstrated that the heaviest hydrocarbon compound in the liquid phase product was C_{40}, compared to C_{26}

in a conventional fixed bed. Abbaslou et al. [45] reported that supercritical media, with a gas-like diffusivity and a liquid-like solubility, efficiently removed the heat zone in the catalyst bed and improved the mass transfer of reactants and products in the catalyst pores. They also found that the overall product distribution shifted towards the heavier hydrocarbon range. Huang and Roberts [46] reported that, beside the production distribution shifting to heavier compounds, 1-olefin contents in the supercritical phase of hexane solvent were always higher than that in a conventional fixed bed. In spite of these benefits, this technique is not economically feasible due to the extremely high pressure required. Moreover, it introduces an additional process to separate the liquid products from the solvent, hexane or pentane, which usually needs to be recycled in a large-scale plant.

Another popular technology is the application of monolith-structured catalysts. In the last decade, increasing attention has been directed to monoliths catalysts in the FTS process. Hilmen et al. [47] discussed monolith catalysts made of different materials for the FTS process. They found that, when loaded with a small amount of catalyst, approximately 0.04~0.05mm thickness of washcoat layer, cordierite monolith showed the same activity and the same product selectivity as a conventional packed bed made of small size catalyst particulates. A larger thickness of washcoat layer resulted in mass transfer restrictions and thus decreased selectivity to heavy products. Deugd et al. [48] proposed a system that recycles the liquid products to enhance the heat transfer of the cordierite monolith catalyst (Figure I.9). Visconti et al. [49] reported on a metallic monolith structure washcoated with a thin layer of cobalt catalyst. This metallic monolith showed a high thermal conductivity, small diffusion limitation and low pressure drop and ideal plug-flow behavior. However, the volumetric catalyst loading

is usually low in this type of reactor due to the thinness of the catalyst layer in monolith structures (10~150μm). Furthermore, the manufacturing of monoliths and the washcoat of catalyst layer are too complex for a large scale application.

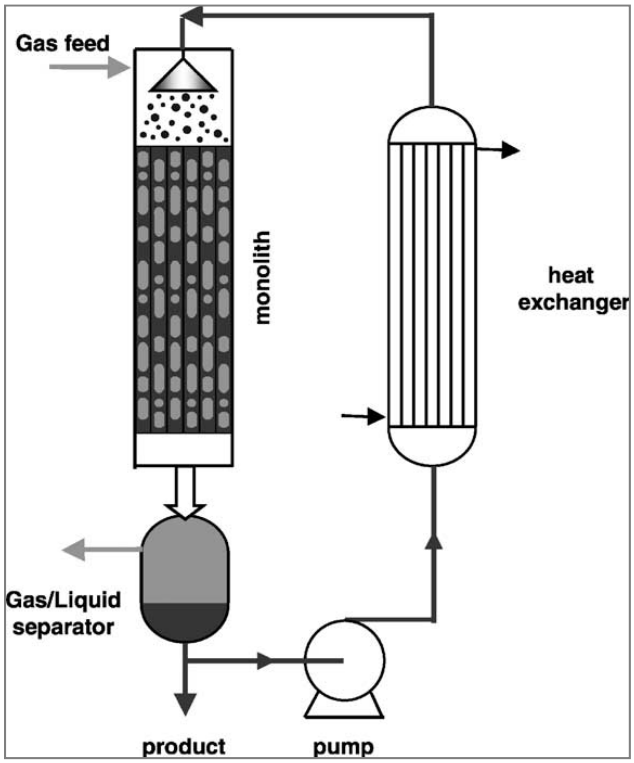

Figure I-9. FTS reactor system with cordierite monoliths [48]

I.6 Temperature-dependent issues in fixed bed reactors

Among the shortcomings of fixed beds, the most crucial one for their application to the FTS process is their poor effective thermal conductivity. This is the primary motivation for using fluidized bed reactors and slurry phase reactors. The problem of hot spots in a fixed bed

reactor introduces several problems such as poor product selectivity and short catalyst lifetime [8].

First, FTS product distribution strongly depends on the local temperature of the catalyst. It has been reported by many researchers that the selectivity of heavy products in the FTS process decreases as the catalyst bed climb higher [23, 50, 51]. Figure I.10 shows the experimental data of the iron based catalysts reviewed by Laan and Beenackers [27]. Furthermore, for high temperature operations, the mathenation reaction that converts syngas back to methane (the main compound of natural gas) predominates.

Lox [51] and Thompson [52] employed reaction mechanisms to explain this dependence of product selectivity upon temperature. They proposed that the α value was a function of temperature as well as a partial pressure of hydrogen and carbon monoxide. Lox developed an equation to estimate α value based on the kinetic data of iron catalysts, as following.

$$\alpha = \frac{k_1 P_{CO}}{k_1 P_{CO} + k_5 P_{H_2} + k_6} \tag{I-10}$$

where reaction rate is given by:

$$k = k_{T_0} * \exp\left[\left(-\frac{\mathrm{E}}{\mathrm{R}}\right) * \left(\frac{1}{\mathrm{T}} - \frac{1}{\mathrm{T_0}}\right)\right] \tag{I-11}$$

The parameters are listed in Table I.3.

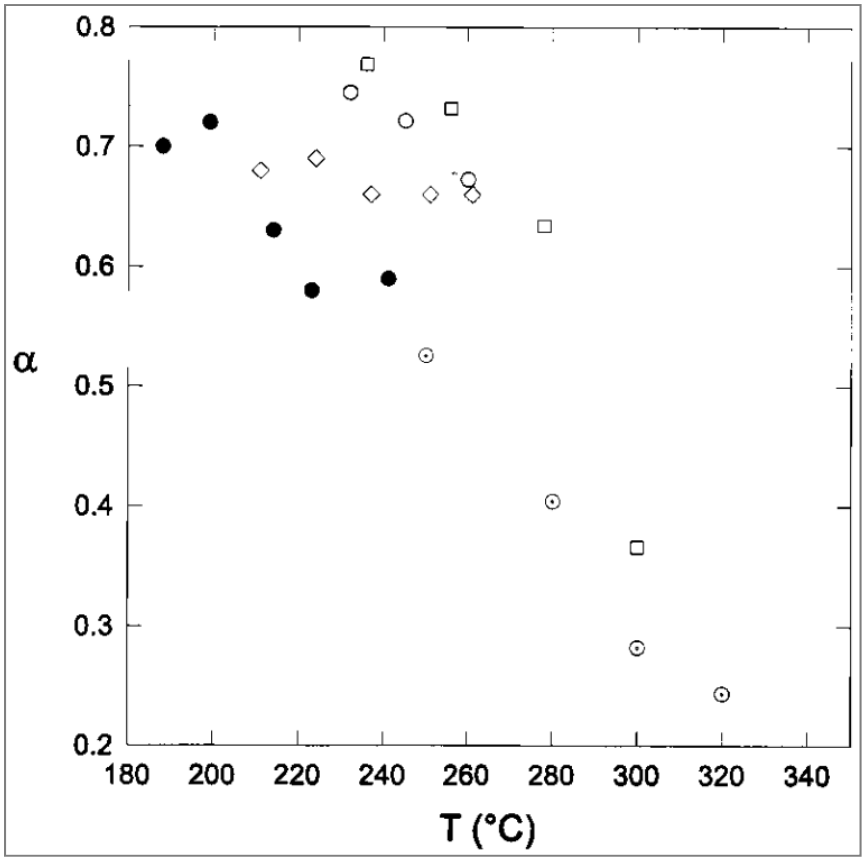

Figure I-10. Chain growth probability factor(α) from experimental data of iron based catalysts [27]

Table I.3 Parameters for the equation to estimate the α value [51]

parameter	dimension	estimate
k_1 @573	mol/(g·s·bar)	1.22×10^{-5}
E_1	kJ/mol	~0
k_5 @573	mol/(g·s·bar)	1.05×10^{-6}
k_5	kJ/mol	94.5
k_6 @573	mol/(g·s)	2.36×10^{-6}
E_6	kJ/mol	132.2

There are several other empirical correlations to estimate α. For example, Yermakova and Anikeev [54] suggested a formula for iron based catalysts in which α depended on the molar fractions of hydrogen and carbon monoxide.

$$\alpha = A\frac{y_{CO}}{y_{CO}+y_{H_2}} + B \tag{I-12}$$

Where A=0.2332±0.0740, B=0.6330±0.0420.

For cobalt based catalysts, Song et al. [54] modified Eq. I-12 by adding a temperature dependent term.

$$\alpha = (A\frac{y_{CO}}{y_{CO}+y_{H_2}} + B)\cdot[1 - 0.0039(T - 533)] \tag{I-13}$$

Where the unit of T is K.

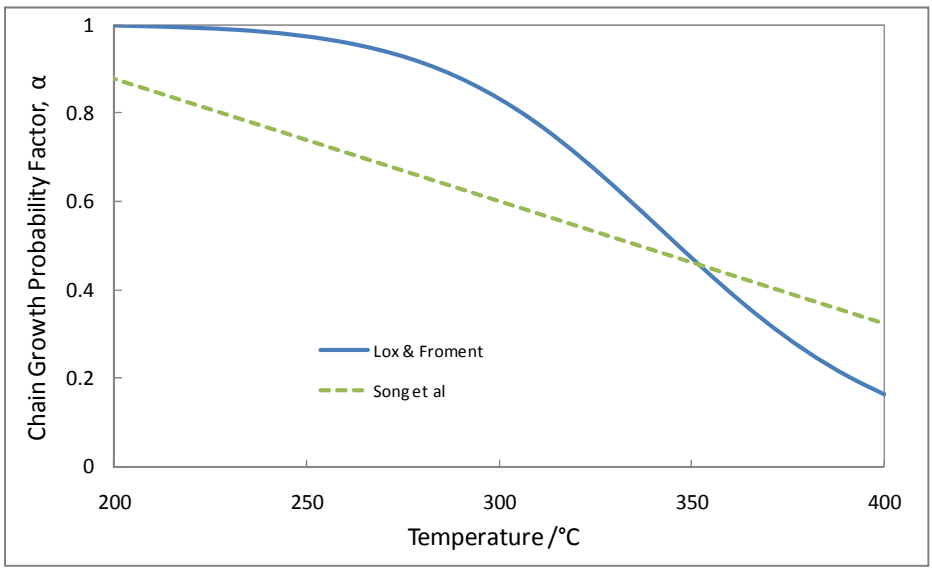

Figure I-11. The relation between the chain growth probability factor(α) and the temperature at H2/CO equal to 2 [51,54]

The dependence of the α value on temperature is obtained from Eq.I-10 and Eq.I-13, as presented in Figure I.11. It is shown that the α value is reduced to a small value in the high temperature range. As discussed previously (Figure I.1), as the α value decreases, the products of FTS reaction shift to light hydrocarbon compounds, and the selectivity to heavy hydrocarbon compounds that are the desired part of FTS products decreases dramatically. To ensure a high α value and a proper product distribution, a low operational temperature and uniform temperature profile throughout the catalyst bed are very critical for a fixed bed reactor used for the FTS process.

Table I.4 Summery of FTS kinetics and parameters from literatures

Catalyst	Reaction rate	k	k_1	T_0 /°C	Literature
Fused iron	$r_{FTS} = \frac{kP_{CO}P_{H_2}}{P_{CO} + k_1 P_{H_2O}}$	0.0017(mol/gcat·s·Mpa) 85 (kJ/mol)	0.028(mol/gcat·s·Mpa) -8.8(kJ/mol)	250	[59]
Fe/Cu/K	$r_{FTS} = \frac{kP_{CO}P_{H_2}}{P_{CO} + k_1 P_{H_2O}}$	0.062(mol/gcat·s·Mpa) 85 (kJ/mol)	0.58(mol/gcat·s·Mpa) -8.8(kJ/mol)	265	[56]
Unpromoted Fe	$r_{FTS} = kP_{CO}^{-0.42}P_{H_2}^{1.4}$	3.77E+6 (mol/kgcat·s·$atm^{0.98}$) 101 (kJ/mol)		265	[55]
Fe/K	$r_{FTS} = kP_{CO}^{-0.05}P_{H_2}^{0.6}$	3.77E+6 (mol/kgcat·s·$atm^{0.55}$) 92 (kJ/mol)		265	
Co/MgO/ThO_2/SiO_2	$r_{FTS} = \frac{kP_{H_2}P_{CO}^{1/2}}{(1 + k_1 P_{CO}^{1/2})^3}$	0.0033 (mol/gcat·min·$bar^{3/2}$) 105 (kJ/mol)	1.2 $bar^{-1/2}$ 20(kJ/mol)	210	[57]
Co/SiO_2	$r_{FTS} = \frac{kP_{CO}P_{H_2}^{3/2}}{(P_{H_2O} + k_1 P_{H_2}P_{CO})^2}$	1.1E-5 (mol/gcat·min·$bar^{3/2}$) 105 (kJ/mol)	0.078 bar^{-1} 20(kJ/mol)	210	[58]

Second, the reaction rate of FTS is greatly influenced by the temperature of the catalyst bed. A hot spot in the catalyst bed worsens the product selectivity of the FTS process because most of reactants are consumed in the high temperature catalyst zone and converted to undesired light products. The kinetics of FTS systems that indicate the relation between reaction activity and the catalyst temperature have been studied by many researchers, using approaches based on thermodynamic and different reaction mechanisms. Eliason and Bartholomew [55] used an empirical power law expression to describe the kinetics of FTS with iron-based catalysts. Atwood and Bennett [59], Leib and Kuo [56] applied a Langmuir-Hinshelwood expression for commercial iron catalysts. Rautavuoma and Bann [57] and Steen and Schulz [58] also employed a Langmuir-Hinshelwood expression for cobalt based catalysts (Table I.4).

In an un-poisoned fixed bed reactor, if fresh syngas with high partial pressures of hydrogen and carbon monoxide is preheated before contacting the catalyst bed, they resultin a high reaction rate within the front part of the catalyst bed. Then, a large amount of reaction heat is generated in this short range at the entrance of the catalyst bed. This reaction heat raises the local temperature, which in turn increases the reaction rate and consumes more reactants. If this thermal runaway tendency is not limited by efficient heat transfer, overheating zones or hot spots will develop in the catalyst bed. Meanwhile, in the downstream catalyst bed, the reactant concentrations are low and the catalyst is unused, so that the overall catalyst efficiency is low for this fixed bed reactor. Kölbel [60] showed this relation in a fixed bed with a diameter of 10mm, made of catalyst granules (Figure I.12). It was shown that the highest reaction rate

occured in the location with the highest temperature which was near the entrance of the catalyst bed and where the reactant partial pressures rapidly declined.

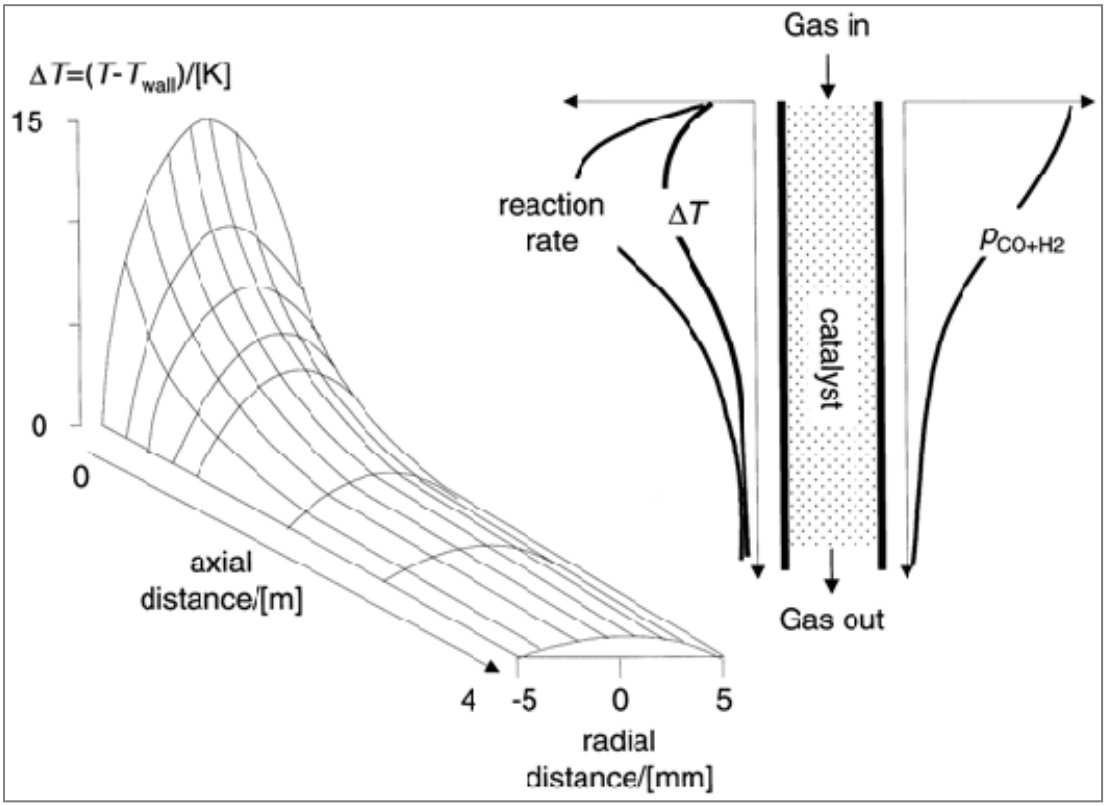

Figure I-12. Reaction rate and concentration with the temperature in a tubular fixed bed reactor [29,60]

Third, the deactivation rate of FTS catalysts is related to the temperature of catalyst beds. Generally, as the temperature increases, the deactivation rate of the catalysts increases. The possible deactivation mechanisms of FTS catalysts are all related to or accelerated by a

high temperature. These include poisoning, crystal sintering, carbon fouling, thermal degradation, re-oxidation and metal-support interaction. Bartholomew [61] reported that a catalytic reaction conducted at a high temperature possessed a high possibility of thermal degradation and fast growth of active phase crystallite (crystallite sintering), as well as more solid-state reactions of the active metal phase with the carriers (metal-support interaction). Thermal degradation due to the high temperatures of the catalyst bed collapses the support pore structure and results in a loss of catalyst activity. Crystallite sintering is also strongly temperature dependent. The underlying mechanism is a surface diffusion or the mobility of metal crystals to form larger aggregates at a sufficiently high temperature. Moulijn [62] reported that the Hűttig temperature, which is the temperature the atoms at defects will become mobile, is 253°C for cobalt and 269°C for iron. These temperatures are in the operating temperature range of low temperature FTS. Therefore, the higher temperature in a catalyst bed with a non-uniform temperature profile easily accelerates the diffusion of the catalytic metal and increases the probability of metal crystal collision. Bian et al. [63] provided direct evidence of the fast growth of cobalt crystals at temperatures above 240°C by utilizing XRD and EXAFS. Carbon fouling is also accelerated by high temperatures. By using temperature-programmed surface reaction and auger electron spectroscopy, Lee et al. [64] showed that the amount of carbon deposited on the surface of the catalyst increased with higher temperatures. The atomic surface carbon transformed morphologically into polymeric and graphitic carbon, which resulted in the reduction of activation energy from 117–134kJ/mol to 71–75kJ/mol; the activity declined significantly as well.

Finally, the thermal runaway state of the FTS process may cause permanent damage to the catalyst and even to the reactors. In a fixed bed reactor that has a poor overall heat transfer coefficient, the mutual enlargement tendency of the reaction rate and temperature is difficult to inhibit. Then a hot spot perhaps develops in the catalyst bed or a runaway state is approached in the reactor. The hot spot and the runaway state sharply decrease the selectivity of the heavy products, produce a significant amount of methane, and cause a permanent decrease in catalyst activity. Sometimes the temperature of a runaway state is high enough to significantly reduce the strength of the metal reactor tubes. Since the reactor tubes are operated under high pressure and with highly flammable and toxic gases, it is a very dangerous situation to have the metal strength reduced. Therefore, controlling the temperature of the fixed bed reactor is very vital for safe operation of the FTS process.

I.7 The poor thermal conductivity of a packed bed

Granular materials have been used in chemical reactions, explosives, ceramics and thermal insulation techniques for a long time. Many researchers have studied the heat transfer properties of packed beds made of granules. Saunders [65] proposed to use the principle of similitude to study the heat transfer of granules in heterogeneous systems. He concluded that the effective thermal conductivity of the packed bed was independent of the size of granules and would be proportional to the interstitial thermal conductivity of the granules. Schumann and Voss [66] first pointed out that the point contacts between particles were so small that the thermal resistance of the packed beds primary came from the point contacts. They measured the effective thermal conductivities of various granules in different fluids by immersing a tube

packed with granules into a bath filled with a heated liquid at a constant temperature and simultaneously starting to measure the heating curves on the plane at the middle length of the packed bed. The estimations of the effective thermal conductivities are listed in Table I.5. The tests under high vacuum (0.93Pa of air) demonstrated that the solid point contacts between particles provided a very small effective thermal conductivity. They also concluded that the fluid in the heterogeneous systems played an important role in the heat conduction through the granules. The effective thermal conductivity was almost independent of the material of granules. Bala et al. [67] reported that the effective thermal conductivity of copper powders was in the range of 0.232W/m-K to 0.652W/m-K for particles with diameters from 75μm to 250μm. This confirmed the high thermal resistance of the point contacts in a packed bed.

Table I.5 Effective thermal conductivities form the study of Schumann and Voss [66]

Particle material	Particle size /μm	Void (fluid)	Pressure /Pa	Effective thermal conductivity /(W/m-K)
Steel shot	1266	0.365 (air)	101,325	0.7455888
Steel shot	1266	0.365 (air)	86659.3	0.7455888
Steel shot	1266	0.365 (air)	45862.8	0.7455888
Steel shot	1266	0.365 (air)	12932.2	0.6702768
Steel shot	1266	0.365 (air)	3466.4	0.50910912
Steel shot	1266	0.365 (air)	154.7	0.23271408
Steel shot	1266	0.365 (air)	40.0	0.16794576
Steel shot	1266	0.365 (air)	0.93	0.07079328
Steel shot	1266	0.365 (H2)	101,325	2.297016
Lead shot		0.40 (air)	101,325	0.7757136
Lead shot		0.31 (air)	101,325	1.2200544
Lead shot		0.40 (H_2)	101,325	2.522952
Lead shot		0.40 (water)	101,325	6.2584272
Lead shot		0.40 (Glycerine)	101,325	3.6827568

For packed beds made of typical catalyst supports or catalyst granules, Sharma and Hughes [68] carried out experiments to determine the effective thermal conductivities of alumina, silica, and silica loaded with nickel. They used a steady state method by measuring the heat flux through cylindrical pellets. As shown in Figure I.13, all effective thermal conductivities of these typical catalyst supports were lower than 0.2W/m-K. Figure I.14 shows that the effective thermal conductivity was a function of the voidages of the intra-particle pores of the catalyst materials. The slight change of the effective thermal conductivity with different nickel loadings suggested that the metal loading on the catalyst supports did not significantly increase the effective thermal conductivity of the catalyst bed. McElroy et al. [69] investigated the relation between the thermal properties of an alumina packed bed and the gas pressures. They reported that the effective thermal conductivity of a packed bed made of 500μm alumina particles in 0.1, 1.0, 30MPa is 0.274, 0.293, 0.30W/m-K for nitrogen gas and is 1.19, 1.40, 1.44W/m-K for helium gas, respectively. Therefore, even a high pressure doesn't considerably increase the thermal conductivity of the packed bed made of catalyst particles.

The effective thermal conductivity of a catalyst bed increases to some degree along with the face velocity of flowing gas because the convection contribution of the heat transfer is improved by the flowing gas. As listed in Table I.6, various empirical correlation equations to predict the effective thermal conductivity have been proposed for packed beds made of particles. Figure I.15 presents the comparison of the predictions of several equations with experimental data. It is shown that the effective thermal conductivity of packed beds increases with the Reynolds number (gas velocity). However, for most heterogeneous catalytic reactions,

the small particle size of the catalyst granules required by the diffusion limitations of reactants induces a significant pressure drop at high gas velocities and, correspondingly, a considerably high cost of mechanical energy. As a result, the method of increasing gas velocity to raise the effective thermal conductivity of the packed bed made of catalytic granules is not practical.

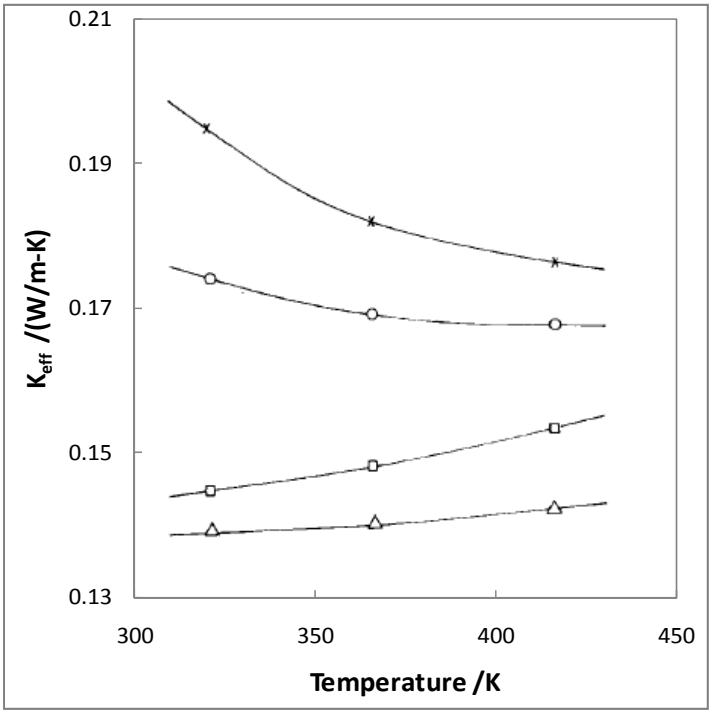

Figure I-13. Effect of temperature on the effective thermal conductivity of packed beds; x--alumina; o--Silica25%+alumina75%; □--Kieselguhr; Δ--Silica [68]

Table I.6 The correlation equations of effective thermal conductivity for packed beds

Author	Radial effective thermal conductivity
Bunnell et al. [70]	$\frac{k_{er}}{k_f} = 5.0 + 0.061 Re_P$
Dixon [71]	$k_{er}\frac{Bi}{Bi+4} = k_f\frac{Bi_f}{Bi_f+4} + k_{rs}\frac{Bi_s}{Bi_s+4}$
Demirel et al. [72]	$\frac{k_{er}}{k_f} = 2.894 + 0.068 Re_P$
Demirel et al. [72]	$\frac{k_{er}}{k_f} = 10.433 + 0.0481 Re_P$
Bey and Eigenberger [73]	$\frac{k_{er}}{k_f} = \frac{k_e^0}{k_f} + 0.1 Re_P Pr$

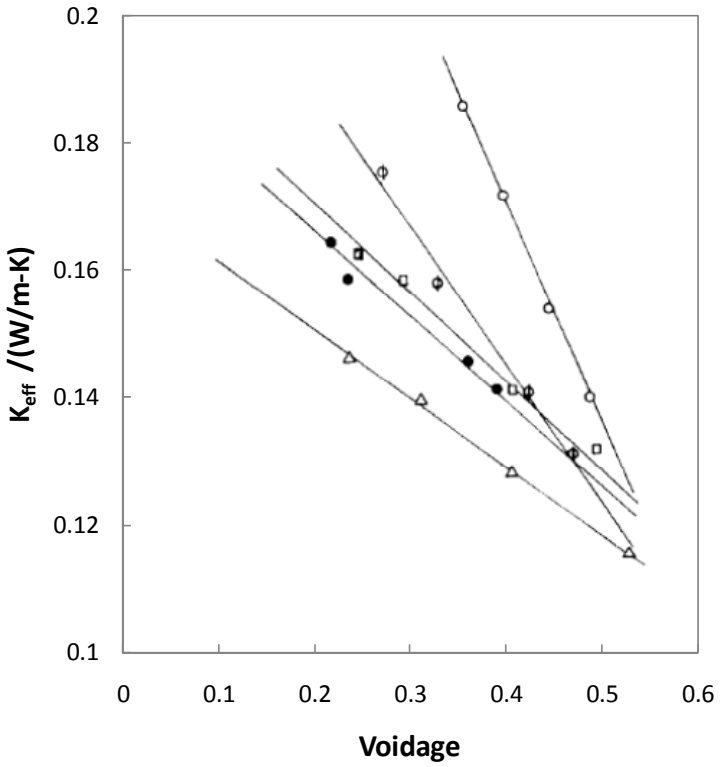

Figure I-14. The effective thermal conductivities of packed beds with the voidages of the intra-particle pores; Δ--silica; ●--5% Ni/silica (impregnated); □--5% Ni/silica (impregnated); ϕ--62% Ni/silica (impregnated); o--62% Ni/silica (copped) [68]

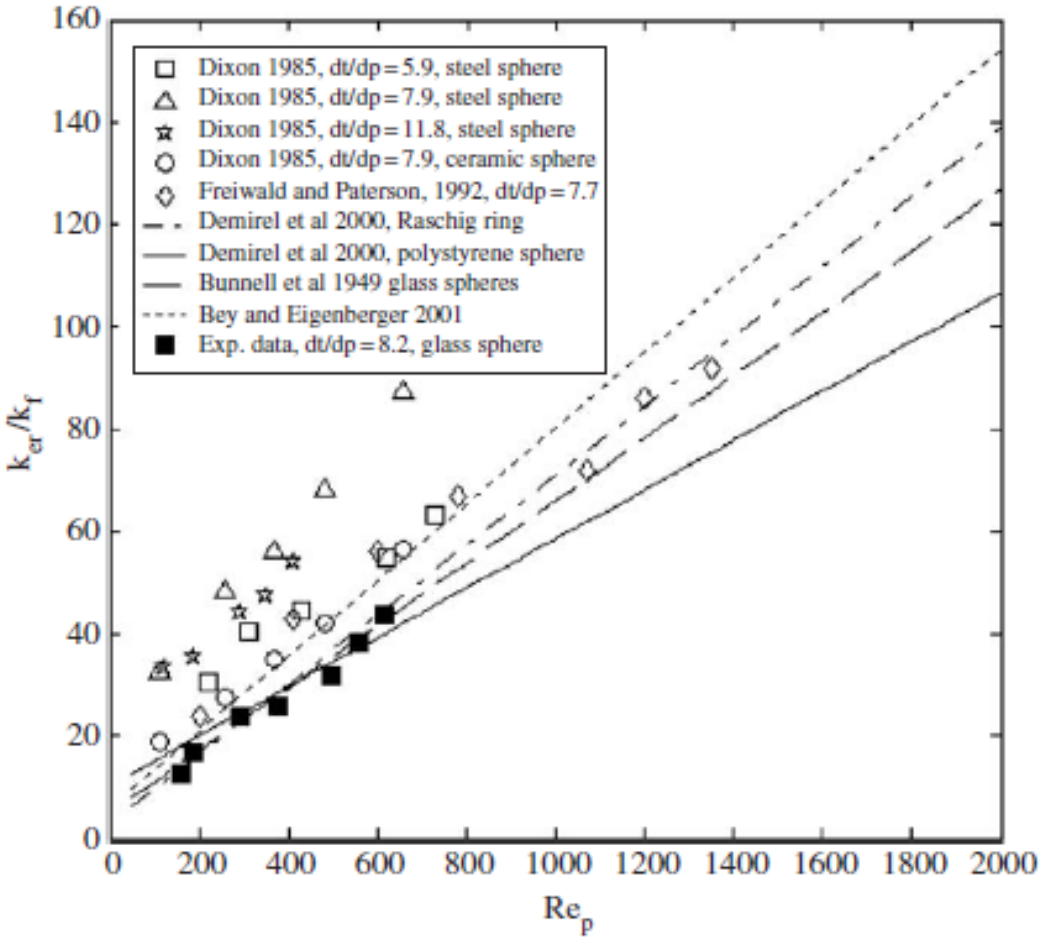

Figure I-15. Comparison of the predictions of several equations with experimental data [74]

The thermal conductivity of syngas with a H_2/CO ratio of 2 at 25°C and 1atm is 0.120W/m-K [75]. Under a typical FTS condition with residual recycled gas in an industrial multitubular fixed bed reactor, the Reynolds number is estimated to be around 50. Because the thermal conductivity of a gas is not affected by pressure except for high vacuums [76],

Demirel's equation [72] gives the effective thermal conductivity of a typical packed bed made of alumina or silica (ceramic) supported catalysts under the FTS condition to be around 0.76W/m-K. Moreover, a liquid phase is also involved in FTS reaction, which further increases the effective thermal

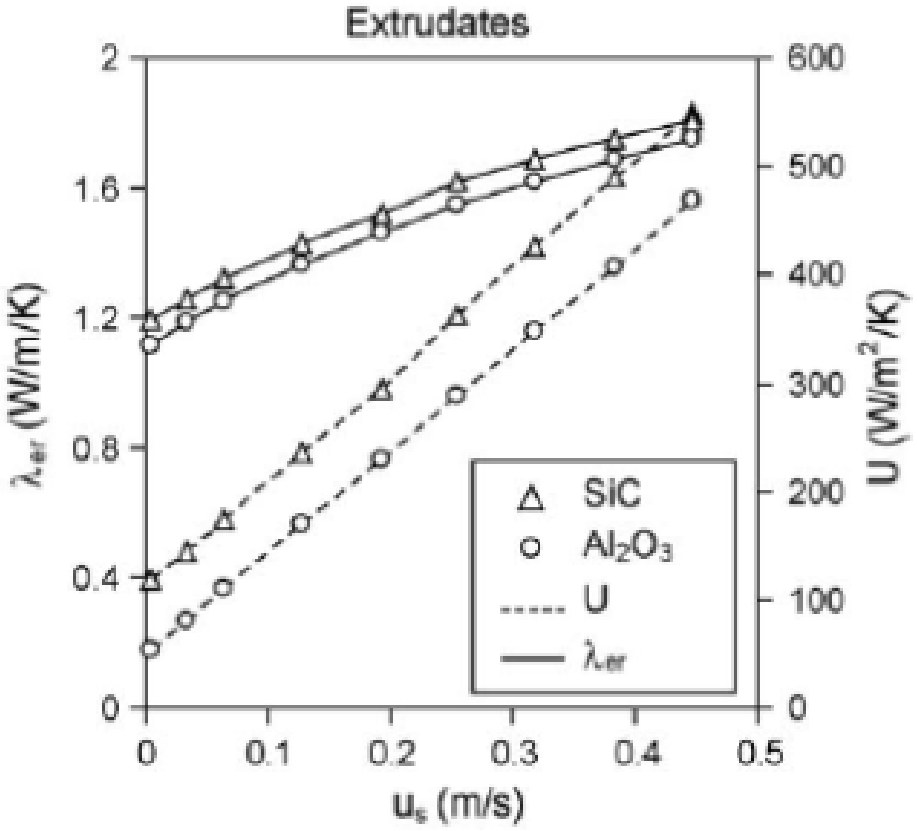

Figure I-16. The radial effective thermal conductivity for FTS catalyst bed [77]

conductivity of the catalyst beds. The heavy FTS products exist as liquids inside the pores of the catalyst supports and form a thin liquid film outside the catalyst particles. At the contact points between catalyst particles, this film forms liquid bridges that decrease the thermal

resistance at the contract points and increase the effective thermal conductivity of catalyst beds. As a result, the effective thermal conductivity of catalyst beds of alumina or silica (ceramic) supported catalysts under the actual FTS condition is higher than 0.76W/m-K. In a study performed by Philippe et al. [77], a range of 1.1~1.8W/m-K was used for the simulation (Figure I.16).

I.8 Summary

The FTS process is an alternative source of liquid fuel that will be used after petroleum reservoirs are depleted or the price of crude oil increases. By employing heterogeneous catalysts, generally iron and cobalt based catalysts, FTS converts syngas, a mixture of hydrogen and carbon monoxide, into a series of hydrocarbon compounds. The product distribution of FTS strongly depends on the temperature of the catalysts, so that a uniform temperature profile through the catalyst beds ensures a high selectivity of the desired heavy products.

It is of crucial importance to control the local temperature of the catalyst beds in the FTS process, because:

1) The product selectivity strongly depends on temperature of the catalyst beds;

2) The reaction rate of FTS is also greatly influenced by the temperature, which worsen the product selectivity;

3) The high temperature of hot spots dramatically accelerates catalyst deactivation.

However, the highly exothermic nature of FTS and the poor heat transfer characteristics of a conventional packed bed made of catalyst granules make fine temperature control difficult.

Therefore, various methods are developed for the design of FTS reactors. The rectangular box reactor and the multiple tubular fixed-bed reactors increase the ratio of heat exchange surface area to catalyst volume. The circulating-gas fixed bed reactor removes the reaction heat from the catalyst bed by recycling a sufficiently large amount of cold residual gas. The Arge tubular fixed bed reactor combines these two methods and works successfully in industrial plants. Several other advanced methods have been studied to improve the heat transfer of fixed bed reactors, such as, supercritical solvent and metallic monolith structured catalyst. Moreover, Fluidized bed reactor and slurry phase reactor provide high heat convection by changing the characteristics of the catalyst bed. They have a remarkable advantage on the removal of reaction heat and success in industrial plants.

However, because they are the simplest to operate and have the highest volumetric catalyst loading, fixed bed reactors remain an attractive option. The poor effective thermal conductivity of packed beds and hence the non-uniform temperature profiles through catalyst beds are still a challenge for large fixed bed reactors used in industrial scale FTS process. Thus, more advanced techniques are desirable to enhance the heat transfer of fixed bed reactors.

The motivation of this work is to apply an enhanced heat transfer catalyst structure (metal microfibrous entrapped catalyst) to the FTS process to improve the heat transfer inside the catalyst bed. Then the hot spot inside the catalyst bed can be avoided, the reactor can be scaled up and a high selectivity of the desired products will still be obtained.

Chapter II: Novel Catalyst Structures with Enhanced Heat Transfer Characteristics

Min Sheng, Hongyun Yang[1], Donald R. Cahela, Bruce J. Tatarchuk

Department of Chemical Engineering, Auburn University, Auburn, AL 36849, USA
[1] IntraMicron Inc., 368 Industry Dr., Auburn, AL 36832, USA

Abstract

Highly exothermic catalytic reactions are problematic from a thermal management perspective and often dictate the type of reactor, heat exchanger, level of conversion/recycle and contacting schemes employed. Those reactions, such as Fischer-Tropsch synthesis (FTS), require catalyst beds with enhanced heat transfer characteristics. Novel catalyst structures, microfibrous entrapped catalyst (MFEC) structures, made of highly conductive metals were compared with traditional packed beds (PB) based on the experimental determinations of thermal parameters and performances in FTS process. Conductive metal MFECs had higher effective thermal conductivities and higher inside wall heat transfer coefficients than PBs including those made of pure copper particles. The radial effective thermal conductivity of copper MFEC was 56-fold higher than that of alumina PB in a stagnant gas, while the inside wall heat transfer coefficient was 10 times higher. The application of copper MFEC in FTS demonstrated a significant improvement of the temperature profiles inside the catalyst beds and an increase in the selectivity of heavy products. Additional advantages such as higher catalyst loading, compatibility with pre-manufactured catalyst particles, and enhanced effective surface

kinetics allow MFEC made of the conductive metals to serve as a potential catalyst structure to enhance the intra-bed heat transfer for highly exothermic or highly endothermic reactions thereby reducing temperature excursions in the reactors.

Keywords: Effective thermal conductivity, microfibrous entrapped catalyst, packed bed, heat transfer, highly exothermic or highly endothermic reaction

II.1 Introduction

Typical packed beds have poor effective thermal conductivity and the size of reactors is limited for highly exothermic and highly endothermic heterogeneous reactions/processes that generate or require a large amount of heat on the surface of catalytic particles. For example, for Fischer-Tropsch synthesis (FTS) with a reaction heat of -165kJ/mol of CH_2 [28] and an adiabatic temperature rise of 1600˚C [29], Van Vuuren [39] reported that the maximum diameter of tubular fixed bed reactors with catalytic granules was 80mm. To address the highly exothermic/endothermic nature, various types of reactors such as fluidized bed reactors [12,41], slurry phase reactors [13,43], metal monolith catalyst structures [47, 48], metallic foams and corrugated packing with open/close cross flow structure [78,79] have been employed. Though experimental and industrial successes of those methods have been achieved, there are still disadvantages or limitations. For instance, the catalyst loadings of fluidized bed reactors and slurry phase reactors are relatively low [9]. Monolith structures [80, 49] and metallic foams [81] need a washcoating process to load catalytic components, which means that they are not suitable for pre-manufactured catalysts. Corrugated packing has been proven to have a poor conductive term to heat transfer [82], so that a gas or liquid recycle is usually applied to increase the convective term to achieve an enhanced heat transfer. A study of thermal parameter determinations and performances in FTS processes reveal a microfibrous entrapped catalyst (MFEC) is a novel enhanced heat transfer catalyst structure that provides a solution to these problems.

The MFEC structures were developed by Auburn University and are now commercially available at IntraMicron Inc., AL. As shown in Figure II.1, MFEC is a microstructured catalyst made of sintered micron-sized metal, glass, or polymer fibers with small catalyst particles entrapped inside [83-88]. MFEC provides a high void volume and an acceptably uniform particle distribution in the media. This high void volume significantly reduces the pressure drop compared to packed beds of similar-size particles. Intra-particle mass/ heat transfers are enhanced by the small particle sizes in this material (e.g., 10 to 100μm dia.) versus typical extrudates used in industrial fixed bed reactors (e.g., 1 to 3mm dia.). Ultra-high contact efficiency also results from the utilization of small particles. To understand the functions of the fibers in the microfibrous media, Kalluri et al. [89] studied the effects on mitigating bed channeling. Yang et al. [90] and Duggirala et al. [91] investigated the effects on external mass transfer in desulfurization by both experiments and CFD modeling. Zhu et al. [92] studied the electrical conductivity of the metal microfibrous sheet in a fuel cell. Ryan Sothen [93] discussed MFEC's pressure drop and effective removal of harmful airborne contaminants in air filtration systems.

However, the thermal property of these structures has not been addressed before. Similar to metal monolith structures, MFEC can be made of highly conductive metals such as copper, brass, and nickel to achieve enhanced heat transfer in the fixed bed reactor. Such a reactor with conductive metal MFEC does not develop hot or cold spots in the catalyst bed and achieves a uniform temperature profile or fine temperature control.

Experimental studies of effective thermal conductivities and inside wall heat transfer coefficients for copper, nickel, and stainless steel (SS) MFECs were compared with those of PBs. In addition, copper MFEC entrapping with 15% Co/Al_2O_3 catalyst particles were tested in the FTS process. The temperature profiles and product selectivity of Cu MFEC were compared with those of PB configurations.

II.2 Materials and methods

II.2.1 Preparation of MFEC

A wet-lay method to prepare MFEC based on traditional high-speed and low-cost paper making techniques was developed by researchers at Auburn University [85-88]. A new method was also developed to prepare the MFEC for pre-manufactured catalyst particles that cannot be applied in metal monolith catalyst structures and metallic foam structures. Herein, all metal MFECs were made of 4μm diameter and 3mm length, and 12μm diameter and 3mm length metal fibers (IntraMicron, Auburn AL, USA). After sintering, the MFEC sheet (Figure II.1) was punched to yield disks sized to stack into the reactor tube. To ensure good contact and avoid dead space between the tube wall and MFEC, the diameter of the MFEC disk was 105% of the I.D. of the tube.

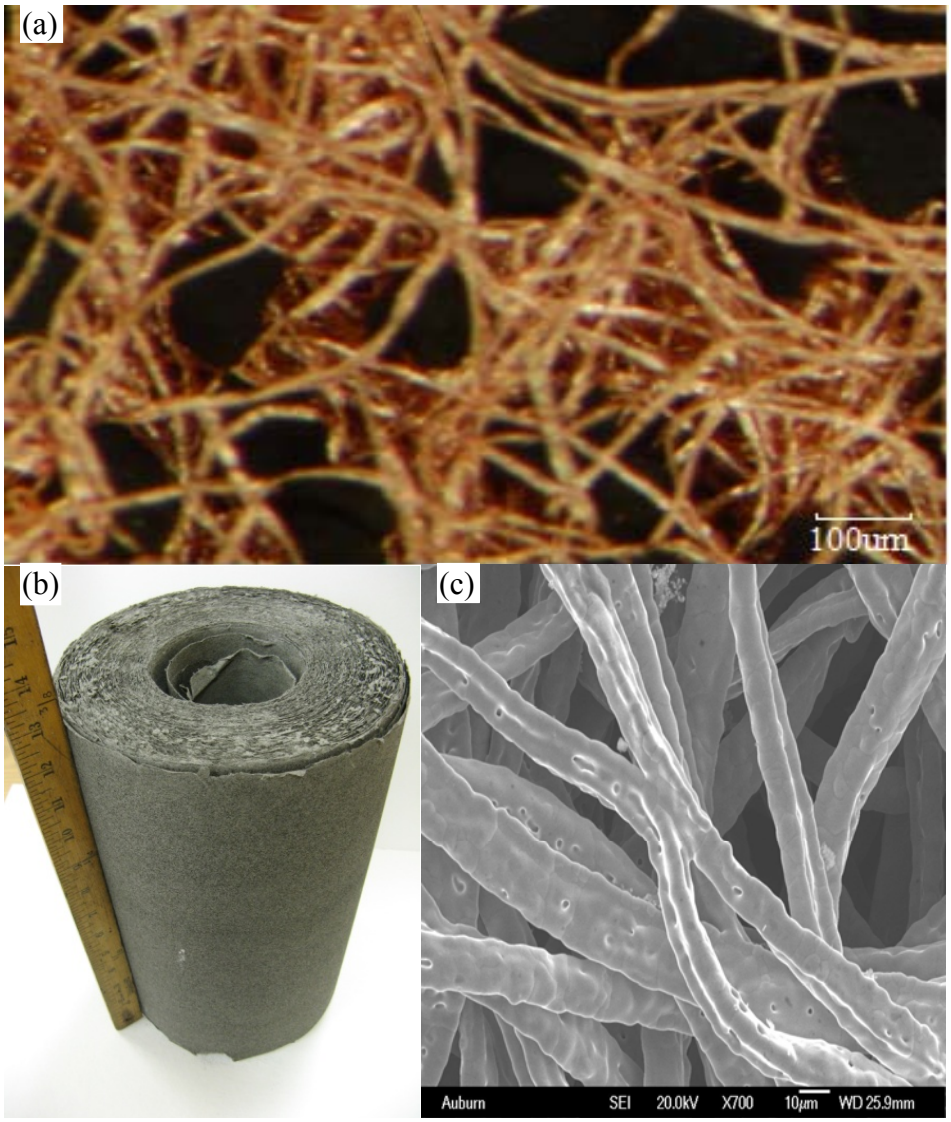

Figure II-1. Pictures of MFECs; (a) 12µm Cu MFEC with FTS catalyst particles, (b) Nickel MFEC roll formed by a paper-making machine, (c) bonding junctions of copper fibers in sample (a).

II.2.2 Thermal Conductivity Determinations

As shown in Figure II.2, tested materials were loaded in the middle section of a 38.1mm O.D. copper tube, which was subsequently immersed into a water bath maintained at constant temperature for all measurements. Fine thermocouples (Omega, 1/32", 0.79mm) were utilized to measure the temperature profiles inside the tested materials. For transient tests , the tube was filled with stagnant N_2 at ambient pressure and no gas was passed through the test tube [94]. At t=0, the test apparatus was put into the water bath, where it was heated from room temperature to the water bath temperature. The heating curves on the midplane were recorded by a data logger (Omega, OM-DAQPRO-5300).

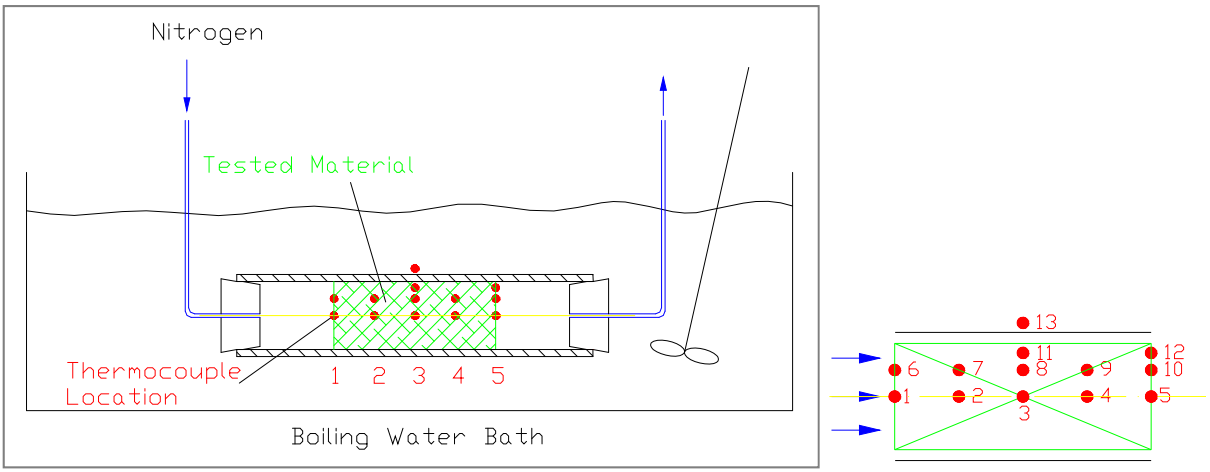

Figure II-2. Apparatus for thermal conductivity measurement (left) and the location of thermocouples (right)

For steady state tests, a N_2 gas stream was fed to the test tube immersed in the water bath. The gas was heated through the tested materials from room temperature. The temperature

profiles inside the materials were measured after the outlet N_2 stream reached a steady temperature. The locations of the thermocouples are shown in Figure II.2.

II.2.3 Samples for Thermal Conductivity Measurement

Copper, nickel, and stainless steel (S.S) MFECs entrapping 180-250μm alumina particles (Alfa, pore volume 1.14cc/g, surface area 245m^2/g) were prepared for thermal conductivity measurements. Packed beds made of copper particles (Alfa, 180–250μm, pore volume 0.22cc/g) and alumina particles of the same size were also evaluated for comparison. The properties of all samples are listed in Table II.1. PB 1 consisted of pure copper particles, PB 4 was made of pure alumina particles, and PB 2 and 3 were mixtures of copper and alumina particles. The copper weight fraction of PB 2 and the copper volume fraction of PB 3 were close to those of Cu MFEC.

Table II.1 Sample properties

		PB 1	PB 2	PB 3	PB 4	Cu MFEC	Ni MFEC	S.S MFEC
Volume %	Metal [1]	33.59	10.81	8.01	0	7.43	4.9	5.67
	Al_2O_3 [2]	0	45.12	53.99	63.89	29.4	18.16	18.01
	Void	66.41[3]	44.07[3]	38[3]	36.11	63.17	76.94	76.32
weight%	Metal [1]	100	75	65	0	76	77	78
	Al_2O_3	0	25	35	100	24	23	22
Packing density g/cc		3.01	1.292	1.1042	0.4363	0.8763	0.5667	0.5821
Volumetric heat capacity J/cc-K		0.8804	0.5677	0.5500	0.3839	0.3799	0.3084	0.3410

Note: 1. Metal: copper particles in PBs; metal fibers in MFECs.
2. Pore volume was included.
3. External void plus internal void of copper powder.

II.2.4 FTS Performances

Cobalt nitrate aqueous solutions were used to prepare 15 wt. % cobalt metal on 180-250μm alumina particles (surface area 255m^2/g, pore volume 1.14cc/g, mean pore size 13.2nm) by incipient wetness impregnation. The catalyst particles were dried at room temperature overnight and calcined at 648K with air flowing for 3hr. The calcined catalyst particles were entrapped into a sintered copper fiber matrix to form a Cu MFEC structure (Figure II.1. a). As illustrated in Figure II.3, circular disks were punched from MFEC to fit the ID of the FTS reactor and a small hole was made at the center of each disk to locate the thermocouple at the centerline of the catalyst bed. The disks (15.9mm in diameter) were 5% bigger in diameter than ID of the reactor tube (15mm), which ensured a good seal at the reactor wall and good contact for a high inside wall heat transfer coefficient. The MFEC were loaded into the reactor and reduced in situ at 638K with flowing hydrogen for 16hr. Syngas with a H_2/CO ratio of 2 and GHSV of 5000/hr was introduced into the reactor to start the FTS process. The pressure was 20bar and the temperature of reactor wall was adjusted.

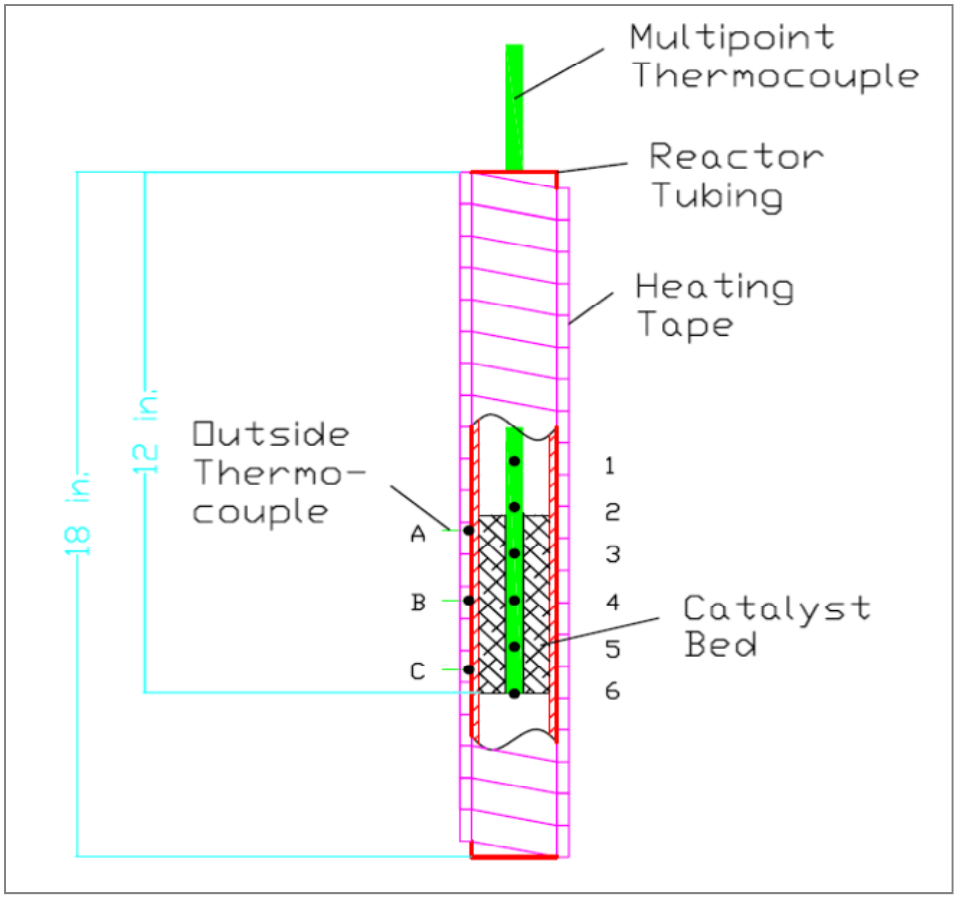

Figure II-3. Diagram of FTS reactor with a multipoint thermocouple at the centerline

For comparison with Cu MFEC, PB with the same 15wt. % cobalt on alumina particles was tested in the same reactor with the same procedure. According to the volume percentage of the catalyst particles in Cu MEFC, PB was diluted with neat alumina particles (180-250μm) to obtain the same catalyst density as the Cu MFEC.

II.3 Estimation of the thermal parameters

Transient methods and steady state methods are widely employed to determine the thermal parameters of porous materials. The transient method based on unsteady radial heat flow was developed by Burke et al. [95] and extended by Waddams [94] by immersing a tube loaded with granulated material in a bath of heated liquid at a uniform temperature while measuring the heating curve on the plane at the middle length of tested material bed. The steady state method involves flowing fluid through porous materials and recording the temperature profiles after a steady state is achieved. This method is used to study the effect of flowing fluids on the thermal parameters of a porous material [96,97], which is a realistic situation inside the heterogeneous catalyst reactors. In either method, it is still a challenge to accurately extract the thermal parameters because of the non-linear relationship between temperature profiles and thermal parameters. One-phase pseudo-homogeneous approaches such as one-dimensional models with effective thermal conductivity and wall heat transfer coefficients [98] and two-dimensional models with radial and axial effective thermal conductivities and wall heat transfer coefficients are popular [99]. Two-phase heterogeneous approaches which are much more expensive to calculate are more practical only if the temperature difference between phases is pronounced.

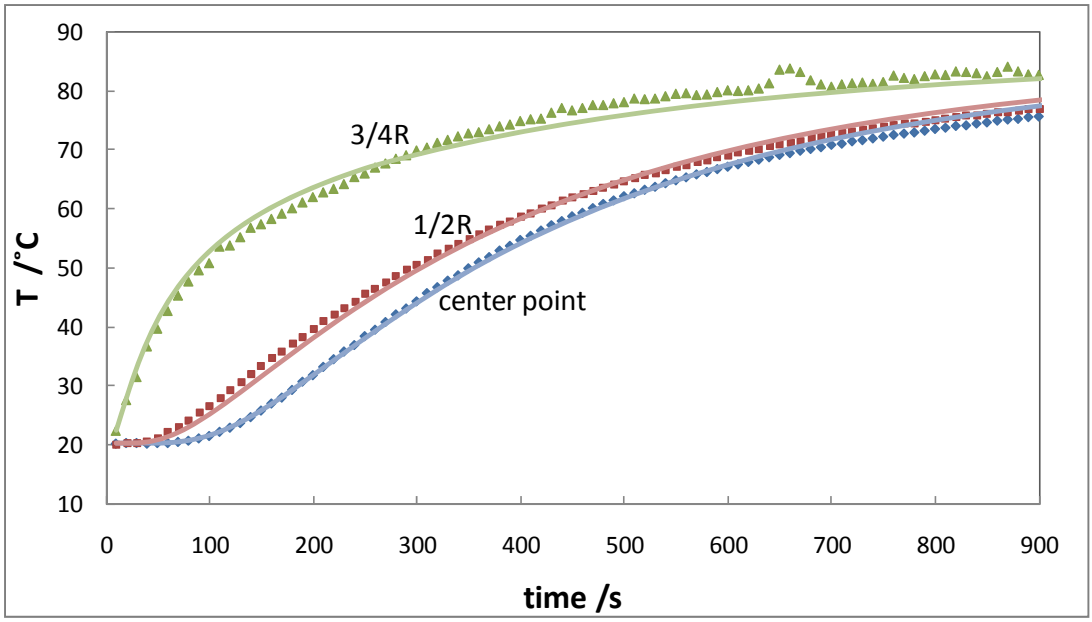

Figure II-4. Temperature-time profile (points) and the numerical fitting result (curves) for PB 3

II.3.1 Transient determination

A pseudo-homogeneous one-dimensional model with radial effective thermal conductivity and an inside wall heat transfer coefficient was used to analyze the data in the transient determinations. The Partial differential equation (PDE) describing the heat transfer inside the material is given by

$$\rho(x_m C_{Pm} + x_{Al} C_{PAl}) \frac{\partial T}{\partial t} = k_{er} \frac{1}{r} \frac{\partial}{\partial r} \left(r \frac{\partial T}{\partial r} \right) \tag{II-1}$$

let $\phi' = \frac{k_{er}}{\rho(x_m C_{Pm} + x_{Al} C_{PAl})}$, then

$$\frac{\partial T}{\partial t} = \phi' \left(\frac{1}{r} \frac{\partial T}{\partial r} + \frac{\partial^2 T}{\partial r^2} \right) \tag{II-2}$$

Apply implicit Euler method to discretize the PDE above:

$$\frac{T_i^n - T_i^{n-1}}{\Delta t} = \phi' \left(\frac{1}{(i-1)\Delta r} \frac{T_{i+1}^n - T_{i-1}^n}{2\Delta r} + \frac{T_{i+1}^n - 2T_i^n + T_{i-1}^n}{\Delta r^2} \right) \quad \text{(II-3)}$$

or

$$T_i^n - T_i^{n-1} = \frac{\phi' \Delta t}{r_{id}^2 \Delta \zeta^2} \left(T_{i-1}^n \left(1 - \frac{1}{2(i-1)} \right) - 2T_i^n + T_{i+1}^n \left(1 + \frac{1}{2(i-1)} \right) \right) \quad \text{(II-4)}$$

let $\lambda = \frac{\phi' \Delta t}{r_{id}^2 \Delta \zeta^2}$, then

$$T_{i-1}^n \left(\frac{1}{(i-1)} - 2 \right) \lambda + T_i^n (2 + 4\lambda) - T_{i+1}^n \left(2 + \frac{1}{(i-1)} \right) \lambda = 2T_i^{n-1} \quad \text{(II-5)}$$

Boundary conditions 1:

$$@\ r = 0\ (i = 1) \qquad \frac{\partial T}{\partial r} = 0 \quad \text{(II-6)}$$

$$\text{then } \frac{3T_1^n - 4T_2^n + T_3^n}{2\Delta r} = 0 \quad \text{or } T_1^n = \frac{4}{3} T_2^n - \frac{1}{3} T_3^n \quad \text{(II-7)}$$

Substitute T_1^n into Eq.II-5 when i=2,

$$\left(\frac{4}{3} T_2^n - \frac{1}{3} T_3^n \right)(1 - 2)\lambda + T_2^n (2 + 4\lambda) - T_3^n (2 + 1)\lambda = 2T_2^{n-1}$$

$$\text{Or } T_2^n \left(2 + \frac{8}{3} \lambda \right) - T_3^n \frac{8}{3} \lambda = 2T_2^{n-1} \quad \text{(II-8)}$$

Boundary conditions 2:

$$@\ r = r_{id} (i = N + 1) \qquad k_{er} \frac{\partial T}{\partial r} = h_w (T_w - T)$$

Or $k_{er}\frac{T_{N-1}^{n}-4T_{N}^{n}+3T_{N+1}^{n}}{2r_{id}\Delta\zeta}=h_{w}(T_{w}-T_{N+1}^{n})$ (II-9)

For the tube wall, $k_{w}\frac{\partial T}{\partial r}=k_{w}\frac{(T_{\infty}-T_{w})}{r_{id}ln\frac{r_{od}}{r_{id}}}$ (II-10)

at $r=r_{id}$ $k_{er}\frac{\partial T}{\partial r}=k_{w}\frac{(T_{\infty}-T_{w})}{R_{id}ln\frac{r_{od}}{r_{id}}}$

or $k_{er}\frac{T_{N-1}^{n}-4T_{N}^{n}+3T_{N+1}^{n}}{2r_{id}\Delta\zeta}=k_{w}\frac{(T_{\infty}-T_{w})}{r_{id}ln(\frac{r_{od}}{r_{id}})}$ (II-11)

then $T_{W}=T_{\infty}-\ln(\frac{r_{od}}{r_{id}})\frac{k_{er}}{k_{w}}\frac{1}{2\Delta\zeta}(T_{N-1}^{n}-4T_{N}^{n}+3T_{N+1}^{n})$ (II-12)

substitute Eq.II-11 into Eq.II-8:

$\frac{T_{N-1}^{n}-4T_{N}^{n}+3T_{N+1}^{n}}{2\Delta\zeta}=\frac{h_{w}r_{id}}{k_{er}}\left[T_{\infty}-T_{N+1}^{n}-\ln(\frac{r_{od}}{r_{id}})\frac{k_{er}}{k_{w}}\frac{1}{2\Delta\zeta}(T_{N-1}^{n}-4T_{N}^{n}+3T_{N+1}^{n})\right]$ (II-13)

let $Bi=\frac{h_{w}r_{id}}{k_{er}}$ then

$T_{N+1}^{n}=\frac{2Bi\cdot T_{\infty}\Delta\zeta+(4T_{N}^{n}-T_{N-1}^{n})\cdot\left[Bi\cdot\ln(\frac{r_{od}}{r_{id}})\frac{k_{er}}{k_{w}}+1\right]}{2Bi\cdot\Delta\zeta+3\left[Bi\cdot\ln(\frac{r_{od}}{r_{id}})\frac{k_{er}}{k_{w}}+1\right]}$ (II-14)

Substitute T_{N+1}^{n} into Eq.II-5 when i=*N*,

$$T_{N-1}^{n}\lambda\left[\frac{1}{(N-1)}-2+\left(2+\frac{1}{(N-1)}\right)\cdot\frac{Bi\cdot\ln(\frac{r_{od}}{r_{id}})\frac{k_{er}}{k_{w}}+1}{2Bi\cdot\Delta\zeta+3\left[Bi\cdot\ln(\frac{r_{od}}{r_{id}})\frac{k_{er}}{k_{w}}+1\right]}\right]+T_{N}^{n}\left[2+4\lambda-4\lambda\left(2+\right.\right.$$

1(N−1)·Bi·ln *(rodrid)kerkw+12Bi·Δζ+3Bi*·ln *(rodrid)kerkw+1=2TNn−1+λ2+1(N −1)2Bi·T∞Δζ2Bi·Δζ+3Bi*·ln *(rodrid)kerkw+1* (II-15)

Combine Eq.II-5, Eq.II-7 and Eq.II-14 to obtain the system equation:

$$\begin{vmatrix} 2+\frac{8}{3}\lambda & -\frac{8}{3}\lambda & 0 & 0 & 0 \\ (\frac{1}{3-1}-2)\lambda & 2+4\lambda & -(\frac{1}{3-1}+2)\lambda & 0 & 0 \\ 0 & . & . & . & 0 \\ 0 & 0 & (\frac{1}{N-2}-2)\lambda & 2+4\lambda & -(\frac{1}{N-2}+2)\lambda \\ 0 & 0 & 0 & A & B \end{vmatrix} \cdot \begin{vmatrix} T_2^n \\ T_3^n \\ . \\ T_{N-1}^n \\ T_N^n \end{vmatrix} = 2 \cdot \begin{vmatrix} T_2^{n-1} \\ T_3^{n-1} \\ . \\ T_{N-1}^{n-1} \\ C \end{vmatrix} \qquad \text{(II-16)}$$

With 40 divisions on the radial direction, the PDE describing the transient tests was discretized by a central finite difference scheme and integrated by the Euler implicit method [100]. A Newton-Raphson search algorithm was used to determine k_{er} and h_w in the PDE equations by fitting the heating curves from three thermocouples labeled 3, 8, and 11, located at the center, R/2, and 3R/4 on the midplane, respectively. For example, in Figure II.4, the heating curves of PB 3 were fitted using the PDE equation with k_{er} =0.182W/m-K and h_w =53.7W/m^2-K. As a result, this nonlinear regression provided estimations of the radial effective thermal conductivity, k_{er}, and the inside wall heat transfer coefficient, h_w, for all samples. Standard deviations for the parameters corresponding to a ninety-five percent confidence interval were estimated by linearized statistics [101].

II.3.2 Steady state determination

A pseudo-homogeneous two-dimensional model was used to calculate radial and axial effective thermal conductivities and the inside wall heat transfer coefficient for the steady state measurements. All thermocouples shown in Figure II.2 (left) were fitted except points 1 and 6,

which served as a boundary condition and the initial condition, respectively. The PDE for the heat transfer phenomena inside the media is given by:

$$\left(\varepsilon\rho_f C_{Pf} + (1-\varepsilon)\rho_s C_{Ps}\right)\frac{\partial T}{\partial t} + \rho_f C_{Pf} v_z \frac{\partial T}{\partial z} = k_{er}\frac{1}{r}\frac{\partial}{\partial r}\left(r\frac{\partial T}{\partial r}\right) + k_{ez}\frac{\partial^2 T}{\partial z^2} \quad \text{(II-17)}$$

Let $\varphi' = \frac{\rho_f C_{Pf} v_z}{(\varepsilon\rho_f C_{Pf}+(1-\varepsilon)\rho_s C_{Ps})}$, $\phi'_r = \frac{k_{er}}{(\varepsilon\rho_f C_{Pf}+(1-\varepsilon)\rho_s C_{Ps})}$, $\phi'_z = \frac{k_{ez}}{(\varepsilon\rho_f C_{Pf}+(1-\varepsilon)\rho_s C_{Ps})}$

$$\frac{\partial T}{\partial t} + \varphi'\frac{\partial T}{\partial z} = \phi'_r\left(\frac{1}{r}\frac{\partial T}{\partial r} + \frac{\partial^2 T}{\partial r^2}\right) + \phi'_z\frac{\partial^2 T}{\partial z^2} \quad \text{(II-18)}$$

Apply explicit Euler method to discretize this PDE:

$$\frac{T_{i,j}^{n+1}-T_{i,j}^{n}}{\Delta t} + \varphi'\frac{T_{i,j+1}^{n}-T_{i,j-1}^{n}}{2L\Delta x} =$$

$$\phi'_r\left(\frac{1}{r_{id}\Delta\zeta(i-1)}\frac{T_{i+1,j}^{n}-T_{i-1,j}^{n}}{2r_{id}\Delta\zeta} + \frac{T_{i+1,j}^{n}-2T_{i,j}^{n}+T_{i-1,j}^{n}}{r_{id}^2\Delta\zeta^2}\right) + \phi'_z\frac{T_{i,j+1}^{n}-2T_{i,j}^{n}+T_{i,j-1}^{n}}{L^2\Delta x^2} \quad \text{(II-19)}$$

Then

$$T_{i,j}^{n+1} = T_{i-1,j}^{n}\left[\frac{\phi\prime_r\Delta t}{r_{id}^2\Delta\zeta^2} - \frac{\phi\prime_r\Delta t}{2(i-1)r_{id}^2\Delta\zeta^2}\right] + T_{i,j-1}^{n}\left[\frac{\phi\prime_z\Delta t}{L^2\Delta x^2} + \frac{\varphi\prime\Delta t}{2L\Delta x}\right] + T_{i,j}^{n}\left[1 - \frac{2\phi\prime_r\Delta t}{r_{id}^2\Delta\zeta^2} -\right.$$

$$\left.2\phi'z\Delta tL2\Delta x2+Ti+1,jn\phi'r\Delta trid2\Delta\zeta2+\phi'r\Delta t2(i-1)rid2\Delta\zeta2+Ti,j+1n\phi'z\Delta tL2\Delta x2-\varphi'\Delta t2\right.$$

$$L\Delta x \quad \text{(II-20)}$$

Boundary condition 1:

$$@\ r = 0(i=1)\ , \quad \frac{\partial T}{\partial r} = 0 \quad \text{or} \quad T_1^{n+1} = \frac{4}{3}T_2^{n+1} - \frac{1}{3}T_3^{n+1} \quad \text{(II-21)}$$

Boundary condition 2:

$$@ = r_{id}(i=N+1)\ , \quad k_{er}\frac{\partial T}{\partial r} = h_w(T_w - T) \quad \text{(II-22)}$$

$$T_{N+1}^{n+1} = \frac{2Bi \cdot T_{\infty} \Delta\zeta + (4T_N^{n+1} - T_{N-1}^{n+1}) \cdot \left[Bi \cdot \ln\left(\frac{r_{od}}{r_{id}}\right) \frac{k_{er}}{k_w} + 1 \right]}{2Bi \cdot \Delta\zeta + 3\left[Bi \cdot \ln\left(\frac{r_{od}}{r_{id}}\right) \frac{k_{er}}{k_w} + 1 \right]} \quad \text{(II-23)}$$

Boundary condition 3:

$$@ = 0 (j = 1)\ ,\ T = T_1 \ \& \ T_6 \quad \text{(II-24)}$$

Boundary condition 4:

$$@ = L (j = M + 1)\ ,\quad \frac{\partial T}{\partial z} = 0 \quad \text{or} \quad T_{M+1}^{n+1} = \frac{4}{3} T_M^{n+1} - \frac{1}{3} T_{M-1}^{n+1} \quad \text{(II-25)}$$

The PDE was discretized using central finite difference formulas and integrated by the Euler explicit method [100] from initial condition to steady state. Forty divisions in the radial direction and 20 in the axial direction were employed to mesh the domain. Von Neumann analysis showed that this scheme was conditionally stable with a courant number smaller than 0.5. The thermal parameters, k_{er}, k_{ez} and h_w, were determined by fitting the experimental temperature profiles with Newton-Raphson search algorithms. Standard deviations of the parameters were estimated using the same method as that used in the transient data [101]. The standard deviations of k_{er} were smaller than 10%, and the standard deviations of h_w were less than 25%. A higher uncertainty of h_w was observed for low gas flow rate cases because less data was collected and a smaller temperature gradient was used.

II.4 Results and discussion

II.4.1 Effective Thermal Conductivity

II.4.1.1 Transient measurements

For transient tests, the length of the tested material bed was about 152.4mm, which was four times the tube diameter. According to Waddams [94] and Kozlov [102], the effect of axial heat flow at the midplane can be eliminated because the bed was of adequate length. Thus, the temperature increase of the material at midplane during the transient heat-up process only resulted from the heat transfer along the radial direction. The one-dimensional homogeneous model was valid for fitting the heating curves on the midplane. The heating curves at the center point on the midplane (point 3) of seven samples are presented in Figure II.5. PB 4 and Cu MFEC had similar volumetric heat capacities (Table II.1), but the temperature rise of Cu MFEC was much faster than that of PB 4. This difference was quantified by the nonlinear regression results. As shown in Figure II.6, the MFEC made of copper fibers had a thermal conductivity of 9.05 W/m-K, which was fifty-five times higher than that of a packed bed made of alumina particles (0.16 W/m-K) and thirty eight times higher than that of a pure copper particle bed (0.23 W/m-K). As shown in Figure II.7, the inside wall heat transfer coefficient of Cu MFEC (235W/m^2-K) was ten times of that of an alumina packed bed (22.7 W/m^2-K) and two times of that of a copper particle bed (125 W/m^2-K). The MFECs made of S.S and nickel also demonstrated high effective thermal conductivities of 1.395 and 3.774W/m-K, respectively. The effective thermal conductivities of PBs were much lower than that of Cu

MFEC, even with the higher volume percentage of metal in PBs. Therefore, the improvement of thermal conductivity was an effect of a sinter-locked network of metal fibers in the MFEC structure as shown in Figure II.1.c. This kind of structure provided continuous metal channels or bridges for heat conduction, which were much more effective than the point contacts in powder PBs.

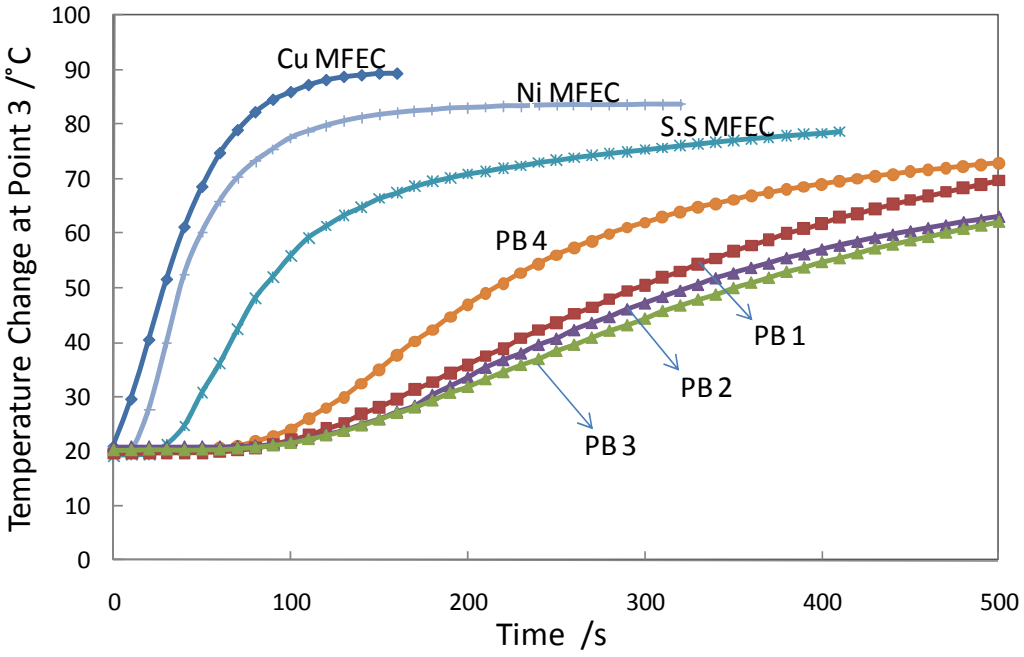

Figure II-5. Temperature-time profiles of center points during transient measurements

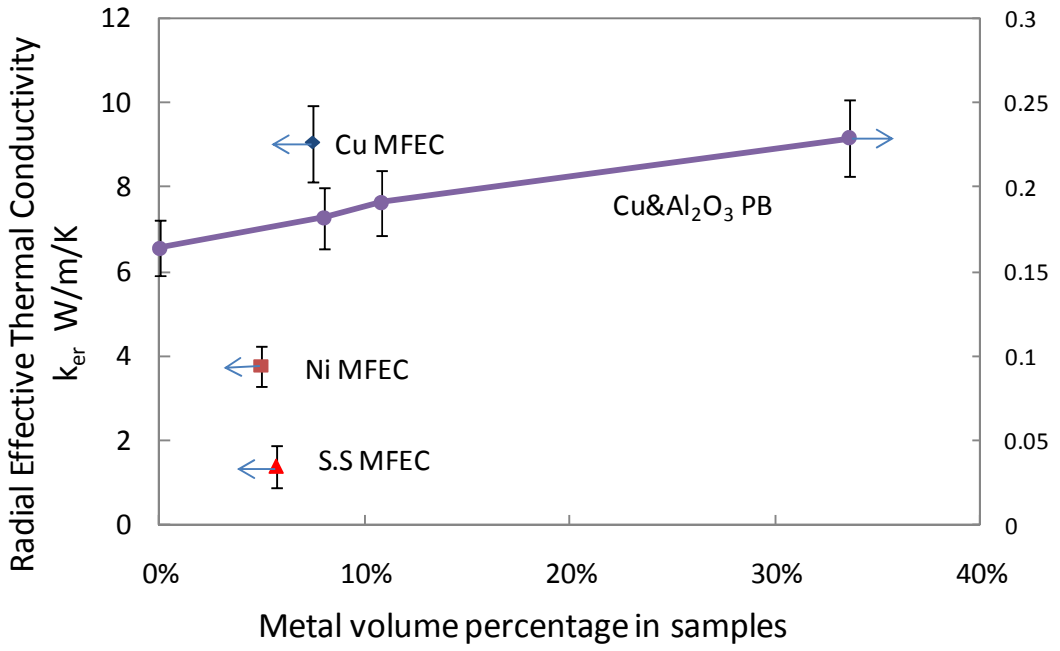

Figure II-6. Radial effective thermal conductivity for MFECs and Packed Beds extracted from the numerical fitting of transient measurements, standard deviation in 10~15%

In Figure II.6 and7, data for PBs 1 to 4 were connected as a curve because they were all packed beds of various fractions of copper particles and alumina particles. The effective thermal conductivities of a pure alumina bed (PB 4) and that of a pure copper particle bed (PB 1) were consistent with data found in the literature [102, 103, 104]. The effective thermal conductivity of the packed beds increased slightly with the copper volume, while all the MFECs demonstrated higher thermal conductivities than any packed bed. However, the inside wall heat transfer coefficient of packed beds increased rapidly with the copper volume. This means that the introduction of copper metal improved the heat transfer through the interface between the reactor wall and catalyst bed. The Cu MFEC showed a higher wall heat transfer

coefficient than that of any packed bed, which suggests that Cu MFEC was superior to copper particle diluted beds in heat transfer behavior. Therefore, metal MFEC efficiently increased thermal parameters of the catalyst bed. The combination of high thermal conductivity and a high inside wall heat transfer coefficient enhanced the intra-bed heat transfer for highly exothermic or highly endothermic reactions when the entrapped alumina particles were loaded with precious metals as active catalytic compounds.

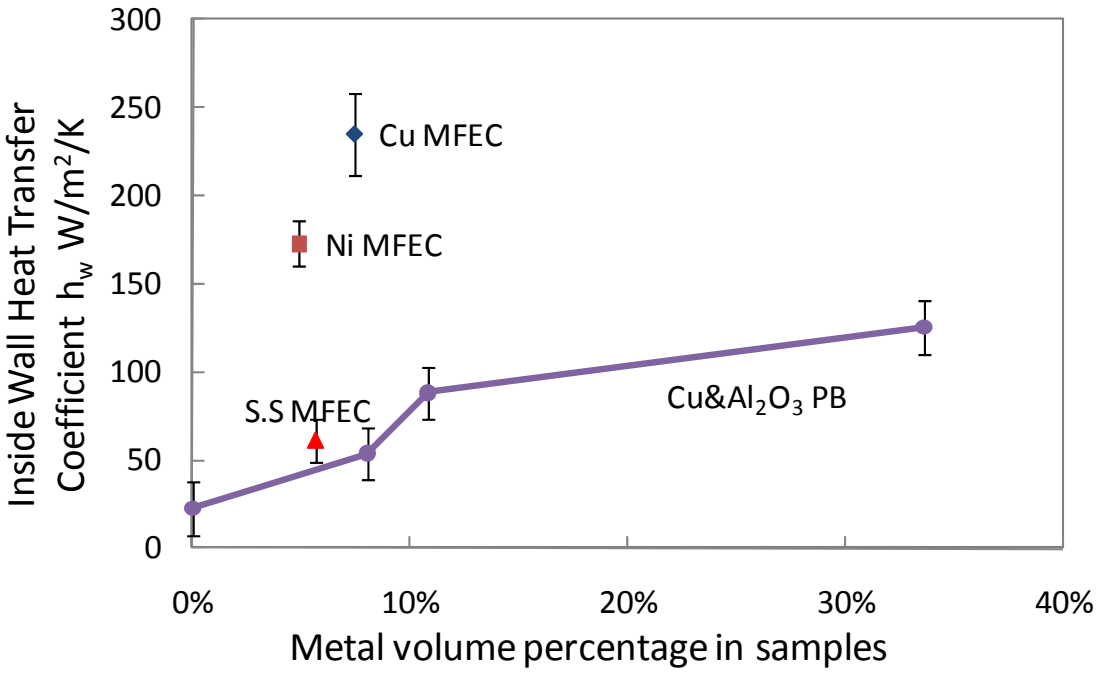

Figure II-7. Inside wall heat transfer coefficient for MFECs and Packed Beds extracted from the numerical fitting of transient measurements, standard deviation in 15~20%

II.4.1.2 Steady State Measurement

For the steady state thermal conductivity measurements, only 76.2mm of the test material was loaded in the copper tube. Assuming homogeneity, thermal parameters, k_{er}, k_{ez} and h_w, were estimated by fitting the temperature profiles. Figure II.8 and 9 show the evaluation of radial effective thermal conductivity, k_{er}, of seven samples at different N_2 gas velocities. Re is calculated by

$$Re = \frac{\rho v D_p}{\mu(1-\varepsilon)} \tag{II-26}$$

where D_p is the equivalent diameter of the sample, given by

$$\frac{1}{D_p} = \frac{S_p}{6V_p} = \sum \frac{y_i}{\varphi_i D_i} \tag{II-27}$$

As compared with those of PBs, the radial effective thermal conductivities of MFEC increased much faster with gas velocity. The high thermal conductivity for MFEC was thought to be caused by co-enhanced interaction of the high conductive contribution from continuous metal channels and the high convective contribution from a high geometric surface area. Because micron-sized fibers offered a large surface area, MFEC had a higher volumetric geometric surface area than PBs (58,080m^{-1} for Cu MFEC and 17,670m^{-1} for alumina PB). The extra geometric surface area of MFEC contributed to the dramatic increase of thermal conductivity. In addition, a poor thermal conductive term as in S.S MFEC limited this trend and resulted in a small increase in the thermal conductivity. Therefore, the combination of the high conduction and high convection contributions accounted for the large increase in radial effective thermal conductivity of MFEC with higher gas velocity.

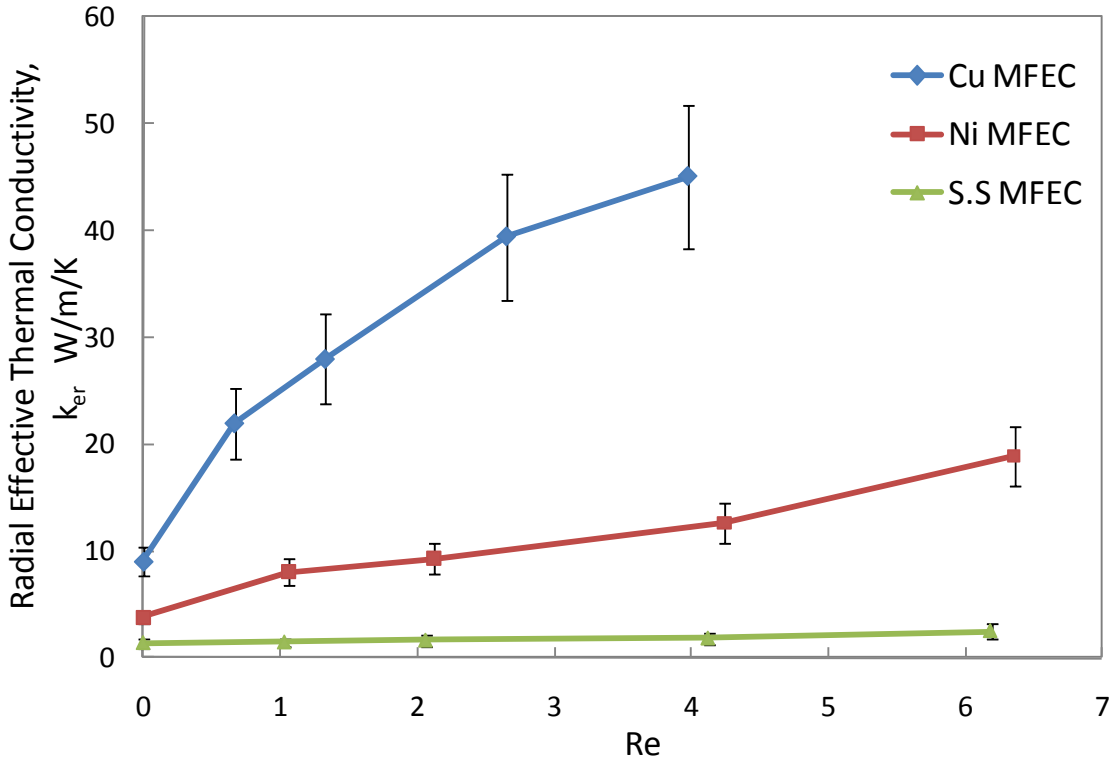

Figure II-8. Radial effective thermal conductivity for MFECs extracted from the numerical fitting of steady state measurements, standard deviation in 15~20%

Axial thermal conductivity was also determined from the analysis of steady state measurements.

The axial thermal conductivity agreed with the equation used by others [105, 106].

$$k_{ez} = k_{ez}^{0} + 0.5 R_e P_r k_f \qquad \text{(II-28)}$$

where k_{ez}^{0} is the axial effective thermal conductivity with a stagnant gas. For the PBs whose macro-structure was identical in the axial and the radial direction, k_{ez}^{0} was equal to the stagnant radial effective thermal conductivity calculated from the transient measurement. For example,

for PB 1 (Figure II.10) the intercept of the tendency line, the stagnant axial effective thermal conductivity was 0.2194W/m-K. This was very close to the value of radial effective thermal conductivity obtained from the transient test (0.2291W/m-K). However, the intercepts of MFECs (0.947, 0.762, and 0.663W/m-K) were much lower than the stagnant radial effective thermal conductivities obtained from the transient measurements (9.05, 3.774, and 1.395W/m-K for Cu, Ni, and S.S MFEC, respectively). The preference of fiber orientations in MFECs prepared by wet-lay

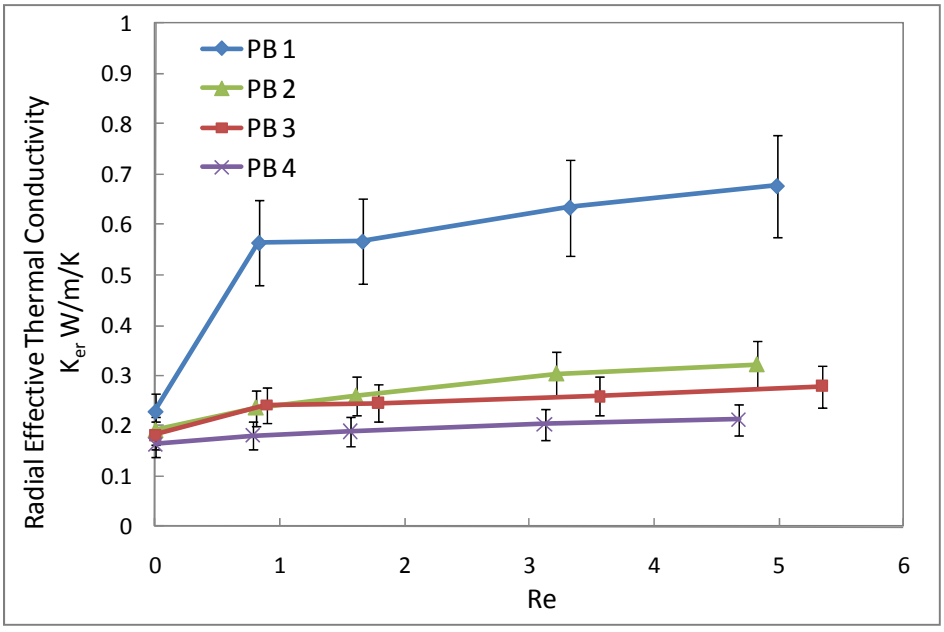

Figure II-9. Radial effective thermal conductivity for Packed Beds extracted from the numerical fitting of steady state measurements, standard deviation in 15~20%

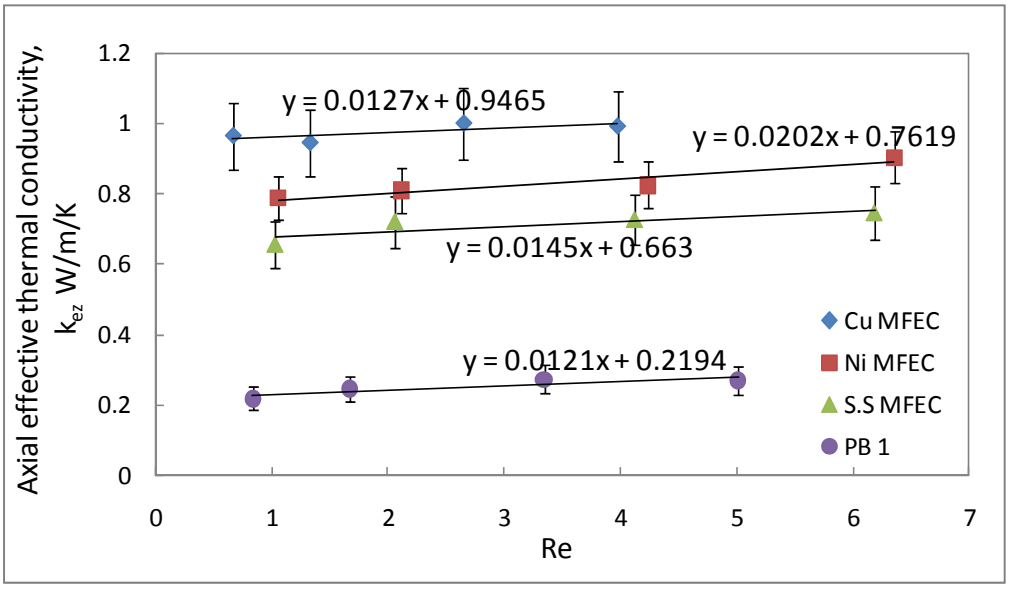

Figure II-10.Axial effective thermal conductivity extracted from the numerical fitting of steady state measurements, standard deviation in 15~20%

manufacture and the separated disks stacked in the tube explained the large differences between axial and radial thermal conductivities. During wet-lay manufacture, when water was drained off through the bottom of the hand sheet model and a metal-cellulose sheet was formed, metal fibers sedimented freely onto the screen where most of the fibers preferentially oriented in the x-y plane. Thus, few metal fibers were oriented in the axial direction in MFEC and most were oriented in the radial direction. In addition, the MFEC materials were prepared as separated disks with 0.4~2mm thickness and were stacked into the tube one by one. Therefore, MFEC did not offer a continuous metal channel in the axial direction as it did in the

radial direction. This resulted in the radial thermal conductivity of Cu MFEC being much higher than the axial thermal conductivity. Because of its direction-dependent thermal properties, extra attention is needed during the loading of the MFEC into the reactor to make use of the high radial thermal conductivity or the high axial thermal resistance.

II.4.2 Inside Wall Heat Transfer Coefficient

The inside wall heat transfer coefficient is also an important parameter that determines heat transfer inside the reactor. The temperature difference between the catalyst bed and the wall of the reactor depends on the thermal resistance between them, which is affected by materials and the contact conditions. Poor inside wall heat transfer is the bottleneck of the metal monolith in highly exothermic and highly endothermic reactions [107]. Because the monolith structure has a smaller diameter than the ID of the reactor, contact between the monolith and the reactor wall is usually poor and the inside wall heat transfer coefficient is low. MFEC is more flexible, which allows it to be corrugated and shaped, and is usually prepared as sheets with a diameter 3~8% bigger than the ID of reactor. Therefore, good contact between MFEC and the inside wall of the reactor can be achieved yielding a high inside wall heat transfer coefficient.

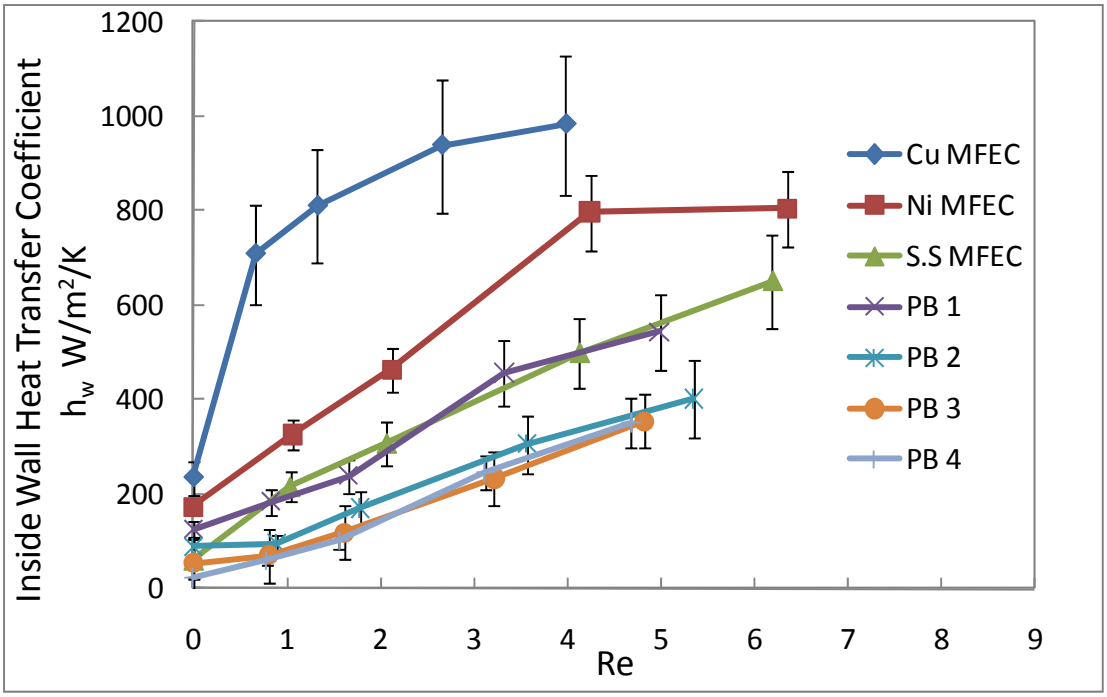

Figure II-11. Inside wall heat transfer coefficient extracted from the numerical fitting of transient and steady state measurements, standard deviation in 15~25%

Although higher uncertainties were shown in the analysis, the results are demonstrated in Figure II.7 and Figure II.11. The inside wall heat transfer coefficients of Cu and Ni MFEC were larger than those of PBs. For stagnant conditions, the heat conduction between the tube wall and the solid phase was the main contributor to the inside wall heat transfer coefficient, which was improved by introducing a metal such as copper into the alumina packed bed. For gas flowing conditions, the convective heat transfer term became more significant such that the inside wall heat transfer coefficient of all samples increased with gas velocity. With the same metal volume percentage, the inside wall heat transfer coefficient of Cu MFEC was higher than that of PB 3. It is possible that some copper fibers in Cu MFEC were compressed against the

wall providing contact with the edge. This would allow efficient heat transfer through the interface between MFEC and the wall. In contrast, the copper particle bed only had point contacts and promoted less efficient heat transfer.

II.4.3 FTS

Copper metal was reported to reduce the selectivity of heavy products in the FTS reaction with cobalt base catalysts [108]. Therefore, a Co/Al_2O_3 catalyst or the Al_2O_3 support must be isolated from the paper-making process and sintering of the copper fiber matrix to prevent copper contamination of the catalyst. This new method to prepare MFEC enables loading the pre-manufactured catalyst, calcined Co/Al_2O_3 particles, into a pre-sintered copper fiber matrix to form Cu MFEC structures. The advantage of this method was that the washcoating process required in monolith and metallic foams was eliminated. In addition, this method avoids the decomposition of copper on the surface of Al_2O_3 support during the sintering of fiber matrix. This maintains the original surface chemistry composition of the entrapped catalyst, as well as its activity and selectivity. Furthermore, intra-particle mass transfer was enhanced because of the small particle sizes used in this structure as compared with typical extrudates used in industrial fixed bed reactors. Hence, a high reaction rate was maintained in the catalyst bed, which required a catalyst structure with enhanced heat transfer characteristics to transport the reaction heat from catalytic sites to the cooling surface.

In the FTS process, without the gas/liquid recycling, the gas superficial velocity is usually small because of the high pressure conditions (superficial velocity was 0.92mm/s) such that the convective contribution of the heat transfer was minimized. Additionally, at the front

of the catalyst bed, where the highest reaction rate occurs (assuming no deactivation) and the highest heat is generated, the amount of the liquid product is small and conduction through the liquid phase is limited. Therefore, a catalyst structure with enhanced heat transfer characteristics is required. For PB, the effective thermal conductivity of alumina particles was only 0.16W/m-K in stagnant N_2 gas. In addition, the corrugated packing was reported to have an effective radial thermal conductivity between 1 and 2W/m-K [82]. In contrast, the effective thermal conductivity of copper MFEC was about 9.05W/m-K. Therefore, copper MFEC was expected to yield an improvement over typical packed bed structure in the intra-bed heat transfer inside the catalyst bed.

Table II.2 Temperature and selectivity of FTS test with two types of catalysts at 20bar, H2/CO ratio 2 and 5000/hr GHSV

Day	T_{wall} /°C	Highest T/°C		Conver-sion	Cobalt-time-yield	Selectivity	
		T	T-T_{wall}		10^{-3}mol_CO/mol_cobalt/s	α value	C_{5+}
PB, Co/Al_2O_3, diluted with fresh Al_2O_3							
1	225	230.7	5.7	0.357	3.32	0.834	0.797
2	235	243.1	8.1	0.534	4.96	0.819	0.734
3	245	259.7	14.7	0.87	8.09	0.725	0.506
4	255	325.2	70.2	1	9.29	0.151[1]	0.124
5	235	237.1	2.1	0.183	1.70	0.822	0.753
Cu MFEC, entrapping Co/Al_2O_3, 7.4vol%Cu, 29vol%Al_2O_3							
1	225	224.6	-0.4	0.151	1.40	0.852	0.821
2	235	237.8	2.8	0.387	3.62	0.831	0.793
3	245	250	5	0.516	4.80	0.815	0.738
4	255	264.4	9.4	0.789	7.33	0.797	0.702
5	235	237.6	2.6	0.371	3.45	0.836	0.801

Note: 1, run away, α value based on methane selectivity

FTS reactions with PB and copper MFEC were performed at different wall temperatures, each for 1 day as shown in Table II.2. For the same conversion of the FTS, the reaction heat was the same, but the temperature difference from centerline to reactor wall was much lower for Cu MFEC. When the conversion increased with higher wall temperature, more reaction heat was produced inside the catalyst bed, which made the temperature difference rise again. For PB, the temperature difference increased faster than that of copper MFEC. That increase was 70.2˚C at 255˚C wall temperature for this 15mm ID reactor and a runaway state was already reached where the methanation reactions dominated (Figure II.12). Because of the poor heat transfer characteristics of PB and the relatively higher temperature inside the catalyst bed, the reaction rate (cobalt-time-yield) was higher for PB than that for Cu MFEC at the same wall temperature (from day 1 to day 4). The runaway state of PB caused a quick deactivation of the catalyst and the reaction rate declined to 1/3 from day 2 to day 5. This was probably because of the high temperature sintering or carbon deposition during runaway on day 4. The application of copper MFEC avoided runaways at high temperature and an even temperature profile was maintained inside the catalyst bed and with little deactivation. Copper MFEC provided a larger range of operating temperatures and better temperature control without damaging the catalyst and decreasing the amount of product.

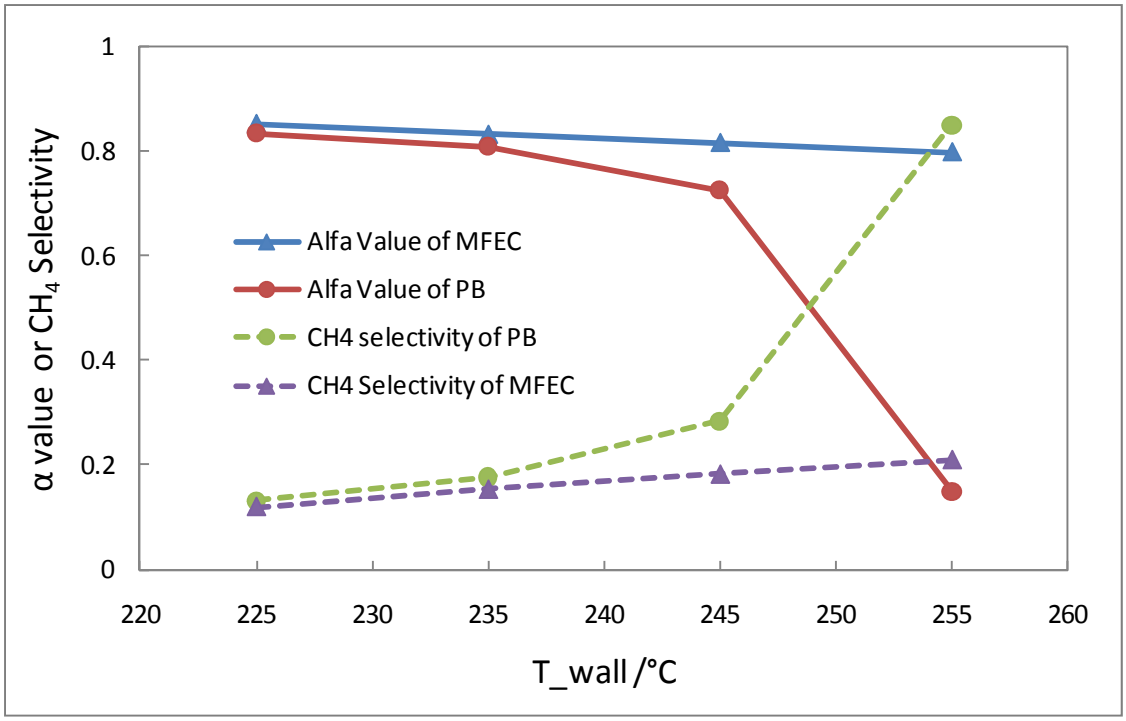

Figure II-12. The chain growth probability factor vs. reactor wall temperature for PB and Cu MFEC

The chain growth probability factor (α) of FTS is dependent on the catalyst temperature. Because of the higher effective thermal conductivity of copper MFEC, the intra-bed heat transfer was enhanced and a more uniform temperature profile inside the catalyst was achieved. The α value also was improved by MFEC structure as shown in Figure II.12. The higher thermal conductivity in the copper MFEC bed resulted in a smaller temperature difference so that the local catalyst temperature was lower than that in PB. The improvement of the α value was observed for high wall temperatures or for large diameter reactors that always have high centerline temperature in PB. Therefore, the application of copper MFEC gave a

higher α value and the desired selectivity of heavier products such as C_{5+}. Although copper was used as a catalyst for methanol synthesis, the surface area of the copper fiber was only 0.7% of the total surface area of alumina. Methanol synthesis was negligible in MFEC with Co/Al_2O_3 since FTS product analysis where the water phase contained only 15ppm methanol.

II.5 Conclusions

The enhanced heat transfer characteristics of Cu, Ni, and stainless steel MFEC were studied by experimental determination of thermal parameters and compared with those of PBs made of copper or alumina or mixtures of the two. In stagnant N2 gas tests, the radial effective thermal conductivity of copper MFEC (9.05W/m-K)was increased 56-fold relative to that of alumina PB, while the inside wall heat transfer coefficient (235W/m2-K)was increased 10-fold relative to that of alumina PB. The high thermal conductivity of MFECs in stagnant gas may have resulted from the sinter-locked network formed by the metal fibers in the MFEC structure that provided continuous metal channels or bridges for heat conduction. With gas passing through the tested materials, the MFEC structure offered a higher volumetric geometric surface area for the convective contribution of heat transfer than the structure of PB, which further increased the effective thermal conductivity of MFEC.

In the FTS tests, the pre-manufactured FTS catalyst particles were entrapped into sintered Cu fiber matrices to form a Cu MFEC structure. This demonstrated an enhanced intra-bed heat transfer property, which resulted in a much more uniform temperature profile through the catalyst bed. The application of Cu MFEC in FTS effectively prevented hot spots and runaway at high temperature, maintained a higher reaction activity, and higher selectivity of

heavy products. Furthermore, intra-particle mass transfer was enhanced because of the presence of small particles in this material as compared with those in typical extrudates used in industrial fixed bed reactors. Therefore, Cu MFEC offered a larger operating temperature range and better product selectivity.

Acknowledgments:

This work was supported by the U.S. Navy under a U.S. Navy contract at Auburn University (N00014-09-C-0208) administered through the Office of Naval Research. The authors wish to thank IntraMicron (Auburn AL., US) for technical support.

Chapter III: Effective Thermal Conductivity and Junction Factor for Sintered Microfibrous Materials

Min Sheng, Donald R. Cahela, Hongyun Yang[1], William R. Yantz Jr., Carlos F. Gonzalez, Daniel K. Harris[2], Bruce J. Tatarchuk

Department of Chemical Engineering, Auburn University, Auburn, AL 36849, USA
[1] IntraMicron Inc., 368 Industry Dr., Auburn, AL 36832, USA
[2] Department of Mechanical Engineering, Auburn University, Auburn, AL 36849, USA

Abstract

A modified resistance network model, the junction factor model, is developed to predict the effective thermal conductivity of sintered microfibrous materials (MFM) made of conductive metals. It contains two characteristic variables: metal volume fraction (y) and junction factor (∅). The junction factor representing the fibers' connection quality can be easily determined by the measurement of electrical resistance, so this model provides a practical and convenient method to estimate the effective thermal conductivity of sintered MFM. Moreover, various methods to improve the junction factor and the effective thermal conductivity of copper MFM are investigated. High sintering temperatures and long sintering times increase both the junction factor and effective thermal conductivity of MFM. Electroplating and impregnation methods were also employed to enhance the junction conductivity. Electroplating provides a significant improvement in the junction factor and the effective thermal conductivity of the media.

Keywords: Effective thermal conductivity, Heat Transfer, Microfibrous Materials, Resistance network modeling, Junction factor

III.1 Introduction

Microfibrous materials (MFM) are a micro-structured media made of sintered micron-diameter metal, glass or polymer fibers with high voidage [83-86]. It has also been found that MFM entrapped with catalyst particles (Microfibrous Entrapped Catalyst, or MFEC) provides high void volume, uniform particle distribution, and reduced pressure drop compared to packed beds of similar size particles. Intraparticle mass and heat transfer are enhanced due to the presence of small particulates in these materials (e.g., 10 to 100μm dia.) versus larger catalyst extrudates typically used in industrial fixed bed reactors (e.g., 1 to 3 mm dia.). MFEC made of highly conductive metal fibers could also improve intra-bed heat transfer efficiency in fixed bed reactors for highly exothermic or endothermic reactions, compared with traditional packed beds (PB). Using small particles entrapped in fiber matrices also results in high contacting efficiency [87,88]. Several investigations have been carried out to understand the function of the media. Kalluri et al. [89] studied the effects of microfibrous media on mitigating bed channeling, while Yang et al. [90] and Duggirala et al. [91] investigated the effects of microfibers on external mass transfer in desulfurization reactors by both experimental approaches and CFD simulations. Still other investigations have demonstrated the benefits of MFM's enhanced heat transfer capabilities on nitration of benzene [109] and methanol steam reforming [110].

Recently, the thermal parameters of metal MFEC were estimated by measuring the temperature profiles developed in steady-state and transient heat transfer experiments and fitting these data with Euler explicit/implicit methods [111]. In a stagnant N_2 gas, the radial

effective thermal conductivity of Cu MFEC was 56-fold greater than that of an alumina packed bed (PB), while the inside wall heat transfer coefficient was approximately 10 times that of alumina PB. Even compared with a PB made of pure copper particles, the Cu MFEC provided significantly higher effective thermal conductivities and higher inside wall heat transfer coefficients in both stagnant and flowing gas. Despite the promising attributes of MFEC, no priori model exists to predict the effective thermal conductivity of MFEC or MFM. In Tang's work [110], a volume-averaged combination of the interstitial thermal conductivities of the solid matrix and the fluid was used to estimate the effective thermal conductivity of a metallic media. This model assumes a perfect connection between the fibers. Due to this assumption, the model overestimates the effective thermal conductivity of MFEC-like structures. Effective thermal conductivities of MFEC from experimental determinations are much lower than the prediction by this model [110], which suggests that the effective thermal conductivity is highly dependent on the geometrical structure of the fibers in MFECs. The sinter-locked network of fibers is believed to be the predominant back bone contribution to the MFEC's high thermal conductivity and requires an accurate foundation with respect to the physical properties of the fibers, as well as their orientation and degree of sinter bonding.

In this paper, a model with a characteristic variable to represent the connection quality of sintered fibers was established in order to accurately estimate the effective thermal conductivity of MFM and guide efforts to optimize and tailor its formation procedures. Moreover, various methods, such as sintering temperature, sintering time, electroplating and an impregnation method, were investigated in an attempt to incease the thermal conductivity of MFM.

III.2 Materials and Methods:

III.2.1 Sample Preparation

A wet-lay paper-making method was used to prepare MFEC which utilized traditional paper-making equipment and techniques [83-86]. Micron-sized metal fibers (IntraMicron, Inc. Auburn, AL, USA) were slurried in an aqueous suspension with silica or alumina particulates as catalyst support and cellulose fibers as binder in the preform. The resulting mixture was then cast into a preformed sheet using a wet-lay process and dried at 110°C for 3 hours to create a self-supporting sheet. Subsequently, the preform underwent a pre-oxidation in flowing air at 500°C for 30 minutes to remove the bulk of the cellulose. Subsequently the perform was sintered in a flowing gas containing H_2 at an elevated temperature (ca. 700°C for copper fibers) for 45 to 60 minutes to form a sinter-locked network that entrapped the selected support particulates.

Recently, newer methods to manufacture MFEC have been developed by preparing sintered fiber networks in a preliminary step followed by subsequent entrapment of catalyst particles into it. With this method, the catalysts are free of contaminates or potential thermal degradation which can occur during the preparation and high temperature sintering steps. This approach also provides other advantages, including the potential to fully optimize the thermal characteristics of the structure prior to catalyst addition. Examples of such treatments include electroplating and copper impregnation which can improve conductivity but which might otherwise poison catalyst surfaces.

In order to investigate the effect of sintering conditions, MFM samples made of 12μm diameter and 3mm length copper fibers were sintered at 550°C, 650°C, 700°C and 750°C for 50 minutes and their thermal conductivity and electrical resistances were measured. Also, different sintering times were investigated at the 550°C sintering temperature.

III.2.2 Thermal Conductivity Determination

The copper-only MFM samples were cut into disks with a diameter 6% larger than the tube ID (36.5mm) and then stacked in the middle section of a copper tube (38.1mm OD, Figure III.1). The loading pressure was kept between 10kPa to 20kPa, which maintained the high porosity in these materials. The length of the bed was 152.4mm, so that the effect of axial heat flow at the midplane could be eliminated because the bed is of adequate length. Fine thermocouples (Omega, 1/32 inch in diameter, 0.79mm) were utilized to measure the temperature profiles of the tested materials. The volume of hot water in the water bath was large enough to provide a high thermal mass and keep the temperature reduction within 1°C after the packed tube was immersed in the bath. The thermal conductivities of the samples were determined by measuring the heating curve in a transient test [94]. In this transient test, the tube was filled with stagnant N_2 at ambient pressure. At t=0, the test apparatus was dipped into a stirred water bath of constant temperature and the transient temperature was recorded in the media as it approached the temperature of the water bath. The temperature-time profile at the center on the midplane was recorded by a data logger (Omega, OM-DAQPRO-5300), as shown in Figure II.2. The Euler implicit method and Newton-Raphson search algorithms were used to extract the effective thermal conductivity from the temperature-time profiles.

III.2.3 Electrical Resistance Measurement

The electrical resistance of Cu MFM was also measured to determine the junction factor which is the parameter representing the connection quality between fibers (to be discussed and developed later). The same Cu MFM samples used in the thermal conductivity measurements were cut into 24x200mm strips. The electrical resistances of these MFM strips were measured based on different lengths, then the electrical resistance per unit length was obtained by linear regression. To ensure uniform contact resistance, constant pressure (31.7kPa) was applied to both ends of the measured length. A EG&G PARC Potentiostat/Galvanostat Model273A co-operated with a Lock-in Amplifier Model 5210 was used in this measurement, which gave an accurate measurement of electrical resistance down to $10^{-5}\Omega$. The electrical resistance measurement was used to determine the junction factor so that the junction model could be used, in part, to calculate the effective thermal conductivity of the packed tubes.

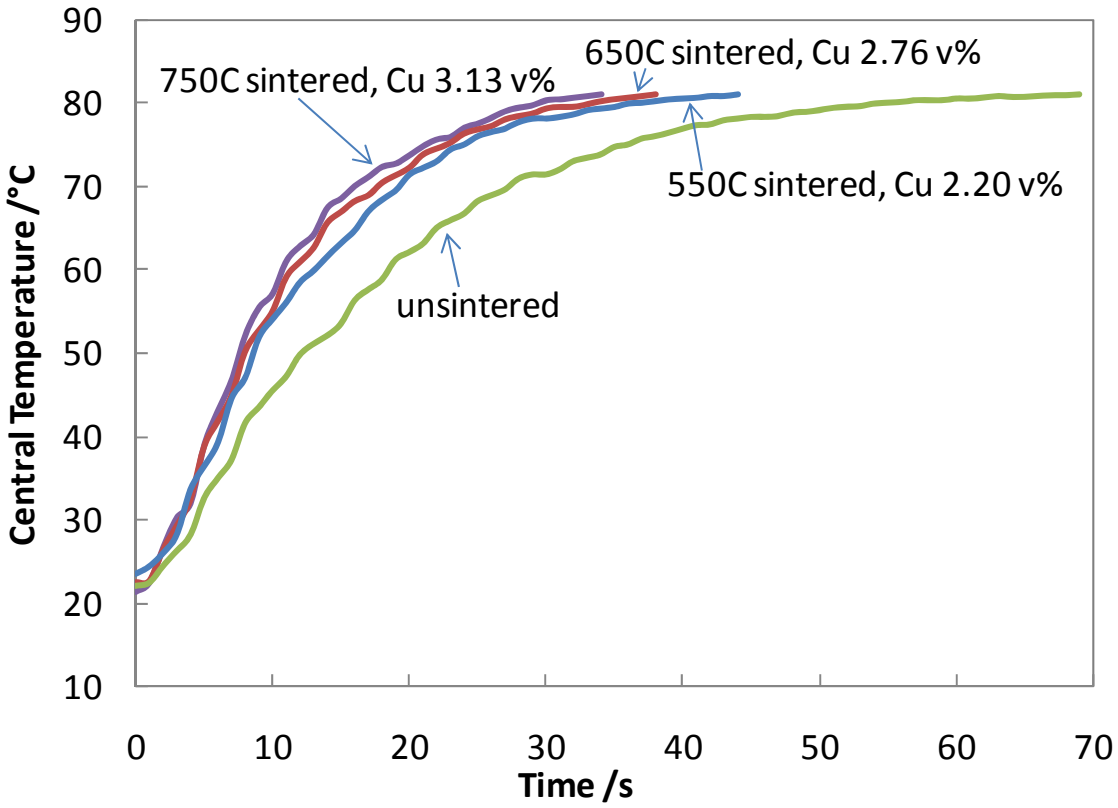

Figure III-1. Temperature-time profiles at the center of the middle plane for Cu MFM sintered at different temperatures.

III.2.4 Copper Electroplating

Electroplating MFM was expected to deposit a uniform layer of metal onto the surface of the structure's fibers, thus physically increasing the diameter of the fibers and improving their connection quality. Cu MFM were prepared by sintering at 550°C in H_2 for 50min, which removed most surface contamination and provided a clean fiber surface for electroplating. The structure was electroplated in an aqueous solution of 0.75M $Cu(NO_3)_2$ and 0.60M H_2SO_4. The electric current was set at a constant 1A for all the plating, which corresponds to 1.6 to 2.3mA/cm^2 for 12 to 19μm fiber diameters. After electroplating, the Cu MFM samples were

washed with D.I. water and subsequently with acetone. Copper was electroplated for different periods of time, as listed in Table III.1. The sample mass after the treatment and the percent of mass increase due to copper deposition are also listed. The average diameter was calculated by assuming an ideal cylinder shape for the fibers. After copper electroplating, samples were subsequently annealed at 750°C for 1hour in nitrogen with 5% hydrogen.

Table III.1 MFM samples electroplated at 1A current for different periods of time

Time of Plating /hr	Sample mass /g	Mass increase %	Average Diameter /μm
Original	1.19	0	12
0.5	1.80	50.6	14.7
1	2.36	97.6	16.9
1.5	2.95	147.3	18.9

III.2.5 Copper Impregnation Method

MFM were impregnated by dipping in a solution of metal salt and subsequent drying at 110°C overnight and reduction at a suitable condition. In this study, Cu MFM sintered at 550°C for 50min were impregnated by an 1.84M $Cu(NO_3)_2$ aqueous solution, and reduced at 400°C for 1 hour in flowing hydrogen. Because of the potential corrosion of copper when exposed to water and air, the drying treatment was integrated into the reduction treatment, so that the water in the impregnated MFM was quickly evaporated during the reduction step. Sintered MFM samples with the same original mass were impregnated and reduced for different times. The sample masses after the treatments and the mass increase due to copper deposition are displayed in Table III.2.

Table III.2 MFM samples modified by impregnation method with different solution volumes

Solution volume /cc	Sample mass /g	Mass increase %
original	1.31	0
4.5	1.80	37.5
9	2.30	75.9
13.5	2.79	113.4

III.3 Results

III.3.1 Model with Junction Factor

As discussed previously [111], the improvement of the MFEC's thermal conductivity is due to the sinter-locked network of metal fibers in its structure. This type of structure benefits from the aspect ratio and continuity of the metal fibers and sintered bridges for heat conduction and is much more effective than the point contacts found in powdered packed beds.

Currently there exists no model to predict the thermal conductivity of MFM that takes the geometrical arrangement of the sintered filters into consideration. Some theoretical and empirical models have been proposed to predict the thermal conductivity of fibrous materials with stagnant gas or low gas flowrates, including a series model [112], a parallel model [112], Dul'new's model [113] and Mantle's model [114]. The series model and parallel model represent the lower and upper limits for the conductivity of composite materials, respectively. Dul'new's model assumed that the fibers are infinitely long cylinders and the model parameters were regressed from unsintered fibrous materials. The effective thermal conductivity of sintered MFM cannot be fitted well by Dul'new's equation because in MFM materials the unsintered fiber length (3mm) is too small to meet the assumption of infinite fiber length.

Mantle derived an empirical equation that compensates for the effects of porosity and the aspect ratio of sintered metal fiber structures, but it was observed that the connection quality between fibers is much more crucial to the thermal conductivity of MFM with fibers having an aspect ratio of $(L/D) > 50$. Therefore, a model that considers the connection quality between fibers is required and may offer a good correlation between predictions and experimental data. Such a model would also provides a sound design basics for the fabrication of enhanced materials.

The resistance network model of packed beds [71], which breaks the thermal conductivity into a series/parallel combination of the individual resistances of the conduction paths, was modified for use in this study, as illustrated in Figure III.2. The overall thermal resistance for a particle packed bed is given by:

$$R = \left[\frac{1}{(1/R_{solid}+1/R_{gas})^{-1}+R_S} + \frac{1}{R_G}\right]^{-1} \quad \text{(III-1)}$$

The thermal resistance can be determined as following.

$$R = \frac{L}{k \cdot A} \quad \text{(III-2)}$$

For example, for a packed bed made of pure copper powder, the effective thermal conductivity in stagnant nitrogen was measured to be 0.23W/m-K [111]. Knowing $k_{Cu} = 398$W/m-K and $k_{N2} = 0.0258$W/m-K, and assuming $L = 1$m and $A = 1\text{m}^2$, Eq.III-2 gives $R_S = 0.0025$K/W and $R_G = 38.76$ K/W. The resistances of point-contacts and gas in the micro-gap, $(1/R_{solid} + 1/R_{gas})^{-1}$, is determined to be 4.895K/W. For most applications

involving packed beds with low gas velocity in chemical processes, R_G is high because gases always possess a relatively low thermal conductivity. Due to low R_S, $(1/R_{solid} + 1/R_{gas})^{-1}$ is the key term to determine the overall thermal resistance. More details of thermal analysis procedures can be found in the literature [115,116].

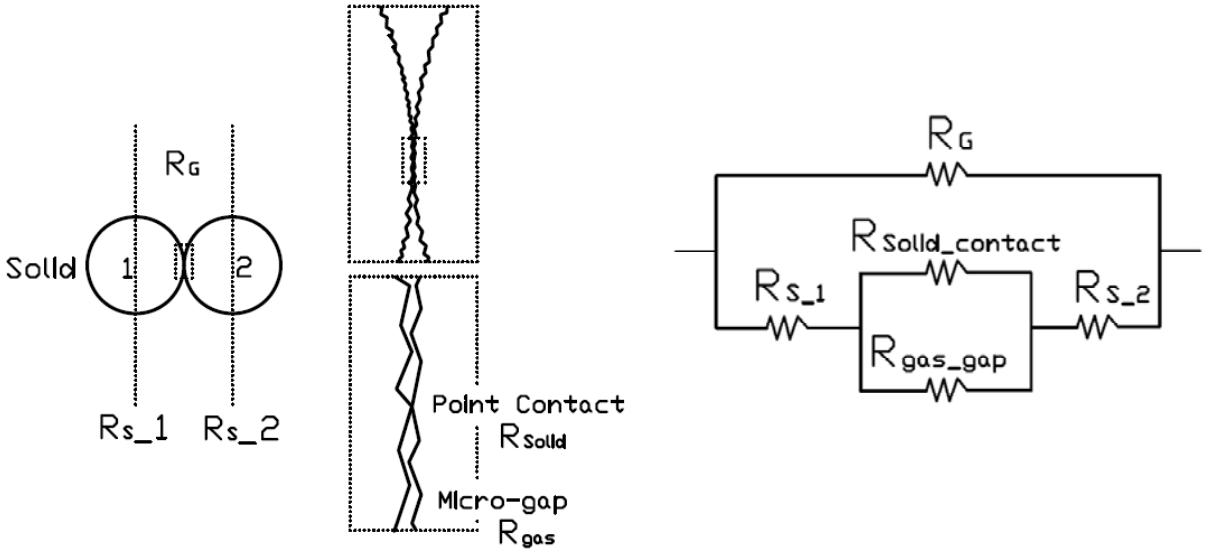

Figure III-2. Sketch of the physical model and the resistance network model of PB. R_G: the thermal resistance of bulk gas; R_S: the interstitial thermal resistance of solid particles; R_{solid}: the contact resistance between particles; R_{gas}: the resistance of gas in the micro-gap between two particles.

For MFM with entrapped particles, another parallel conduction path is needed to represent the sintered metal fibers which provide a continuous metal channel in the sinter-locked network (see Figure III.3). Taking this path into account, the overall thermal resistance for MFM can be derived by:

$$R = \left[\frac{1}{(1/R_{solid}+1/R_{gas})^{-1}+R_S} + \frac{1}{R_G} + \frac{1}{R_F+R_{F\_jun}}\right]^{-1} \quad \text{(III-3)}$$

where R_S is the average interstitial thermal resistance from solid particles and metal fibers.

In the case of a stagnant gas or low gas velocity, the thermal conductivity of the gas is much lower than that of the metal; the thermal conductivities of the solid point-contacts and the gas in the micro-gaps are also low. Therefore, $1/R_G$ and $(1/R_{solid} + 1/R_{gas})$ are relatively small, so Eq.III-3 can be reduced to:

$$R = R_F + R_{F\_jun} \quad \text{(III-4)}$$

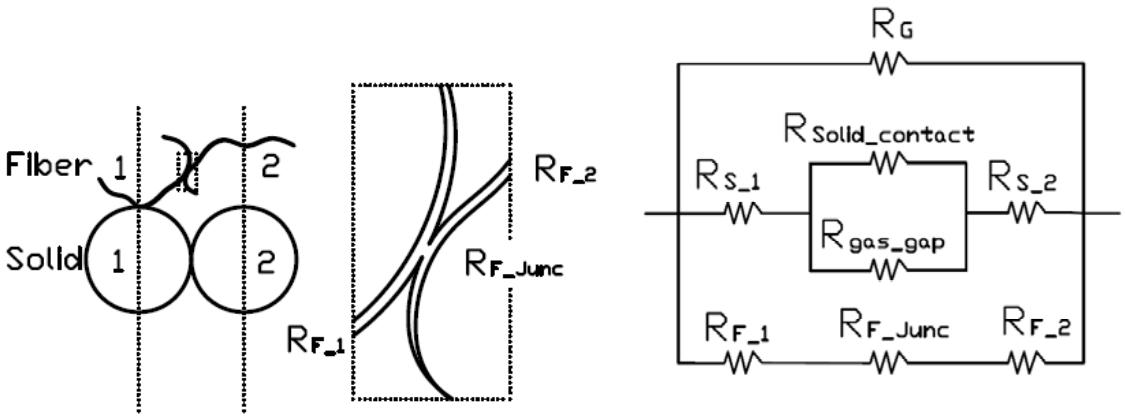

Figure III-3. Sketch of the physical model and the resistance network model of the MFEC. R_F: the interstitial thermal resistance of the metal fibers; R_{F_jun}: the interstitial thermal resistance through the junction between two connected fibers

Overall resistance therefore primarily depends on the conduction path through the continuous metal channels. By assuming $R = R_F/\emptyset$, then R_{F_jun} is equal to $(1-\emptyset)R_F/\emptyset$, where $\emptyset$ is the junction factor representing the connection quality between fibers in the MFM. The junction factor can be determined by measuring the electrical resistance. Therefore, the effective thermal conductivity of MFM is given by:

$$k_e = y_m \cdot \emptyset \cdot k_m \quad 0 \le \emptyset \le 1 \tag{III-5}$$

Based on the resistances of point-contacts and gas in the micro-gaps of packed beds, this simplification gives a reasonable prediction (within a 10% deviation for MFEC) when the interstitial thermal conductivity of fibers ($y_m \cdot \emptyset \cdot k_m$) is greater than 2W/m-K, or for MFM when $y_m \cdot \emptyset \cdot k_m > 10 \cdot R_G$. Due to this restriction, this model should be a good prediction for the radial effective thermal conductivity of MFM discs made of highly conductive metals, such as copper and nickel. If the metals are not highly conductive, the deviation introduced by this simplification is unacceptable. For example, the junction factor of stainless steel (S.S.) MFM was estimated to be 1.51, which is greater than 1. This discrepancy results from the low interstitial thermal conductivity of S.S. fibers which is of the same magnitude as some of the other heat transfer terms. Furthermore, this model is restricted to MFM with stagnant gas or low gas velocity, where the convective heat transfer can be neglected. For high gas velocities, it is believed that the effective thermal conductivity of MFM is the result of the co-enhanced interaction of the metal channels' high conductivity and the high convective contribution from the fibers' high geometric surface areas. Meanwhile, the axial thermal conductivity of MFM is small because of the deliberate preferential alignment of the fibers in the radial direction from

the wet-lay and subsequent packing procedures. Therefore, this model cannot be used to calculate the axial thermal conductivity. For many practical applications where heat is removed from the outer wall of a tubular reactor the model is well-suited.

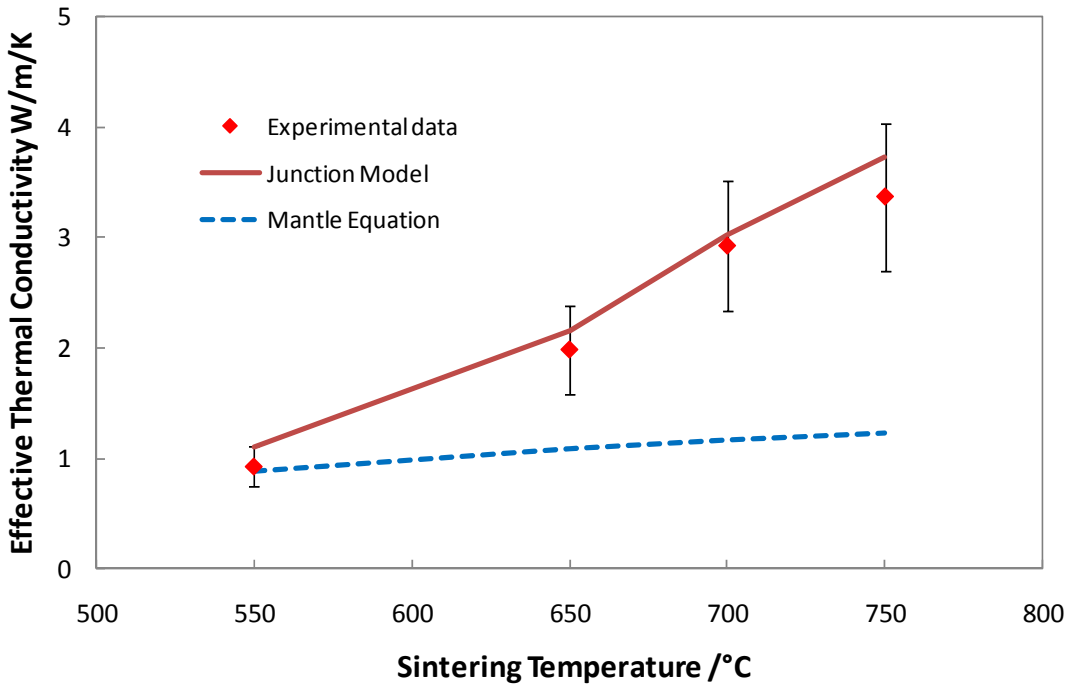

Figure III-4. Effective thermal conductivity of Cu MFM sintered at different temperature for 50min, and the predictions by the junction model and Mantle equation.

Figure III.4, for the Cu MFM sintered at different temperatures, shows a comparison between the effective thermal conductivities predicted by the junction model of this study and the Mantle equation. The junction model agreed well with the experimental data derived from the materials sintered at different temperatures because it takes into account the differing sintering temperatures on the connection quality between the fibers. In contrast, the Mantle

model only addresses the effects of porosity and the aspect ratio of the fibers. Because copper fibers with the same length and the same diameter were used in all samples, the Mantle equation only addresses the porosity changes, which is the result of a modest shrinking of MFM during the sintering process. Because Mantle's equation has not taken into consideration the connection quality among fibers, it underestimates the effective thermal conductivity of MFM sintered at higher temperatures.

III.3.2 Junction Factor

The radial effective thermal conductivity of MFM made of highly conductive metals in stagnant gas or low *Re* can be estimated by Eq.III-5. Here, all parameters are easy to determine except the junction factor. The junction factor is used to represent the connection quality among fibers in MFM. An assumption for this parameter is exhibited in Figure III.5. Here, the heat flux or electrical current through the physical structure of the metal fibrous material was conceptually idealized as a straight metal cylinder with a junction. The length of the junction is infinitely small, and the total volume of the bulk cylinder is equal to the total volume of the metal in the fibrous material. The crossing area of the junction corresponds to the effective crossing area at the sintered junctions in MFM, as shown in Figure.III.10.a. In this assumption, the junction can be expressed as:

$$\emptyset = \frac{Crossing\ Area\ of\ Junction}{Crossing\ Area\ of\ Bulk\ Metal} \tag{III-6}$$

From this point of view, the junction factor will depend on many variables. First, the orientation of the fibers will constitute an upper limit on the junction factor. Because the conduction between fibers and gas is relatively small and thereby ignored, some fibers which

are not along the direction of heat flux will either partially contribute to the heat transfer behavior or not contribute at all. For example, as shown in Figure III.5, the fiber perpendicular to the direction of the heat flux cannot transfer the energy from one end to the other end, but it contributes to the total volume of the metal in MFM, thus increasing the crossing area of the bulk metal. Therefore, the orientation of the fibers imposes an upper limit for the junction factor. In addition, the junction factor directly represents the connection quality among fibers, which strongly depends on material, sintering temperature, sintering time, fiber diameter and other factors. A high sintering temperature and longer sintering time give better fused connections at the junctions. As shown in Figure III.6, the junction factor increases with the sintering temperature for Cu MFM. A smaller fiber diameter means lower temperatures are needed for making the appropriate contacts due to the high surface free energy and propensity for sintering possessed by unsaturated metal surfaces.

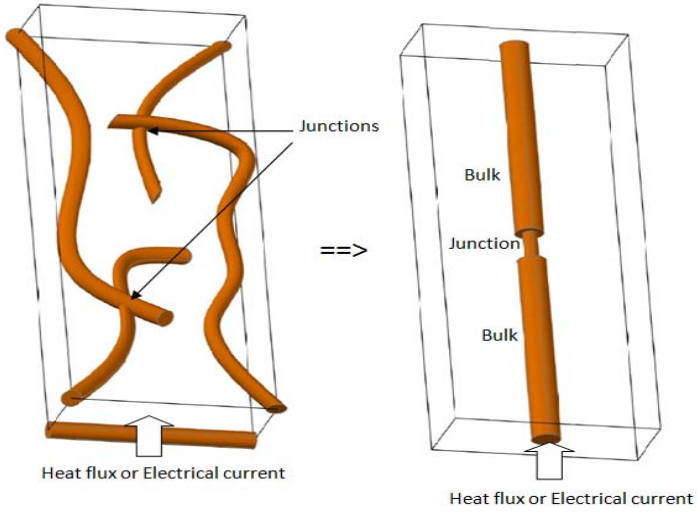

Figure III-5. Idealized model of the junction factor for MFM materials

The correlation between thermal conductivity and electrical conductivity was studied by Powell [117] on solid materials. Koh et al. [118] fit the data of sintered metal powders with a linear relationship. Their empirical equation for sintered copper powder can be represented by the following equation independent of porosity:

$$k = 2.307 \times 10^{-8} \frac{T}{R^*} + 18.6 \quad \text{(III-7)}$$

The sintered MFMs have the same attributes as sintered metal powders for heat flux and electrical current through them, conducted by the bulk metal and limited by the connection between fibers. Therefore, electrical resistance is used to quantitatively characterize the fibers' connection quality in MFM. The effective crossing area at the junction can be calculated from measured electrical resistivity as in Eq.III-8, and the total crossing area can be determined from the weight of sample. By combining them, the junction factor can be obtained, as given in Eq.III-9.

$$A_e = \frac{\varphi L}{R^*} \quad \text{(III-8)}$$

$$\emptyset = \frac{\varphi \rho L^2}{W R^*} \quad \text{(III-9)}$$

For the Cu MFMs sintered at different temperatures, the electrical resistances were measured and the junction factors were calculated based on Eq.III-9. A comparison of these junction factors with junction factors determined by Eq.III-5 is illustrated in Figure III.6. Strong correlations between them confirmed the feasibility of determining the junction factor from electrical resistance, and thus the prediction of thermal conductivity from this factor. This

method gives an efficient way to determine the effective thermal conductivity of MFM since the measurement and analysis of thermal conductivity is more complicated than measuring electrical resistance. This method requires that the interstitial thermal conductivity of fibers is high enough to dominate the overall thermal conductivity of MFM. This requires that the MFM is made of a highly conductive metal and that a good connection quality between fibers exists. For example, the junction factor for unsintered MFM is 0.078 based on a measurement of thermal conductivity, but 5.8E-11 based on a measurement of electrical resistance. In this case, the unsintered fibers give an extremely high electrical resistance, but they show a thermal conductivity as high as a packed bed, so that the proposed model does not work in this case.

As shown in Figure III.7, the loading pressure on an un-sintered preform of Cu MFM increases the junction factor due to the increase of point contacts between fibers. However, the cross-sectional or crossing area of these point contacts is much smaller than that of sintered bonds, so that even at pressure as high as 50kPa a junction factor of only 0.01 was observed. This contribution to the junction factor is relatively small and thereby ignored in most cases. Thus the electrical measurements for the junction factor are typically carried out on MFM without any extension loading pressure.

III.3.3 Methods to improve the effective thermal conductivity of MFM

MFM with high effective thermal conductivity can be used in applications involving highly exothermic and high endothermic reactions/processes in terms of thermal stability, product selectivity and catalyst activity. Because higher effective thermal conductivity

improves the uniformity of the steady-state temperature profile developed inside the catalyst bed, methods to improve the effective thermal conductivity of MFM are desirable.

III.3.3.1 Sintering Temperature

Increasing sintering temperature is one method to improve the fibers' connection quality, and thus increase the effective thermal conductivity, as shown in Figure III.6. In general, the sintering temperature is set between 50% to 85% of the corresponding bulk metal melting point. In this temperature range, the metal atoms on the surface of the fibers touching each other sinter bond by reducing their surface free energy and surface area.

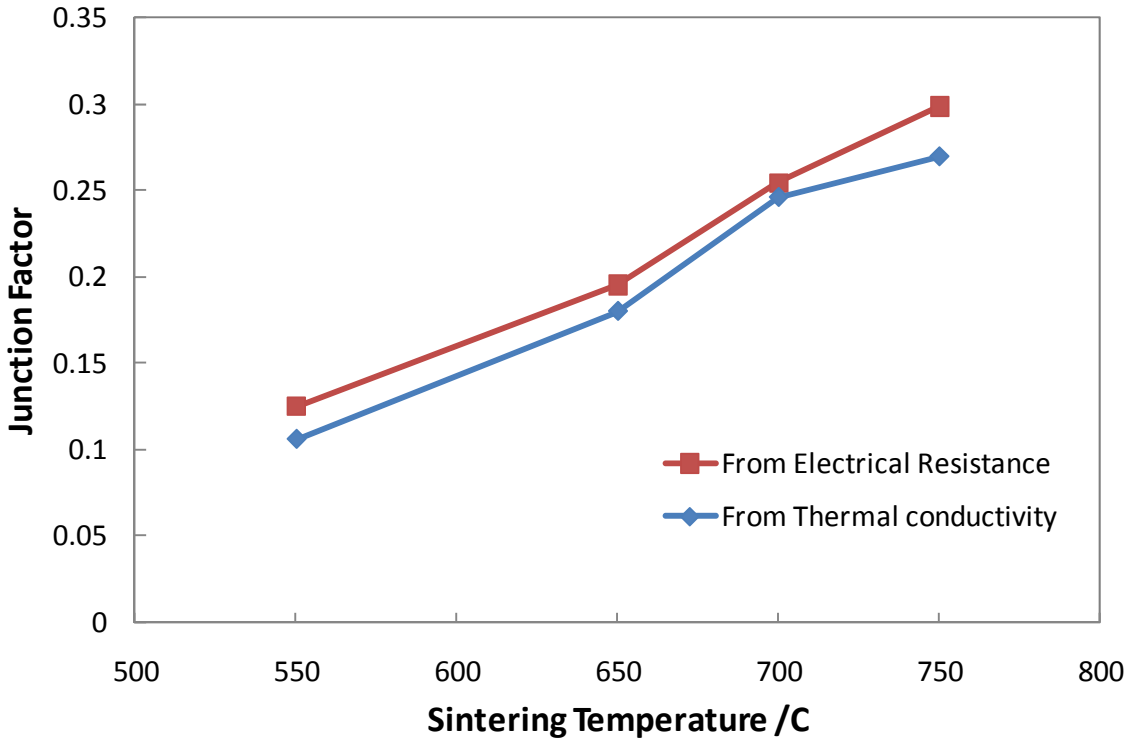

Figure III-6. Junction factor for Cu MFM sintered at different temperatures for 50min

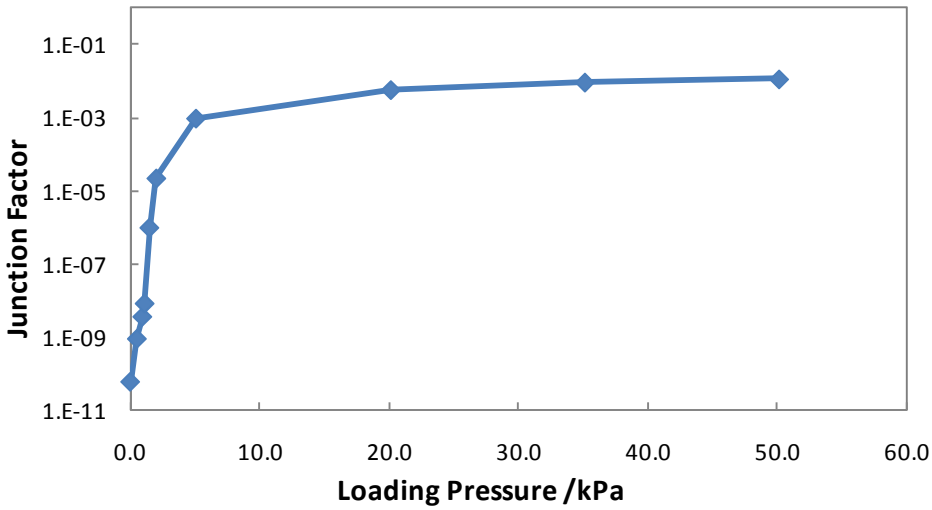

Figure III-7. Junction factor of un-sintered Cu MFM under different loading pressures from the electrical measurements

Increasing the sintering temperature is the most efficient method to increase the effective thermal conductivity of MFM, but it also reduces of the voidage in MFM due to a modest level of shrinkage of the metal fiber materials during high-temperature sintering and subsequent cooling. For example, the copper volume percentage of MFM increases from 2.2% to 3.13% when sintered from 550°C to 750°C, respectively, which corresponds to a decrease in porosity from 97.8% to 96.87%.

III.3.3.2 Sintering Time

Increasing the time can also increase the effective thermal conductivity, as shown in Figure III.10. Similar to the benefits given by higher sintering temperature, longer sintering times also enable the production larger bridges between fibers. It was found that the gains in thermal conductivity are dramatic during the first 1 hour of sintering at 550°C while additional

sintering time only marginally increases the thermal conductivity. Therefore, the ideal time for sintering MFM is usually around 45~60min. The explanation for this is that the touching points between fibers which are easiest to be sintered are consumed during the first hour of sintering.

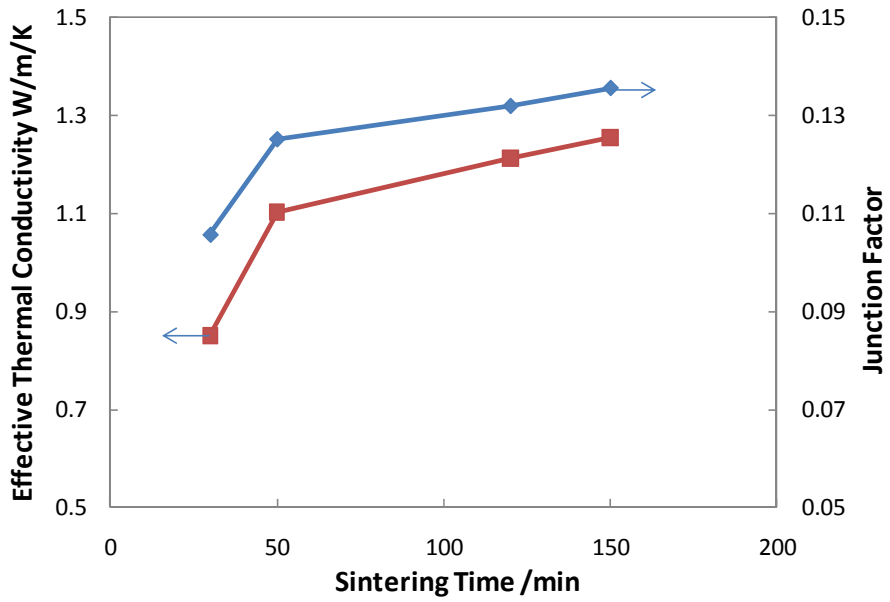

Figure III-8. Junction factor and effective thermal conductivity of Cu MFM sintering at 550C for different time

III.3.3.3 Electroplating

Electroplating can deposit additional copper on the outside of the fibers and is therefore expected to improve the fibers' connection quality, as well as the thermal conductivity of MFM. Because the catalyst entrapped in MFM is generally sensitive to additional treatment, electroplating is suggested to be applied to post-sintered MFM prepared without catalyst or

catalyst support. After electroplating, the catalyst particles can be entrapped into the MFM to form MFEC.

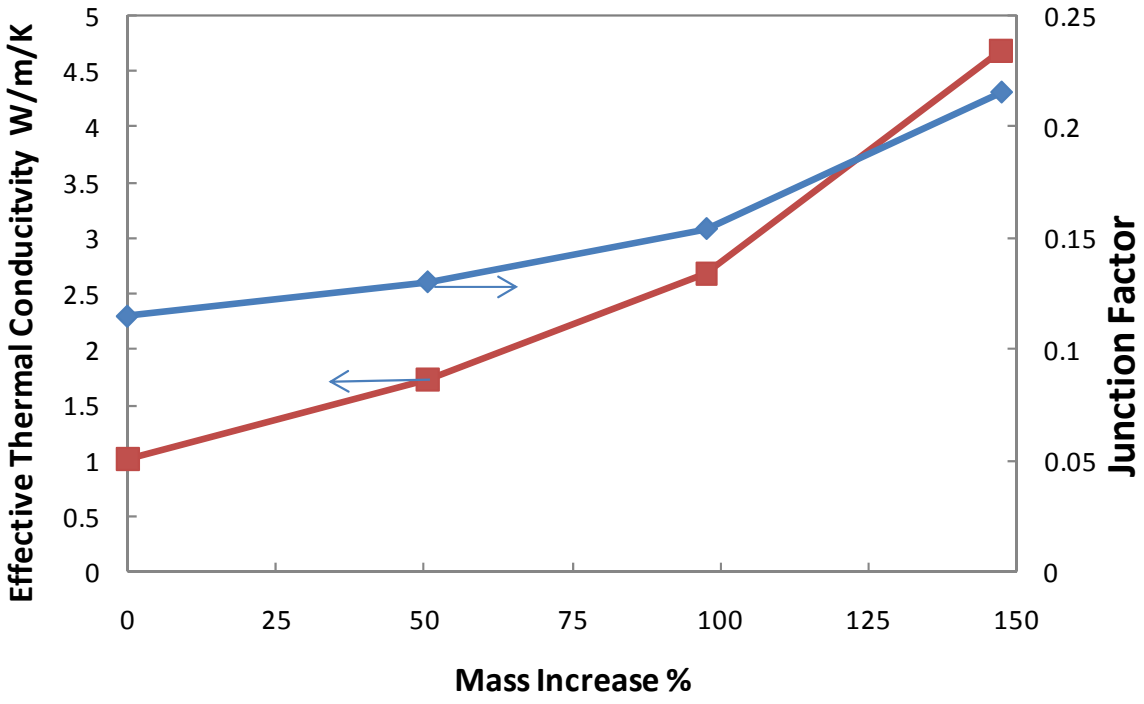

Figure III-9. Junction factor and effective thermal conductivity of Cu MFM modified by electroplating

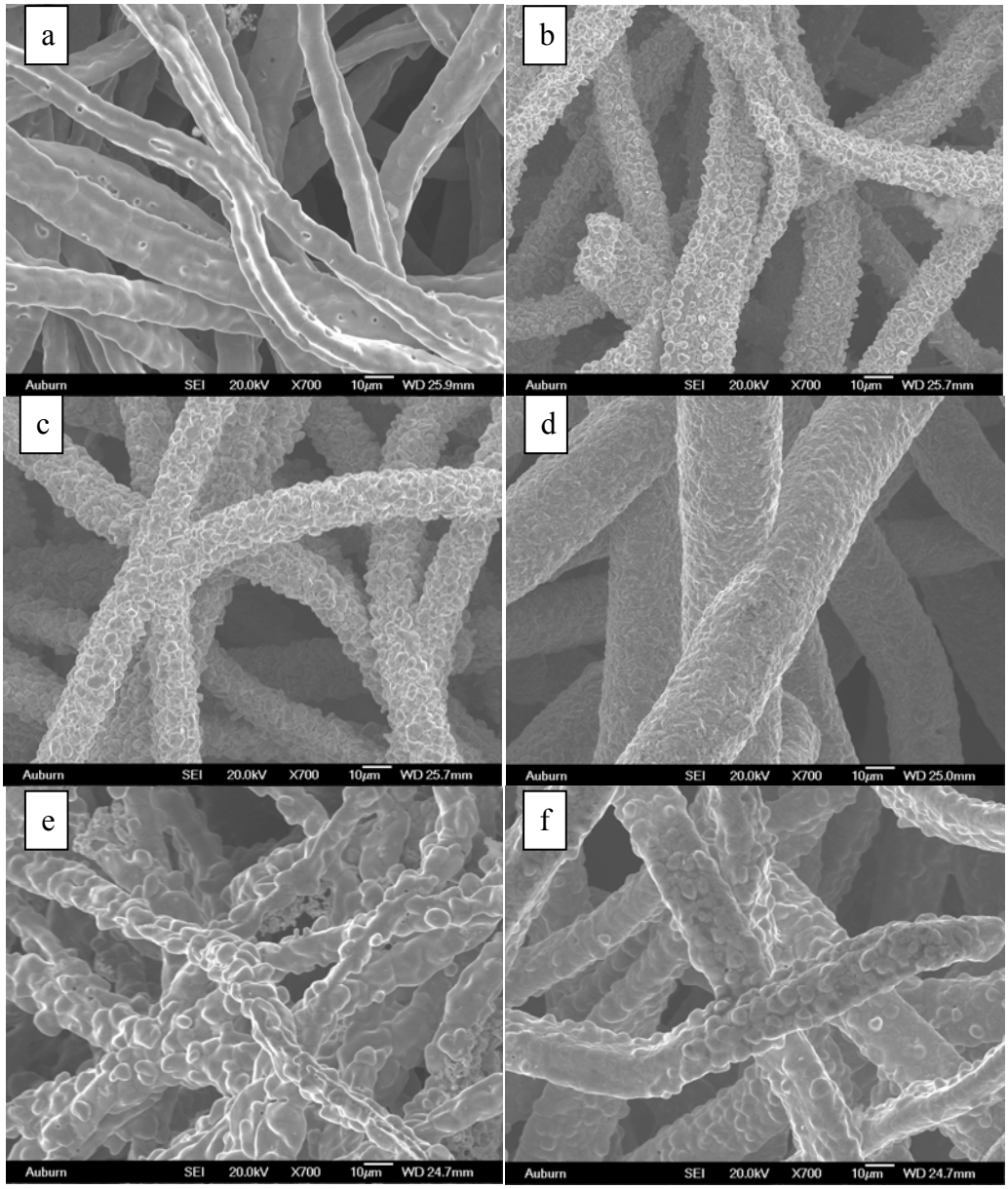

Figure III-10 SEM of Cu MFM modified by electroplating; a) original Cu MFM after 550°C sintering, 12µm fiber; b) electroplating for 0.5hr, mass increasing 50.6%, 14.7µm fiber; c) electroplating for 1hr, mass increasing 97.6%, 16.9µm fiber; d) electroplating for 1.5hr, mass increasing 147.3%, 18.9µm fiber; e) sample c after annealing at 750°C for 1 hour; f) sample d after annealing at 750°C for 1 hour

For the MFM sintered at 550°C for 50min, different amounts of copper were added via electroplating, and the junction factors were determined by electrical resistance measurements as shown in Figure III.9. The effective thermal conductivities were calculated based on the junction model of Eq.III-5. It is observed that the electroplating not only increases the metal volume percentage in MFM, but also improves the fibers' connection quality. The SEM images in Figure III.10 show the geometric surface of the fibers during the electroplating process. The copper crystals grow up from small seeds on the smooth surface of the original fibers during electroplating. After a period of time, the crystals on the surface are connected to one another. The connection quality of the junctions between fibers is improved by the additional copper; therefore, the effective thermal conductivity increases with the amount of electroplated copper.

Subsequent annealing of the electroplated MFM samples at 750°C for 1hour provided for the improvements in the junction factor and the effective thermal conductivity (Figure III.9). This high temperature treatment increased the junction factor of the un-electroplated MFM from 0.115 to 0.315, and that of 147.3% copper electroplated MFM from 0.215 to 0.462. The source of this increase is the sintering and coalescence of the small copper crystallite that were formed via electroplating (see Figure III.10).

The crystallinity and orientation of the electrochemical deposits also have an effect on the conductivity, but these factors and the opportunity for subsequent annealing of these deposits are not a focus of these efforts. Factors relating to the net increase in volume loading of copper (as seen in Figure III.9) as a result of electroplating were expressly removed by the methodology used to calculate the junction factors.

III.3.3.4 Impregnation method

Similar to the electroplating method, an impregnation method was employed to load additional metal onto fibers of MFM. The final location of the added metal is very important for improving the junction factor as well as the overall effective thermal conductivity. In the case of the impregnation method, the final location of the additional metal depends on many variables such as the concentration of the solution, drying temperature, surface tension and the affinity between the solution and the fiber surface, etc. The uniformity of the added metal is a significant challenge for this method. A slow drying process at a low temperature can move the added metal to the junctions via capillary action, while a fast drying process at high temperatures makes the metal more dispersed, even forming a secondary metal deposit with high porosity.

The resulting junction factor and thermal conductivity of the MEM modified by copper impregnation are seen in Figure III.11. Similar to the electroplating method, the impregnation method improved the effective thermal conductivity as more copper is added. However, the junction factor increased slightly with a small amount of added copper and declined slightly with a large amount of added copper. This result was attributed to the porous structure of the copper added by the impregnation method. As seen in Figure III.12, the SEM images of the MFM samples showed that the added copper was dispersed on the surface of the fibers and formed a structure with high porosity. This porous structure improved the conductivity, especially the conductivity of the junctions. Hence the junction factor increased as a small amount of copper was impregnated. As more copper was added, the additional copper was

dispersed on the top of the porous layer formed by previous impregnations and was not located at the junctions of the fibers.

Further annealing at 750°C for 1hour (Figure III.12.e) did not improve the junction factor. It appeared that under the conditions of this study the dispersed copper in the porous structure did not have sufficient driving force to migrate to the junctions.

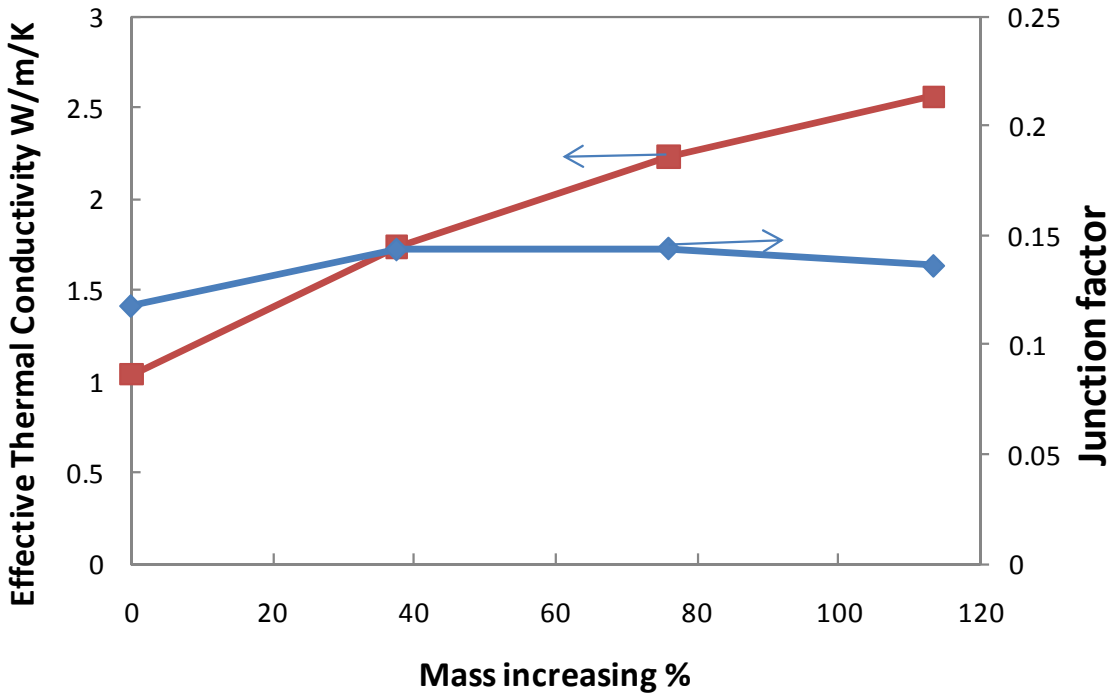

Figure III-11. Junction factor and effective thermal conductivity of Cu MFM modified by impregnation method

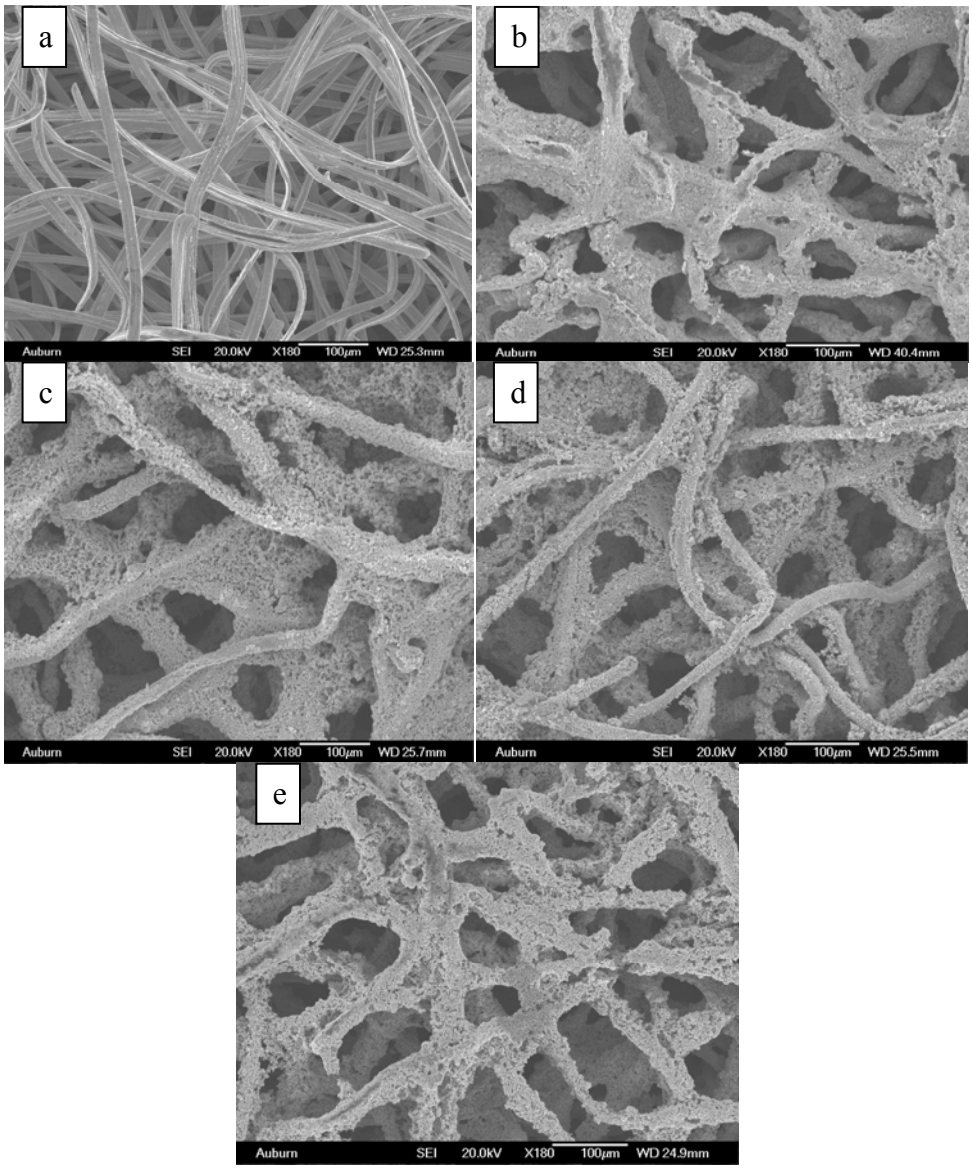

Figure III-12. SEM of Cu MFM modified by impregnation method; a) original Cu MFM after 550°C sintering; b) impregnation method with 4.5cc, mass increasing 37.5%; c) impregnation method with 9cc, mass increasing 75.9%; d) impregnation method with 13.5cc, mass increasing 113.4%; e) sample d after annealing at 750°C for 1 hour

III.4 Conclusions

The radial effective thermal conductivity of sintered MFM made of conductive metal is much higher than that of traditional packed beds. This improvement in thermal conductivity is the result of a sinter-locked network of metal fibers in the microfibrous structure which provides continuous metal channels for heat conduction that are much more effective than the point contacts in powdered packed beds.

A practical model taking the junction factor of fibers into account was developed to predict the radial effective thermal conductivity of MFM. Since this model takes the connection quality among fibers into consideration, it exhibited much better agreement with experimental results than previous efforts. Because the junction factor is easily determined by measuring the material's electrical resistance, this model and appropriate electrical measurements provide a facile method to determine the thermal conductivity of MFM.

The effect of sintering temperature and sintering time on Cu MFM was also studied. It was shown that higher sintering temperatures and longer sintering times improve the junction factor and effective thermal conductivity. The effects of additional copper being loaded onto Cu MFM were evaluated by electroplating and impregnation methods. Due to the different geometric structures of the added metal, the electroplating method was determined to be more efficient in improving the junction factor as well as the effective thermal conductivity of MFM. Overall, the following variables provided the best means to improve the thermal conductivity: sintering temperature > sintering time > electroplating >impregnation.

Acknowledgements:

This work was supported by the US Navy under a U.S. Navy contract at Auburn University (N00014-09-C-0208) administered through the Office of Naval Research. The authors want to thank IntraMicron (Auburn AL, US) for technical support.

Chapter IV: A Micro Scale Heat Transfer Comparison between Packed Beds and Microfibrous Entrapped Catalysts

Min Sheng, Donald R. Cahela, Hongyun Yang[1], William R. Yantz Jr., Carlos F. Gonzalez, Bruce J. Tatarchuk

Department of Chemical Engineering, Auburn University, Auburn, AL 36849, USA
[1] IntraMicron Inc., 368 Industry Dr., Auburn, AL 36832, USA

Abstract

Computational Fluid Dynamics (CFD) was used to compare the micro scale heat transfer inside a packed bed and a microfibrous entrapped catalyst (MFEC) structure. Simulations conducted in stagnant gas determined the thermal resistance of the gas in the micro gaps between the particle-to-particle contact points in the resistance network model of a packed bed. It was shown that thermal resistance at the contact points accounted for 90% of the thermal resistance of the solid path. In the MFEC, the thermal resistance of the continuous metal fibers was relatively smaller than that of contact points. As a result, 97.2% of the total heat flux was transported by continuous fiber cylinders, which was the fundamental function of fibers on improving the heat transfer of MFEC structures. Enhanced heat transfer characteristics of MFEC were further demonstrated by simulations performed in flowing gas, where both heat conduction and heat convection were significant.

Keywords: Computational Fluid Dynamics (CFD), Microfibrous Entrapped Catalyst (MFEC), Packed bed, Heat transfer, Resistance network model

IV.1 Introduction

Computational Fluid Dynamics (CFD) is a powerful analysis and design tool used to study reactor engineering characteristics and to provide insight into heat transfer, mass transfer, chemical reactivity, and heat generation in a micro scale. The CFD model has been successfully used to predict the fluid flow and pressure drop of fixed bed reactors [119], estimate diffusion and chemical reaction behavior with heat and mass transfer in porous catalyst pellets [120], and investigate the surface kinetics of heterogeneous catalysts [121].

For the purpose of heat transfer study, the first 3-dimensional CFD simulation of a packed bed structure was performed by Derkx and Dixon [122]. They simulated three spheres with a tube-to-particle ratio (N) of 2.14, and reported a strong agreement of the Nu number with the value predicted by model-matching theory based on experimental measurements. Moreover, they studied fluid flow and heat transfer inside fixed beds [123], heat transfer near the wall [124-126], convective heat transfer [127], and heat transfer in a packed bed used for a steam reforming reaction [128-130]. Several other papers examined the heat transfer in packed beds. Romkes et al. [131] performed a study on mass and heat transfer using CFD modeling and experimental validation for a composite structured catalytic reactor packing with a low N value. Guardo [132] discussed wall-to-fluid heat transfer in packed beds using different turbulence models. Guardo [133] also studied the convective heat transfer of fixed bed reactors at various pressures. Despite these numerous studies, using CFD to study heat conduction without the interaction with heat convection in packed beds has been seldom done.

The CFD modeling of heat conduction through packed beds can provide information to determine the potential limiting terms of heat transfer. For example, a resistance network

model (Figure IV-1.a) which separated the thermal conductivity of packed beds into a series/parallel combination of the individual resistances of conduction paths was discussed by Dixon [71], Slavin [115], and Bahrami [116]. The equation for this model was the following:

$$R = \left[\frac{1}{(1/R_{solid}+1/R_{gas})^{-1}+R_S} + \frac{1}{R_G}\right]^{-1} \quad \text{(IV-1)}$$

So far, there is no method or measurement that is capable of accurately determining the individual terms in this equation. The major difficulty is the inability to measure the temperature profile in a micro scale used to estimate the thermal resistance of point contacts (R_{solid}) and the thermal resistance of gas in micro gaps (R_{gas}). The common consensus based on empirical correlations or regressions is that the high thermal resistance between particle-to-particle contact points is the limiting term of heat transfer in packed beds. The simulation using CFD provides a clear temperature distribution in the micro scale and thereby serves as a potential method to determine the heat transfer behavior around the particle-to-particle contact points.

Due to the high thermal resistance between contact points, packed bed structures with poor heat transfer characteristics are not suitable for highly exothermic or endothermic reactions/processes. For these reactions or processes, catalyst structures with high thermal conductivity are required to enhance intra-bed heat transfer and reduce temperature excursions in the reactors. Microfibrous entrapped catalyst (MFEC) made of sintered micron diameter fibers with small catalyst particles entrapped within the network of fibers is one such catalyst structure [83-88]. It can be made of highly conductive metal fibers to satisfy heat transfer

requirements. The high effective thermal conductivity of metal MFEC has been determined by our experimental measurements [111], but a full understanding of the function of the metal fibers on improving heat transfer behavior is needed.

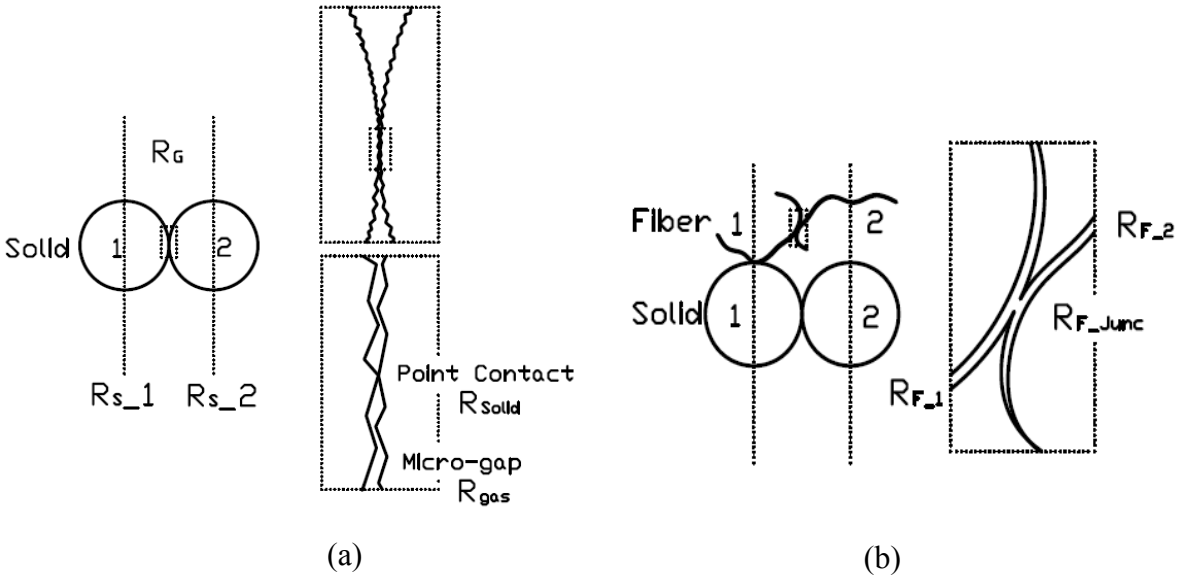

(a) (b)

Figure IV-1. ketch of the resistance network model for PB (a) and MFEC (b).

The CFD model has already been used to study pressure drop and mass transfer behavior of MFEC structures. By using a 2-dimensional CFD model, Kalluri [134] studied the effects of the fibers on the mass transfer of hexane adsorption and reported a significant improvement of the mass transfer rate at high gas velocities. Duggirala [135] investigated the effects of fiber diameter on pressure drop and external mass transfer rate with a 3-dimensional CFD model. It was found that the pressure drop did not change significantly by varying the fiber diameter from 2μm to 8μm, while MFEC with small size fibers resulted in an enhanced external mass transfer rate up to 70-80% over that of a packed bed of the same size particles.

In this paper, a CFD approach (Fluent) was utilized to estimate the micro scale heat transfer of MFEC to determine the enhancements in heat transfer compared to a packed bed of equal particle size. Simulations have been conducted in both stagnant gas and flowing gas environments.

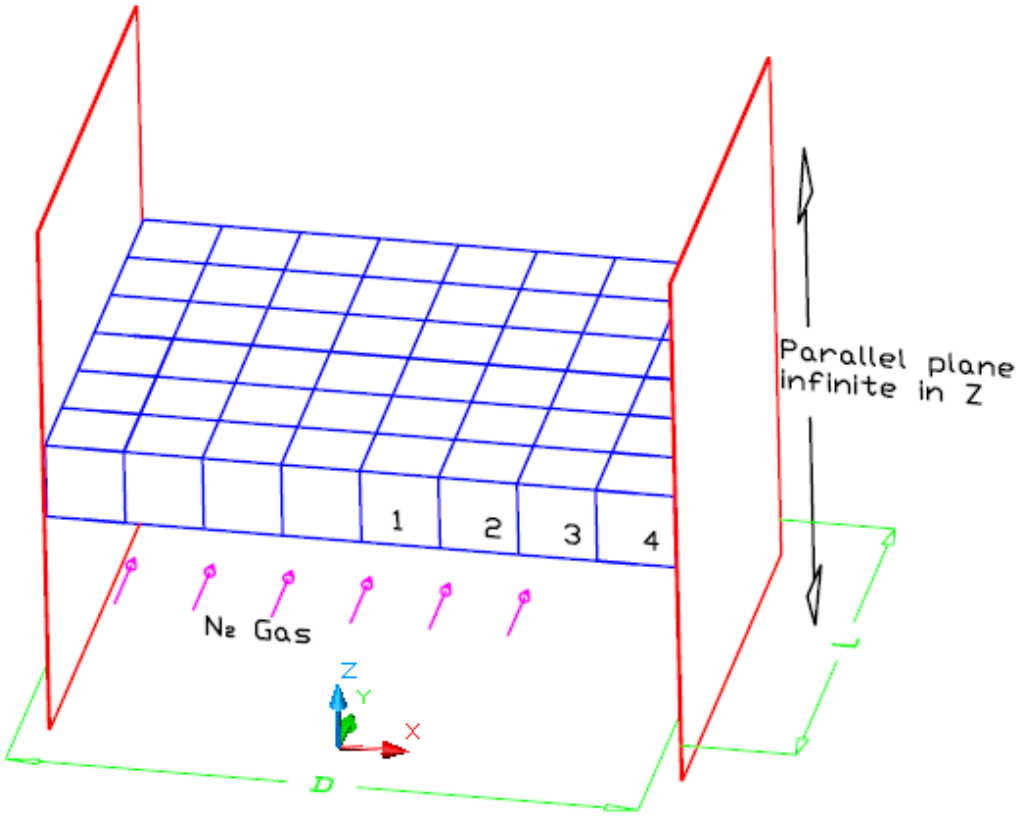

Figure IV-2. Parallel plate heating problem for CFD simulation

IV.2 CFD models

IV.2.1 Geometrical models

Due to computational limitation and geometrical complications, most CFD studies of packed beds were limited to a low tube-to-particle ratio (*N*). For example, Logtenberg and Dixon [123] used a packed bed with *N*=2.86, Guardo et al. [133] studied a packed bed of 44 spheres with *N*=3.923, and Dixon et al. [130] examined a packed bed reactor with *N*=4. If a packed bed had a large *N* value, a Cartesian geometrical model with symmetry boundary conditions was generally used to reduce mesh size and computation time. For instance, Yang et al. [136] showed pressure drop and convective heat transfer in structured packed beds using a Cartesian geometrical model. A Cartesian geometrical model was also utilized by Duggirala [135] to study the mass transfer of MFEC.

In our experimental measurements of the thermal conductivities of an alumina packed bed and MFEC, a tube (35.9mm ID) packed with alumina particles (177~250μm) was used. This corresponded to an *N* value equal to 173. The simulation of the experimental thermal conductivity measurement could not be easily performed, so a simpler geometry was used. Two parallel plates served as heat sources and a packed bed or a MFEC bed between them served as a heat path (Figure IV-2). It was assumed that the alumina particles in the CFD model were perfect spheres and the copper fibers were straight cylinders. The diameter of the alumina spheres was set to be the geometric mean diameter of experimentally tested particles, and the diameter of the fiber cylinders was set to be 12μm (Table IV.1). The void space was filled with N_2 gas, of which both density and thermal conductivity were temperature dependent [75]. The thermal conductivities of alumina particles and copper fibers were constant:

7.24W/m-K for alumina particles (the volume-averaged combination of the interstitial thermal conductivities of alumina solid and void inside,

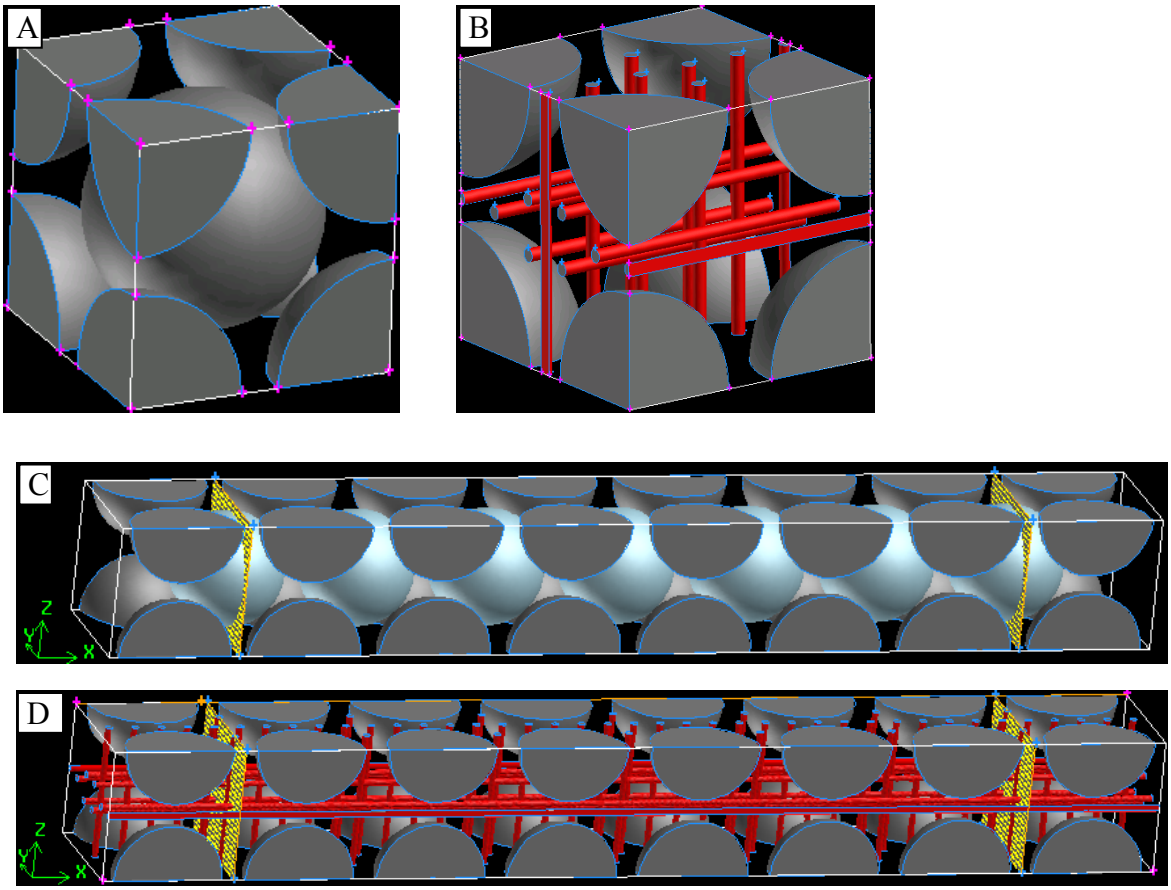

Figure IV-3. Geometrical models for packed bed and MFEC: A, Unit cell of packed bed; B, Unit cell of MFEC; C, 8 unit cells of packed bed for stagnant gas simulation; D, 8 unit cells of MFEC for stagnant gas simulation. Packed bad, 66vol.% Al_2O_3; MFEC, 3.6vol.% Cu metal, 29.4vol.% Al_2O_3.

1.14cc/g intra-particle pore volume) and 398W/m-K for copper fibers. A body centered cubic (BCC) structure that has 32% void volume by cubic close packing was chosen for the geometrical model of the packed bed shown in Figure IV-3.A. The edge length of a unit cell of the packed bed was 239.02μm and the diameter of the sphere was set to be 99% of the original diameter (207μm) to obtain a 34% voidage. For the MFEC structure, a simple cubic lattice was applied for the arrangement of the alumina spheres, and fourteen straight cylinders representing the metal fibers were distributed among those spheres. To obtain the same volume fraction of alumina as the experiments, the edge length of the unit cell of the MFEC model was extended to 250.9μm. Since surface contacts introduced drastically skewed meshes, the fiber cylinders and the alumina spheres in this model did not touch each other. Moreover, due to the preferential fiber orientation in the MFEC structure and the separated disk stack loading in a tubular reactor, the fiber cylinders were located evenly along the X-axis and Z-axis (Figure IV-3.B).

Due to the complexity of the interface between catalyst beds and the reactor wall, the contact situation for boundary unit cells is difficult to determine so that the wall effect is well represented. Since the heat transfer inside the catalyst structures was the focus of this study, simplified boundary unit cells were used. Fibers along the X-axis in MFEC structure had their ends touching the wall with zero heat flux at that ends. The data used to calculate the effective thermal conductivity was extracted from two plates that were one unit cell away from the walls, shown in Figure IV-3.CandD.

First of all, to investigate heat conduction without the contribution of heat convection, the packed bed and the MFEC were studied in a stagnant gas environment. The void space was filled with N_2. Only one row with eight unit cells along the X-axis (the front row in Figure IV-2) was simulated. Symmetry boundary conditions were applied on both the Y and Z directions, as shown in Figure IV-3.C and D. Heat flux was transported by the packed bed or the MFEC from the hot plate (100˚C) to the cold plate (20˚C) and the temperature distributions were then used to determine the effective thermal conductivities of the materials.

Moreover, simulations were also conducted in flowing gas in the packed bed and MFEC structures to show the combined contributions of heat conduction and heat convection, and the effect of different gas velocities. Nitrogen gas flowed through the materials between two plates along the Y direction. An array of twenty-four unit cells (4×6, 1-4 columns in Figure IV-2) was calculated. Similarly, symmetry boundary conditions were used in the Z direction and also on the middle plate perpendicular to the X-axis (in Figure IV-4). For these simulations the temperature of both plates was kept at 100˚C and the gas at the inlet was held at 20˚C.

Table IV.1 Volume percent and particle size of the experimental samples and CFD models

		Volume percent %			Size /μm	
		Fiber	Al_2O_3	Void	Fiber	Al_2O_3
Experiment	Packed Bed	0	63.89	36.11	0	177~250
	Cu MFEC	7.43	29.4	68.6	4&12	177~250
CFD model	Packed Bed	0	66	34[1]	0	207[2]
	Cu MFEC	3.59	29.4	67.01	12	207[2]

Note: 1. void for sphere with 99% diameter of the original diameter
2. geometric mean size from surface and volume of alumina particles

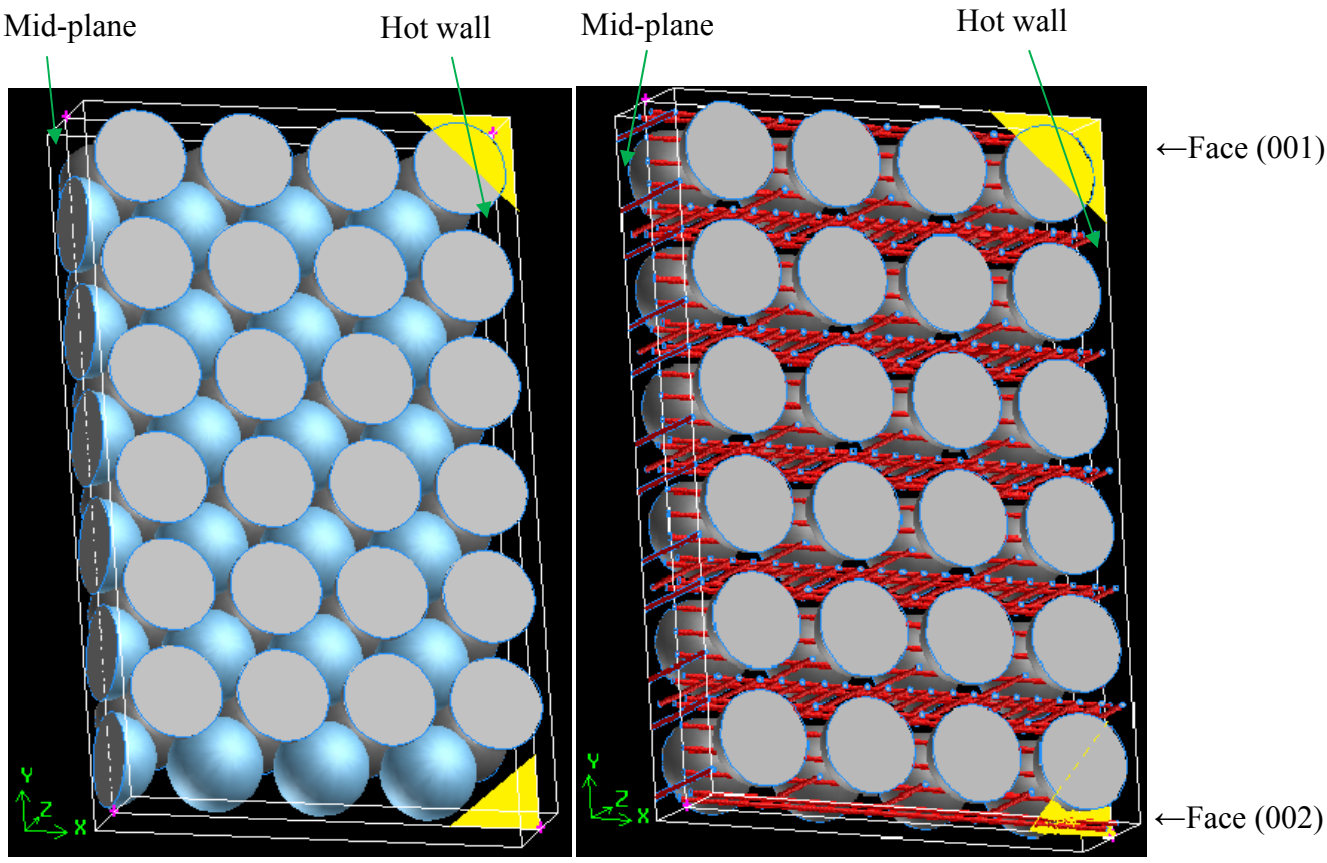

Figure IV-4. 6 by 4 unit cells for flowing gas simulations: left, packed bed; right, MFEC. Packed bad, 66vol.% Al_2O_3; MFEC, 3.6vol.% Cu metal, 29.4vol.% Al_2O_3.

IV.2.2 Near-miss" model for heat conduction in packed beds

Due to severely skewed meshes around the contact points inside packed beds, a “near-miss” model that creates a very small gap between two "touching" surfaces was proposed by Nijemeisland and Dixon [127]. They reported that a “near-miss” model with 99% of the original sphere diameter strongly agreed, in terms of velocity distribution, with a touching model with 100% of the original sphere diameter. There has been no study about the effect of this “near-miss” model on heat conduction and heat convection of packed beds. Since heat convection primarily depends on the fluid behavior that has been sufficiently addressed in their result, it is reasonable to believe that a good “near-miss” model is adequate to predict the heat convection in a packed bed. However, heat conduction is related to many other variables. Therefore, the verification of a “near-miss” model on heat conduction of a packed bed was carried out in stagnant N_2 gas, which had little or no interaction with heat convection. A series of models with a sphere diameter that was 95, 97, 98, 99 and 99.5% of the original diameter were studied to examine the effects of gap size on the behavior of heat conduction.

The comparisons of the models with 95, 97, 98, 99, 99.5% sphere diameters are illustrated in Figure IV-5. Since the thermal conductivity of N_2 gas (0.0258W/m-K) was much lower than that of solid alumina (7.24W/m-K), the large gaps in the 95% and 97% diameter models introduced a high thermal resistance for heat transfer. As a result, the effective thermal conductivities of these diameter models were smaller than the others. It was believed that the gap between the spheres was very important to the heat conduction behavior in the packed bed. Smaller gaps or no gaps at all were more appropriate, but they required very small mesh elements in order to avoid highly skewed meshes and large dispersion errors. Consequently,

the touching model never reached convergence in our calculations. Therefore, there is a compromise between the selection of gap size and accurate heat transfer results. Since both the 99 and 99.5% diameter models had close effective thermal conductivities, the 99% sphere diameter for the packed bed was used to reduce the skewed mesh and accelerate the convergence in further studies.

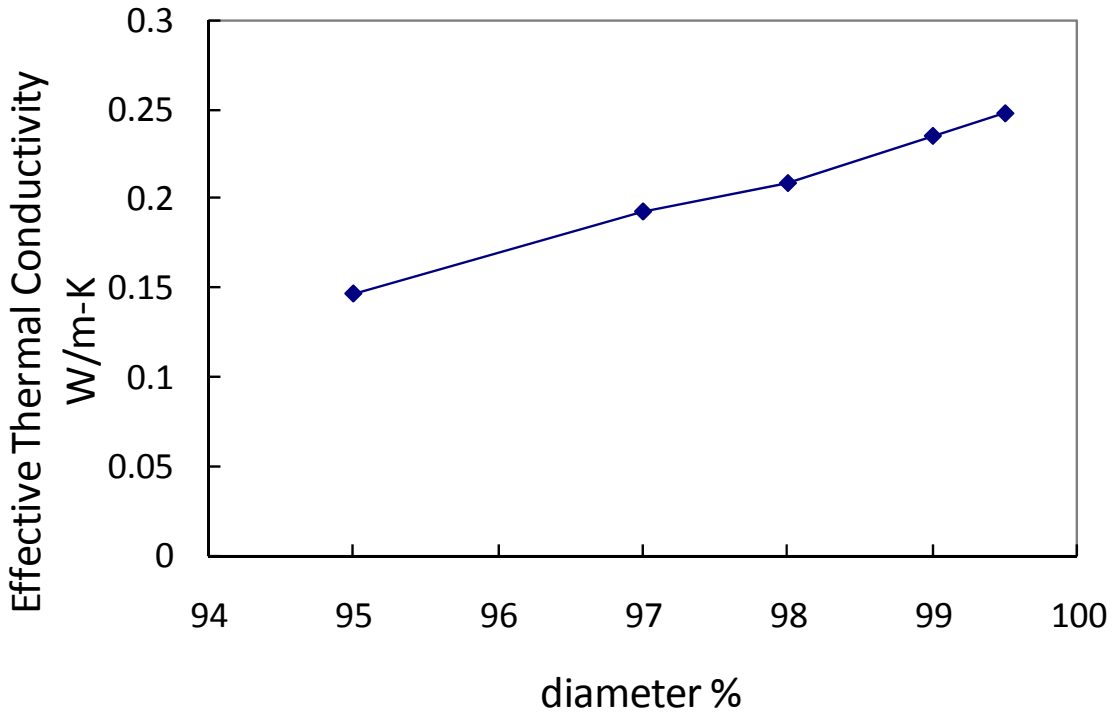

Figure IV-5. Effective thermal conductivity of packed bed with different gap sizes

IV.3 Results and discussion

IV.3.1 Stagnant gas cases

Since the symmetry boundary conditions applied on both the Y and Z directions, the stagnant gas simulation actually simulated the material sitting between two infinite plates. By

setting one plate at 20˚C and the other at 100˚C, the heat from the hot plate flowed through the packed bed or MFEC to the cold plate. As a result of their different heat transfer properties, the temperature distribution of the packed bed strongly contrasted to that of the MFEC.

The temperature distribution of the packed bed is demonstrated in Figure IV-6 and the temperature profiles of the straight lines indicated on the face (011) are shown in Figure IV-7. It was noticed that the isothermal temperature profiles approximated the geometrical surfaces of the alumina spheres, so that the temperature inside each of the spheres was nearly uniform. The wall effect in the packed bed was indicated as a loose packing density of spheres in the boundary unit cells (e.g., no hemispheres on face (002)) and the untouched geometrical structure of the boundary spheres with the wall. Therefore, the temperature gradient in the boundary unit cells ($\Delta T_{av} = 17.1$℃) was higher than those in other non-boundary unit cells ($\Delta T_{av} = 7.5$℃). This implied a higher thermal resistance in this region. Except for the boundary unit cells, all unit cells showed a similar temperature gradient (Figure IV-7) that reflected that they had a similar thermal resistance. Figure IV-8 showed that a significant temperature jump of 3.5˚C was found at the contact points between two neighboring spheres in the packed bed, while the temperature gradient through the alumina sphere was only 0.4˚C.

Figures 9 and 10 illustrate the temperature distribution of the MFEC structure, including a very large temperature gradient within boundary unit cells and a slight change in other unit cells. Because the inside wall heat transfer coefficient was the limitation term of the overall heat transfer coefficient in the MFEC, it was observed that the most drastic temperature gradient in the MFEC was contained in the regions very close to the walls. The temperature

gradient of the non-boundary unit cells in the MFEC ($\Delta T_{av} = 2.1$℃) was much smaller, compared to that of the boundary ones ($\Delta T_{av} = 33.7$℃, Fig.10). The temperature gradient in a non-boundary unit cell of the MFEC was much smaller than that of the packed bed (Figure IV-7). According to the work of Nijemisland et al. [126], this suggested that the effective thermal conductivity of the MFEC was higher than that of the packed bed.

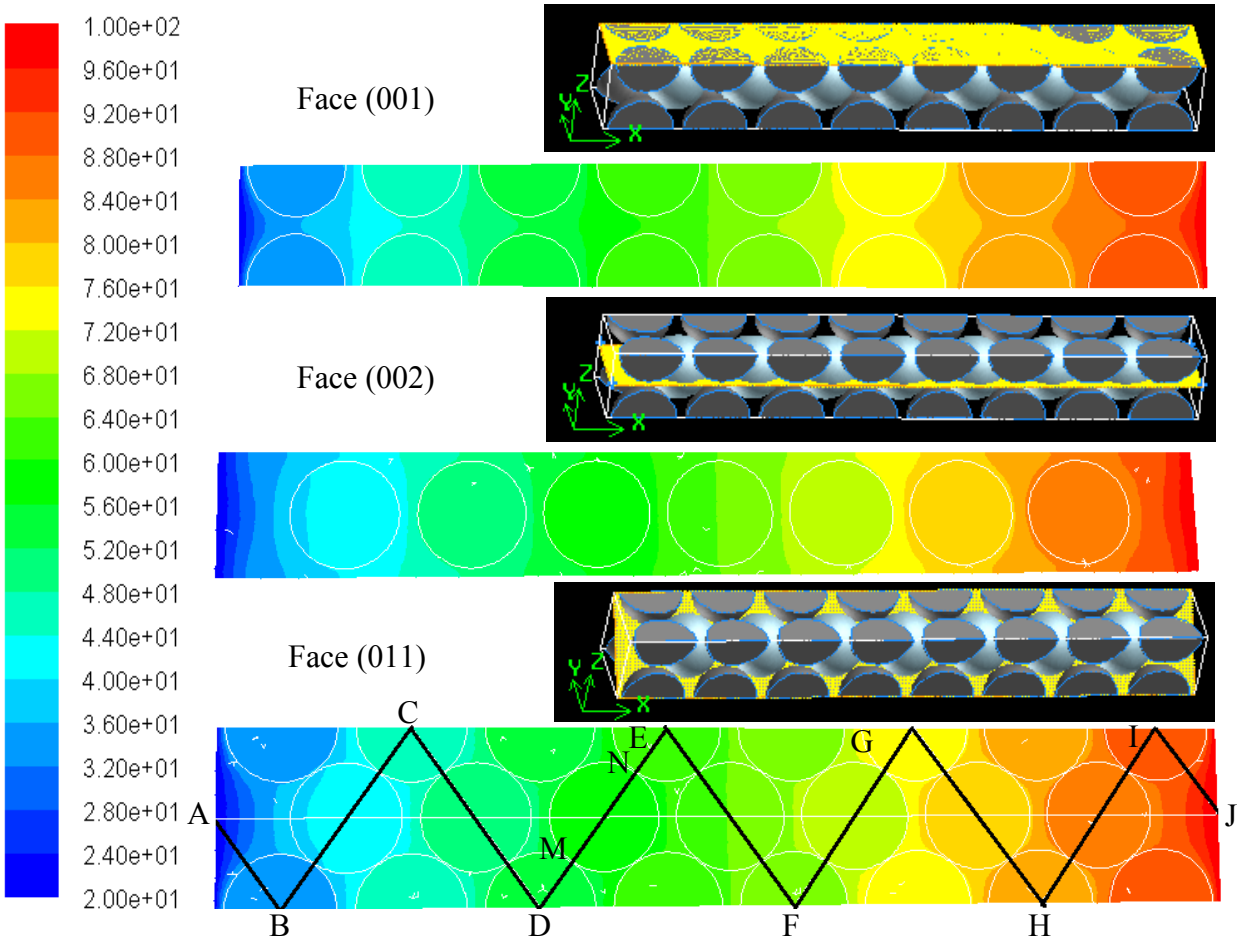

Figure IV-6. Temperature distribution of alumina packed bed in stagnant gas simulation; 66vol.% Al_2O_3 and 99% diameter model.

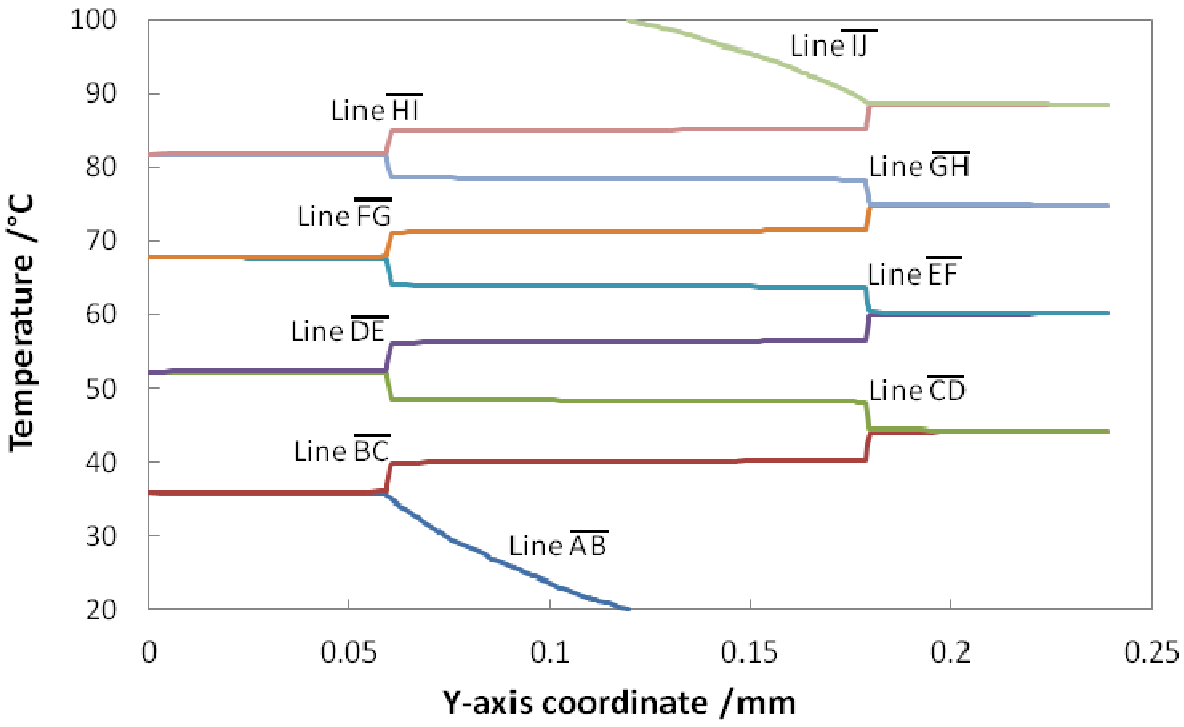

Figure IV-7. Temperature profiles of the straight lines on face (011) of the packed bed along the Y-axis; location of the straight lines shown in Fig.6; the packed bed with 66vol.% Al_2O_3 and 99% diameter model.

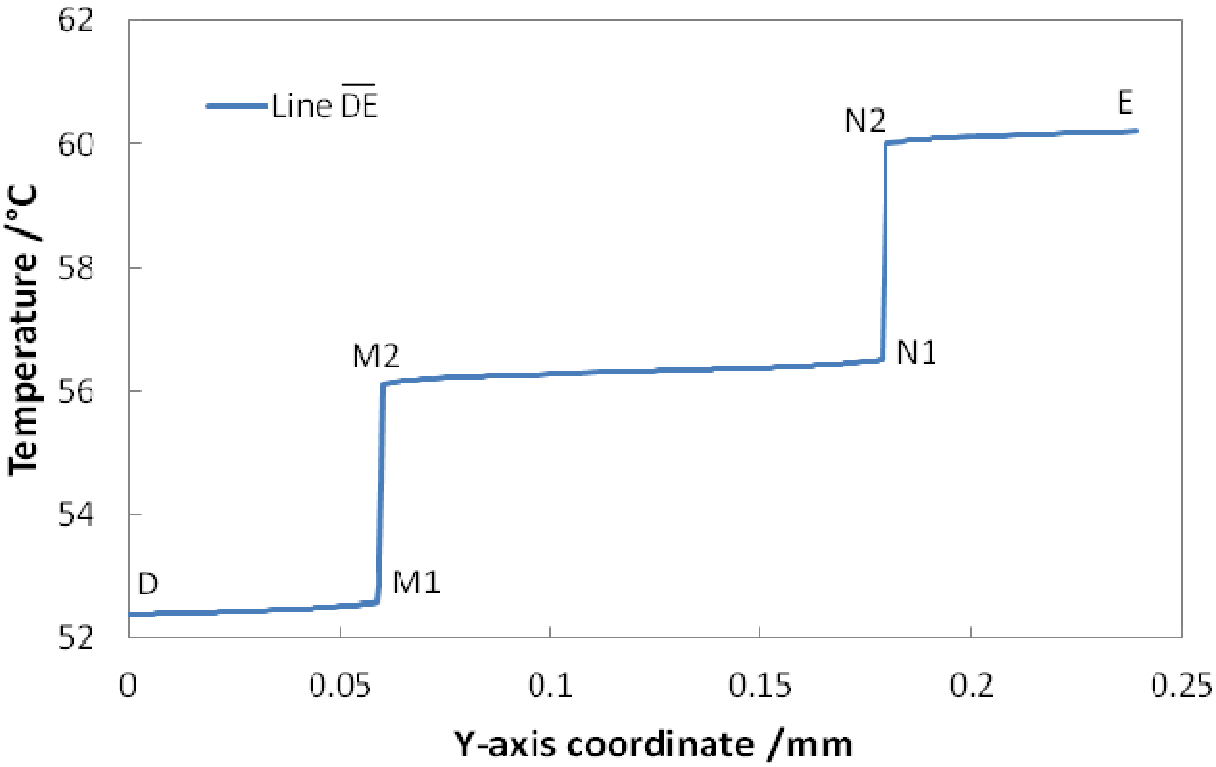

Figure IV-8. Temperature profile of line $\overline{DE}$ in the packed bed

Effective thermal conductivity could be obtained from the temperature distribution of the CFD result as the following:

$$k_e = \frac{Q}{A_c} \cdot \frac{L}{\Delta T} \tag{IV-2}$$

To avoid the wall effect on boundary unit cells, both the temperature difference (ΔT) and the heat flux (Q) were extracted from two plates that were one unit cell away from the walls (Figure IV-3). As listed in Table IV.2, the effective thermal conductivity and thermal resistance from the experiments and the simulations showed deviations for both the packed bed and MFEC. The deviation of the packed bed resulted from the higher solid volume in the CFD

model (Table IV.1) and the idealization of the physical shape of alumina particles. The significant discrepancy of the effective thermal conductivity of the MFEC attributed to the difference of the copper volume percentage between the experimental measurements (7.43vol% copper) and the CFD model (3.59vol% copper, as listed in Table IV.1). The copper volume percentage in the CFD model was less than half of the experimental value. But a high volume percentage of copper required more cylinders in the CFD geometrical model, which would have introduced difficulty with building the spatial structure and meshing the geometrical model. Another source of the discrepancy was from the idealization of the complicated physical structure of the fibers. For example, straight cylinders were used to represent the copper fibers that are actually bent and tortuose in the MFEC structure. Additionally, the cylinders were purposely set along X and Z directions and separated from each other in the CFD model so that only half of the cylinders form continuous metal channels along the direction of heat flux. However, the effective thermal conductivity of the MFEC with 3.59% copper was still twenty-one times that of the packed bed. This confirmed the experimental result: fifty-six times that of the alumina packed bed for MFEC with 7.43% copper.

Table IV.2 Comparison of the experiment data with the results of CFD simulation

	Effective thermal conductivity (W/m-K)		Thermal resistance through one unit cell (K/W)	
	experiment	simulation	experiment	simulation
Packed bed	0.16	0.235	26,100	18,300
MFEC	9.05	4.9	440	816

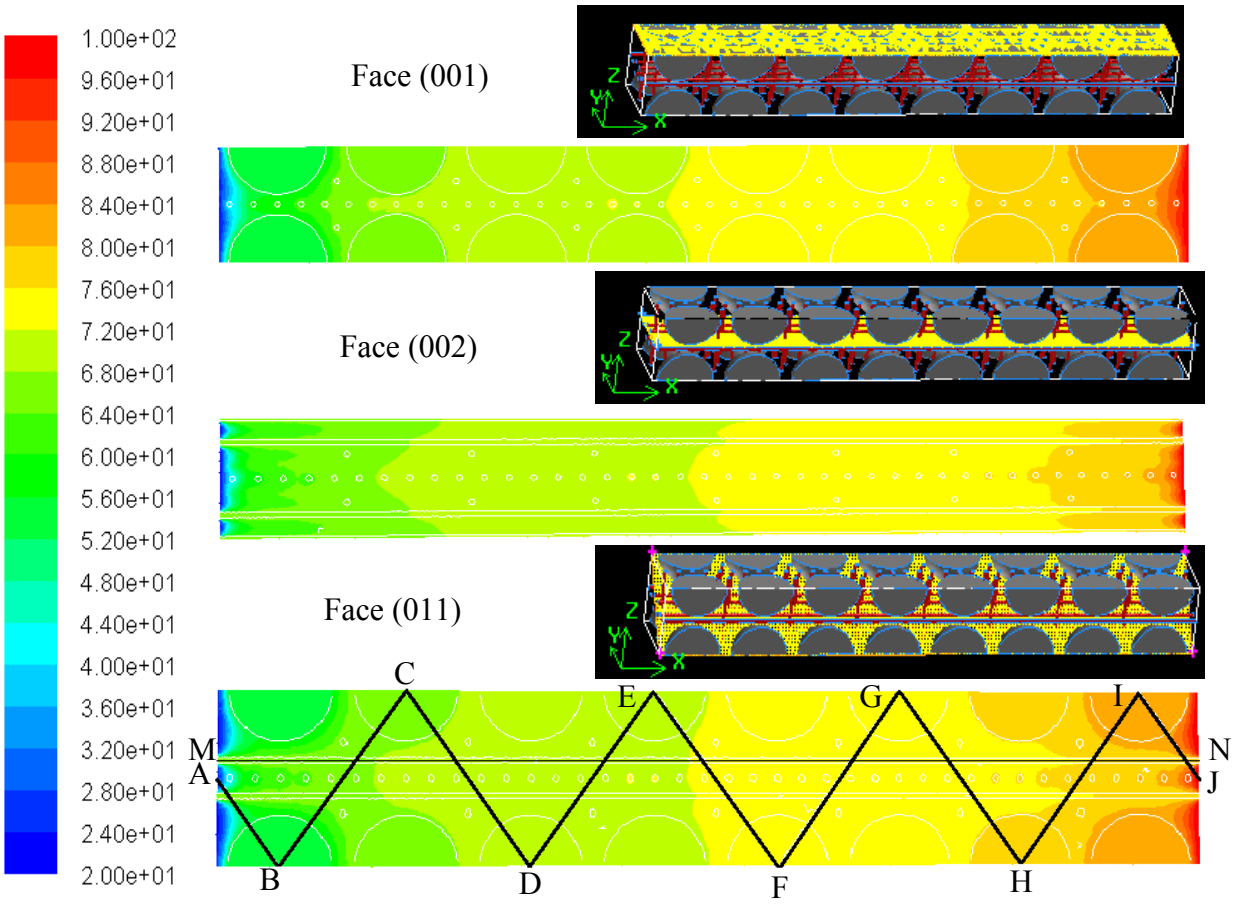

Figure IV-9. Temperature distribution of Cu MFEC in stagnant gas simulation; 3.6vol.% Cu metal, 29.4vol.% Al_2O_3.

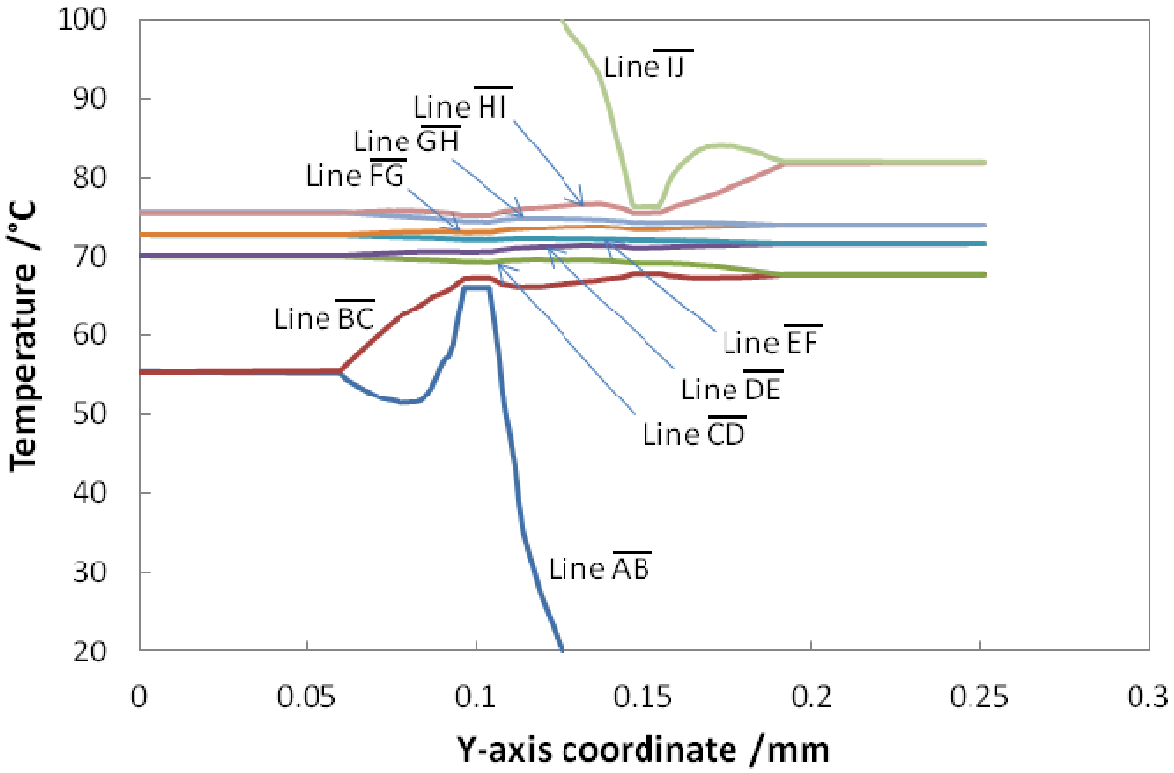

Figure IV-10. Temperature profiles of the straight lines on face (011) of MFEC along Y-axis; location of the straight lines shown in Figure IV-6; the MFEC with 3.6vol.% Cu metal, 29.4vol.% Al_2O_3.

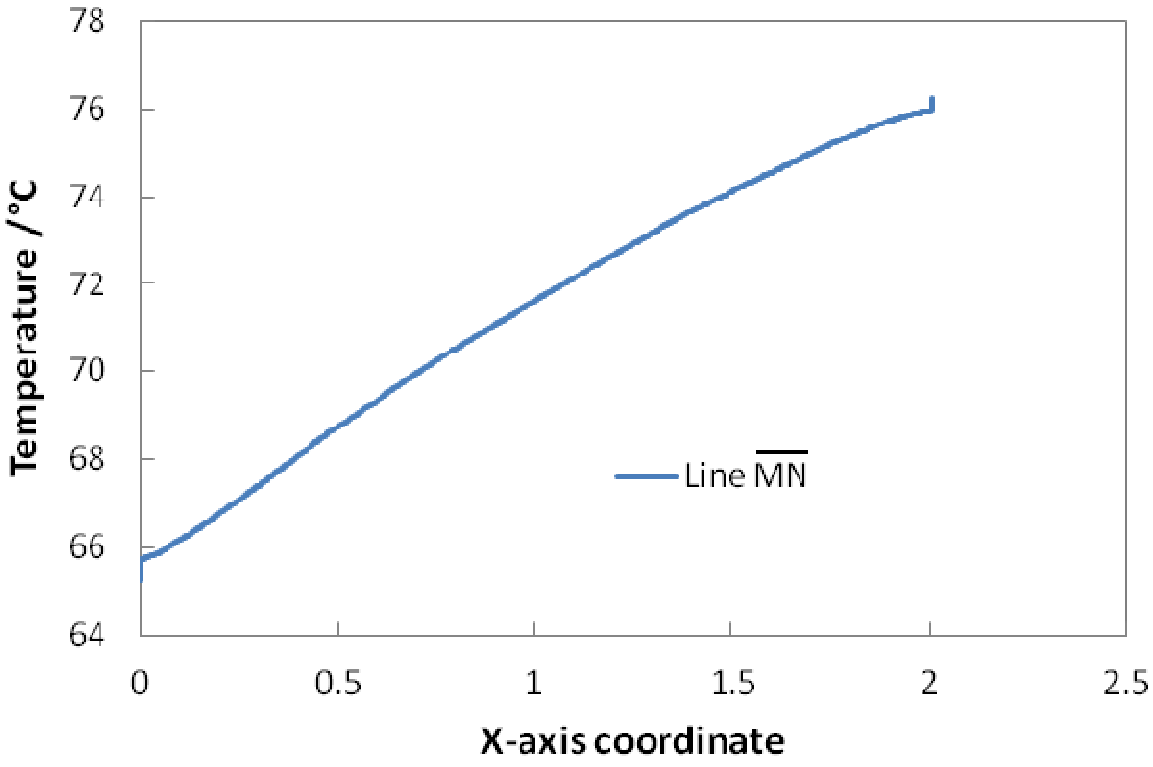

Figure IV-11. Temperature profile of line $\overline{MN}$ in MFEC

The temperature gradient of the boundary unit cells accounted for a significant portion of the total temperature gradient of both the packed bed and the MFEC (e.g., 43% for packed bed, 85% for MFEC). This suggested that the inside wall heat transfer coefficient was a limiting factor of the overall heat transfer coefficient in these CFD models. The boundary unit cells had different temperature distributions from the non-boundary unit cells. For example, the temperature profiles of line $\overline{AB}$ and $\overline{IJ}$ in MFEC (Figure IV-9) demonstrated dramatic temperature changes while these lines passed through the fiber cylinders that had a much higher or lower temperature than the surrounding gas (Figure IV-10). To avoid the complex

heat transfer behavior in boundary unit cells, two plates that were one unit cell away from the walls were used to calculate the effective thermal conductivity.

IV.3.2 Verifying resistance network model of packed bed

The internal temperature distribution from the result of the CFD simulation facilitates an accurate estimation for each term in the resistance network model of the packed bed (Eq.IV-1). Thermal resistance is determined by the following equations:

$$R = \frac{\Delta T}{Q} \tag{IV-3}$$

$$\text{or } R = \frac{L}{y \cdot k \cdot A} \tag{IV-4}$$

where Q is the heat flux through the conduction path and ΔT is the temperature difference.

Table IV.3 Thermal resistance of each term in the resistance network model of packed bed

Terms	R_s_1	R_{gas}_1	R_s_2	R_{gas}_2	R_s_3	R_G[1]	R_{solid}[2]	R
Path	$\overline{DM1}$	$\overline{M1M2}$	$\overline{M2N1}$	$\overline{N1N2}$	$\overline{N2E}$			
ΔT/K	0.2	3.5	0.4	3.7	0.21			
R/(K/W)	1.9E+03	3.3E+04	3.8E+03	3.5E+04	2.0E+03	5.1E+05	∞	1.83E+04

Note: 1. Calculated by Eq.IV-4
2. No point contact in CFD model

Among the temperature profiles of straight lines in the packed bed, the temperature rise along line $\overline{DE}$ of Figure IV-7 was highlighted in Figure IV-8 for the calculation of thermal

resistances (Table IV.3). The total heat transferred from the hot plate to the cold plate was 4.23×10^{-4}W. The path along line $\overline{DE}$ was considered as an individual solid conduction path, such that there were four such paths parallel to each other in this unit cell. Assuming that the total thermal resistance of the solid conduction paths was small enough compared to that of the bulk gas path, we concluded that all heat flux was transported through the solid paths. Consequently, the heat for one individual solid path was 1.06×10^{-4}W. The thermal resistance of each term in the solid conduction path can then be determined by Eq.IV-3, as listed in Table IV.3. In an individual solid path, the thermal resistance of the contact points (R_{gas}) was 90% of the total resistance. Thus the thermal resistance of the contact points was the limiting term of the effective thermal conductivity of packed beds. This resistance accounted for most of the temperature difference in the solid path. The total thermal resistance of four solid conduction paths was 1.89×10^{4}K/W, accounting for only 3.7% of the bulk gas path resistance, which verified the previous assumption. The total thermal resistance of the packed bed calculated from these individual thermal resistances using Eq.IV-1 was 1.83×10^{4}K/W. This gave an effective thermal conductivity of 0.23W/m-K, which was only a 2.5% deviation from the value calculated using Eq.IV-2. This verified the practicality of the CFD approach used to determine the individual terms of the resistance network model of a packed bed. Furthermore, by assuming the thermal resistance of solid spheres (R_s) to be zero, the thermal resistance from the contact points in the packed bed with stagnant N_2 gave an effective thermal conductivity of 0.25W/m-K. This value was believed to be the maximum effective thermal conductivity of the packed bed by changing the material of the spheres, for example, from alumina packed bed to

copper packed bed. This confirmed the experimental measurements of a low effective thermal conductivity of the packed bed made of copper particles [111].

IV.3.3 Verifying resistance network model of MFEC

For the MFEC structure, a modified resistance network model was proposed and correlated to experimental measurements (Figure IV-1.b):

$$R = \left[\frac{1}{(1/R_{solid}+1/R_{gas})^{-1}+R_S} + \frac{1}{R_G} + \frac{1}{R_F+R_{F\_jun}}\right]^{-1} \quad \text{(IV-5)}$$

In contrast to the packed bed, the determination of each term in this model was much more complicated, because R_S represented both the alumina particle and metal fibers in the MFEC structure and $1/R_{solid} + 1/R_{gas}$ referred to the point contacts of particle-to-particle, particle-to-fiber and fiber-to-fiber. The term $(1/R_{solid} + 1/R_{gas})^{-1} + R_S$ was always larger than R_{gas} and the thermal resistance of micro-gap gas (R_{gas}) in MFEC was assumed to be similar to that in the packed bed. In addition, from the effective thermal conductivity, $R_F + R_{F\_jun}$ was determined to be 816K/W for one unit cell. So that the ratio of $(R_F + R_{F\_jun})/[(1/R_{solid} + 1/R_{gas})^{-1} + R_S]$ was smaller than 0.025 and that of $(R_F + R_{F\_jun})/R_G$ was only 0.002. Therefore, the total thermal resistance for MFEC made of highly conductive metals could be reduced to $R \approx R_F + R_{F\_jun}$.

The temperature profile of a continuous fiber cylinder along the X-axis is shown in Figure IV-11, where line $\overline{MN}$ is the centerline of the cylinder. Using Eq.IV-3, the heat passing through all fiber cylinders along the X-axis was determined to be 1.58×10^{-3}W. This value was

97.2% of the total heat flux through the MFEC. This confirmed that the continuous metal fibers were the primary conduction path for the heat transfer inside MFEC made of highly conductive metals. The fundamental function of fibers is to improve the effective thermal conductivity of the MFEC structure and enhance the heat transfer in a stagnant gas or with a low Reynolds number.

IV.3.4 Simulations conducted in flowing gas environments

In these simulations, N_2 gas flowed through the packed bed or the MFEC bed between two plates and the cold gas was gradually heated up along the direction of flow. Besides heat conduction of the materials, heat transfer by convection also influenced the temperature distribution.

The temperature distributions on face (001) and face (002) of the packed bed and the MFEC with gas face velocity of 0.05m/s are shown in Figure IV-13. The Reynolds number was 1.10 for the packed bed and 1.03 for the MFEC. The Reynolds number (Re) is determined by:

$$Re = \frac{\rho v D_p}{\mu(1-\varepsilon)} \tag{IV-6}$$

where D_p is the equivalent diameter of the sample, given by

$$\frac{1}{D_p} = \frac{S_p}{6V_p} = \sum \frac{y_i}{\varphi_i D_i} \tag{IV-7}$$

The temperature of the gas increased much faster in the MFEC than in the packed bed, which demonstrated the enhanced heat transfer characteristic of the MFEC. For the packed bed, the temperature profiles still matched the surfaces of the alumina spheres. As a result, the outlet

temperature profile of the packed bed was approximately parabolic (Figure IV-12). While in the MFEC, the temperature profiles followed the surfaces of the fiber cylinders. The temperature gradient along the X direction was reduced by the enhanced heat transfer of the continuous fiber cylinders so that the temperature profile of the outlet gas was much flatter in the MFEC (Figure IV-12). Similarly to the result of the stagnant gas simulations, the temperature gradient in the boundary unit cells showed that the inside wall heat transfer coefficient was the major limiting term in the overall heat transfer coefficient of the MFEC model.

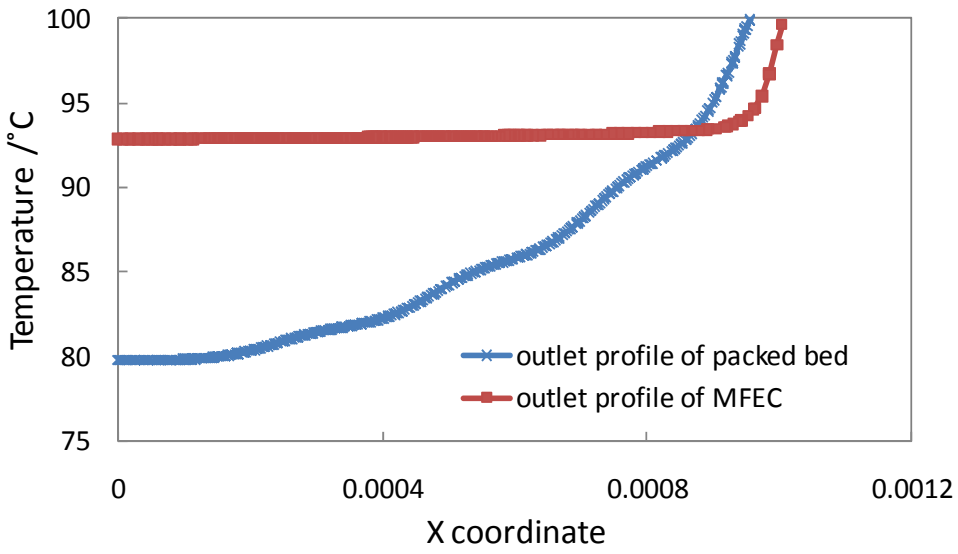

Figure IV-12. Outlet temperature profile along the X-axis for packed bed and MFEC.

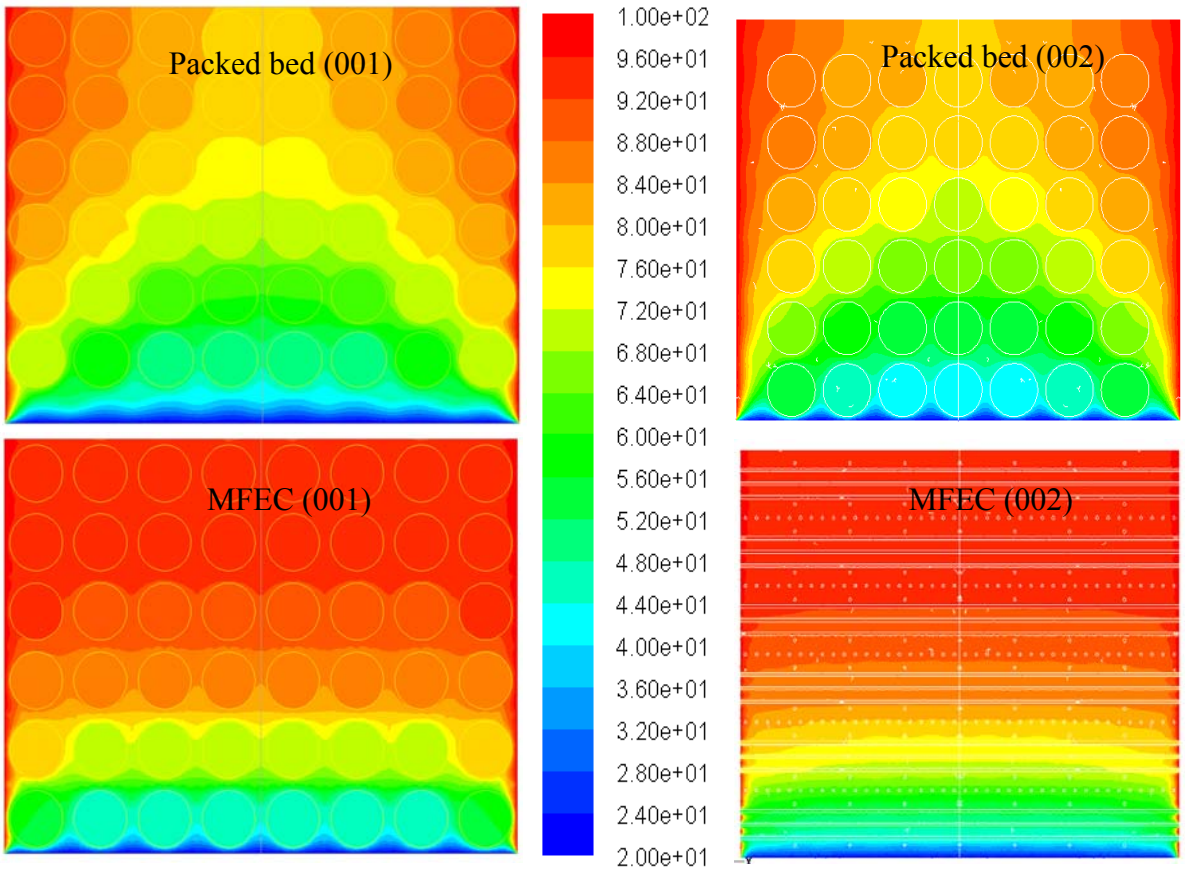

Figure IV-13. Temperature distribution of packed bed (upper) and MFEC (bottom) with N_2 at 0.05m/s; Packed bed, 66vol.% Al_2O_3 and 99% diameter model; MFEC, 3.6vol.% Cu metal, 29.4vol.% Al_2O_3; Positions of face (001) and (002) shown in Figure IV-4.

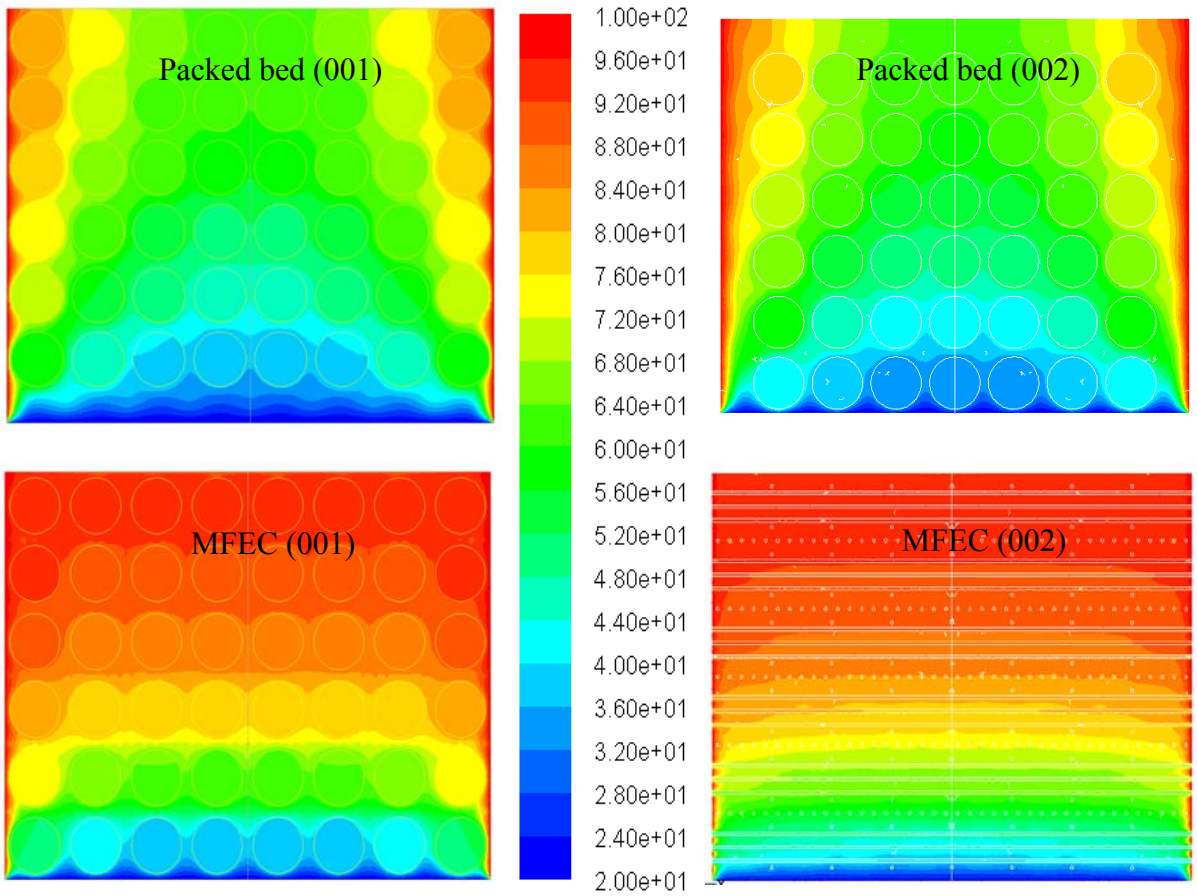

Figure IV-14. Temperature distribution of packed bed (upper) and MFEC (bottom) with N_2 at 0.2m/s; Packed bed, 66vol.% Al_2O_3 and 99% diameter model; MFEC, 3.6vol.% Cu metal, 29.4vol.% Al_2O_3; Positions of face (001) and (002) shown in Figure IV-4.

These two beds were also studied at various gas face velocities to investigate the influence of convection on the overall heat transfer. The temperature distributions for 0.2m/s face velocities, (Reynolds number 4.41 for the packed bed and 4.11 for the MFEC bed) are shown in Figure IV-14. Compared to the gas face velocity of 0.05m/s, the average gas temperature in the packed bed at high gas velocity greatly decreased and that of the MFEC did not change much. The different temperature distributions between the packed bed and MFEC confirmed experimental measurements, which showed that the effective thermal conductivity of MFEC greatly increased with gas velocity, but the packed bed did not. At a higher gas velocity, more cold gas coming from the inlet required a larger heat duty for the heat sink of the materials. The temperature profiles in MFEC followed the outlines of the fiber cylinders along the X-axis, especially the isotherm curves near the gas inlet. This means that the fiber cylinders are the predominate heat source from which heat was transferred to the gas phase by convection. The combination of a high heat transfer capacity along the continuous fibers and a large geometric surface area from using small diameter fibers resulted in a rapid increase of effective thermal conductivity of MFEC with gas velocity.

From results of the CFD simulation, the overall heat transfer coefficient of the packed bed model (Figure IV-2, L=1.434mm and D=1.912mm) and MFEC model (L=1.505mm and D=2.007mm) was calculated by the following equation:

$$U = \frac{q}{\Delta T_m \cdot A} \tag{IV-8}$$

where $\Delta T_m = \frac{T_{in} - \overline{T_{out}}}{\ln \frac{T_w - \overline{T_{out}}}{T_w - T_{in}}}$ (IV-9)

$\overline{T_{out}}$ is the mass-weighted average temperature of the outlet gas.

The resulting values were compared with those estimated from thermal parameters experimentally determined [111], shown in Figure IV-15. The deviations of the overall heat transfer coefficient for the packed bed are due to the higher solid volume in the CFD model and the idealization of the physical shape of alumina particles. The deviations for the MFEC are attributed to the smaller copper volume percentage in the CFD model versus the experimental data and the overestimation from the boundary fibers touching the wall in the CFD model.

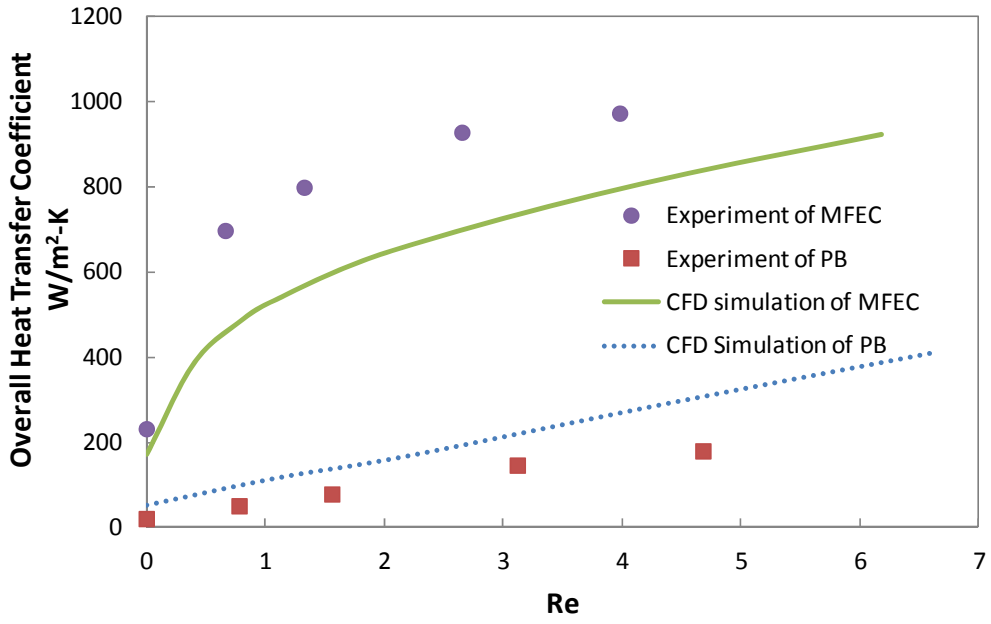

Figure IV-15. Overall heat transfer coefficient of packed bed (PB) and MFEC; ●: MFEC (7.4vol% copper) estimated from experimental determination; ■: Alumina packed bed

estimated from experimental determination [111]; ──: MFEC (3.6vol% copper) estimated from CFD simulations; ·····: Alumina packed bed estimated from CFD simulations.

IV.4 Conclusions

Due to difficulties in experimentally measuring the temperature profile in a micro scale, CFD provides a novel approach was utilized to predict the temperature distribution and estimate the thermal resistance at particle-to-particle contact points in packed beds. The thermal resistance of the contact points accounted for 90% of the thermal resistance of the solid path of the packed bed. Thus it was the limiting term of heat transfer inside packed beds.

Compared to the packed bed, MFEC offered continuous fibers with an individual heat path, which have a relatively smaller thermal resistance than contact points. As a result, 97.2% of the total heat flux was found to be transported by the continuous fiber cylinders. This suggested that the continuous metal fibers were the primary conduction path for the heat transfer inside the MFEC made of highly conductive metal. In addition, due to a high heat transfer capacity through the continuous metal fibers and a large geometric surface area from using small fiber diameters, the thermal conductivity of the MFEC increased faster than that of the packed bed with increased gas face velocity.

Acknowledgements:

This work was supported by the U.S. Navy under a U.S. Navy contract (N00014-09-C-0208) administered through the Office of Naval Research. The authors want to thank IntraMicron (Auburn AL, US) for technical support.

Chapter V: High Conductivity Catalyst Structures for Applications in Exothermic Reactions

Min Sheng, Hongyun Yang[1], Donald R. Cahela, William R. Yantz Jr., Carlos F. Gonzalez, Bruce J. Tatarchuk

Department of Chemical Engineering, Auburn University, Auburn, AL 36849, USA
[1] IntraMicron Inc., 368 Industry Dr., Auburn, AL 36832, USA

Abstract

Highly exothermic catalytic reactions are problematic from a thermal management perspective and often dictate the type of reactor, heat exchanger, level of conversion/recycle and contacting scheme that are employed. To investigate the opportunity for enhanced heat transfer structures, 15wt% Co/Al_2O_3 catalyst particles (149-177μm dia.) were examined in both a packed bed configuration and after being entrapped within a 7.4 vol.% network of sintered Cu fibers (12μm dia.). Fischer Tropsch Synthesis (FTS) at 225-255°C, 20bar, H_2/CO of 2.0, was utilized as the probe reaction due to its exothermicity and temperature dependent selectivity. Both the hot spot and runaway state were prevented by utilizing metal microfibrous entrapped catalyst (MFEC) compared to the packed bed. In a 41mm ID reactor, the maximum temperature deviation from the centerline to the reactor wall was only 6.4°C for the copper MFEC. In contrast, the packed bed diluted to the same catalyst density and operated at an equivalent condition had a centerline temperature deviation of 460°C indicating ignition. The more isothermal temperature profile through the catalyst bed of the copper MFEC led to a

higher selectivity of heavy products than that of the packed bed. Also, it enabled a larger reactor diameter to be used with more precise and robust temperature control.

Keywords: Microfibrous entrapped catalyst, packed bed, Fischer-Tropsch synthesis, overall heat transfer coefficient, Highly exothermic or highly endothermic reaction

V.1 Introduction

Typical packed beds with catalyst granules (e.g., 1 to 3 mm dia.) have poor thermal conductivities and high mass transfer limitations, which make them problematic for highly exothermic reactions. Metal microfibrous entrapped catalysts (MFEC, Figure V-1) developed in our laboratory provide an alternative approach for reactions confronting mass and/or heat transfer limitations [111]. It has been shown that in a stagnant gas the radial effective thermal conductivity of copper MFEC was 56 times that of an alumina packed bed, and the inside wall heat transfer coefficient was 10 times higher. The small catalyst particles (e.g., 10 to 100μm dia.) entrapped in MFEC enhance both the internal and external mass transfer rates thereby increasing both the effectiveness factor and the volumetric reactivity.

Fischer-Tropsch synthesis (FTS) was used as a probe reaction in this study because it is a highly exothermic reaction (ΔH= -165kJ/mol of CO) [28] with an adiabatic temperature rise of approximately 1600˚C depending on the product slate [29]. The main products of FTS are paraffinic hydrocarbons, based on the following equation:

$$n\,CO + (2n+1)H_2 = C_nH_{2n+2} + n\,H_2O \quad \Delta H = -165kJ/mol\_CO \tag{V-1}$$

The distribution of the paraffins is most simply described and modeled by the Anderson-Schulz-Flory (ASF) product distribution [18-20].

$$x_n = (1-\alpha)\cdot\alpha^{n-1} \tag{V-2}$$

The chain growth probability factor (α) for ruthenium, cobalt and iron based catalysts at typical operating conditions is 0.85~0.95, 0.70~0.80, and 0.50~0.70, respectively [21].

Efficient heat removal and the resulting intrabed temperature profiles are critical to the FTS process due to product selectivity and catalyst deactivation. The α value strongly depends on the temperature of the active sites and can be significantly reduced at higher temperatures [27,51]. Song et al. [54] proposed an empirical equation to estimate the dependence of the α value on temperature, as follows:

$$\alpha = (0.2332 \frac{x_{CO}}{x_{CO}+x_{H_2}} + 0.6330) \cdot [1 - 0.0039(T - 533)] \quad \text{(V-3)}$$

Figure V-1. SEM of copper MFEC with Co/Al_2O_3 particles; copper fiber 12μm, Co/Al_2O_3 particles 149-177μm

Furthermore, most of the reactants are consumed in the high temperature zone [29]. Should unwanted thermal runaway or the development of hot spots occur, methanation becomes the dominant reaction pathway [23]. A uniform temperature profile in a packed bed reactor permits maximization of the desired product selectivity. Uniform temperature profiles also reduce catalyst deactivation. Possible deactivation mechanisms of FTS catalysts include poisoning, crystallite sintering, carbon fouling, thermal degradation and re-oxidation [144]. Each deactivation mechanism is related to or accelerated by higher temperatures. Catalyst structures with enhanced heat transfer characteristics reduce the severity of hot spots and thermal runaway in packed beds and extend catalyst life.

To address the highly exothermic nature of FTS, various types of reactors such as fluidized bed reactors [41,12], slurry phase reactors [43,12], and multi-tubular fixed bed reactors[37,38] have been employed. As mentioned by Davis [14], fixed bed reactors remain an attractive approach because they have the highest volumetric catalyst loading and the highest potential volumetric productivity. They are also the easiest to scale to various levels, both large and small. Unfortunately, the poor thermal conductivity of packed beds results in serious temperature deviations between the centerline and the reactor wall [8,14,60]. To maintain thermal stability in a packed bed, reactors with small radii and multiple tubes have been used to overcome heat transfer limitations. It was found that the maximum radius of a packed bed reactor without gas recycle was 10mm, but preferably 7mm [30]. Supercritical media [46,53], metal monolith catalyst structures [47,48], metallic foams and corrugated packing with open/closed cross flow structures [78,79] are potential methods for use in FTS to improve intra-bed heat transfer. Compared to these alternative approaches, MFEC may have

some potential advantages such as higher catalyst loading, compatibility with pre-manufactured catalyst particles and enhanced effective surface kinetics.

In this paper, metal MFEC has been investigated for application to FTS to determine the enhancements in heat transfer that are available compared to a packed bed of equal particle size and catalyst loading operated at roughly equivalent levels of conversion and volumetric reactivity. Evaluations have been conducted using both 15 and 41mm ID tubular reactors.

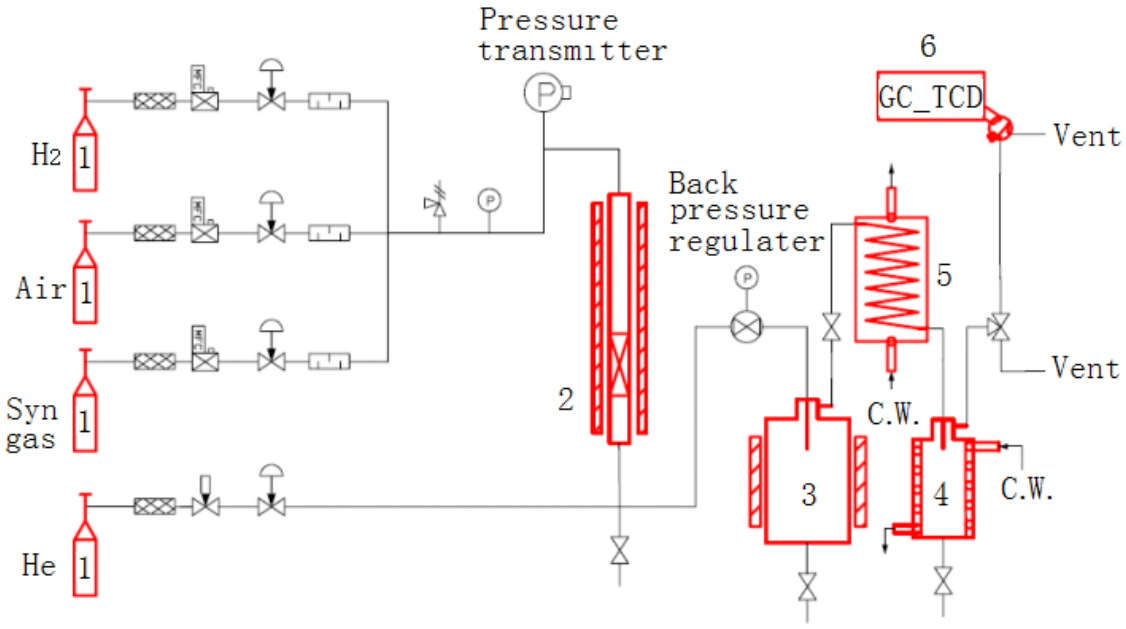

Figure V-2. FTS setup: 1, gas cylinders; 2, FTS reactor; 3, hot trap; 4, cold trap; 5, shell-and-tube cooler; 6, on-line GC.

V.2 Materials and methods

V.2.1 Apparatus

Two downflow tubular reactors were employed to compare the MFEC to the packed bed reactors. A schematic of the experimental apparatus is presented in Figure V-2. The 15mm ID reactor was a stainless steel tube with a wall thickness of 2.05mm. The 41mm ID reactor was made from a 1.5in. schedule 10 stainless steel pipe. Multipoint thermocouples (Omega, 316SS probe, 1.59mm OD, 0.15mm wall thickness, 6 points, 25.4mm interval) were used to measure temperatures in the catalyst beds. The thermal mass of these thermocouples was relatively small compared to the thermal mass of the catalyst beds. As listed in Table V.1, the thermocouple sheath represented less than 3.5% of the total thermal mass in the 15mm ID reactor. Moreover, the close temperature on thermocouple No 3 and 4 shown in Figure V-3 confirmed that thermal diffusion was negligible along the sheath of the thermocouple. From these observations, the presence of these thermocouples was assumed to have a negligible effect on the measured temperature gradient. The locations of the thermocouples in the catalyst beds of the reactors are shown in Figure V-4 and Figure V-5. Inside the 15mm ID reactor, one multipoint thermocouple was used at the centerline, and the catalyst bed was located between measurement points 2 to 6. Inside the 41mm ID reactor, two multipoint thermocouples were used; one at the centerline and the other at 15.4mm from the centerline. The catalyst bed started at point 2 on the thermocouple and extended to 25.4mm after point 6.

Table V.1 Thermal mass of each component in the 15mm ID reactor

	Thermal mass in 1cm length of catalyst beds			
	Packed Bed		Cu MFEC	
	J/K	%	J/K	%
Thermocouple (sheath)	0.027	3.4	0.027	3.2
Catalyst	0.765	96.6	0.358	42.9
Copper fiber	0	0	0.449	53.8
Total	0.792	100	0.834	100

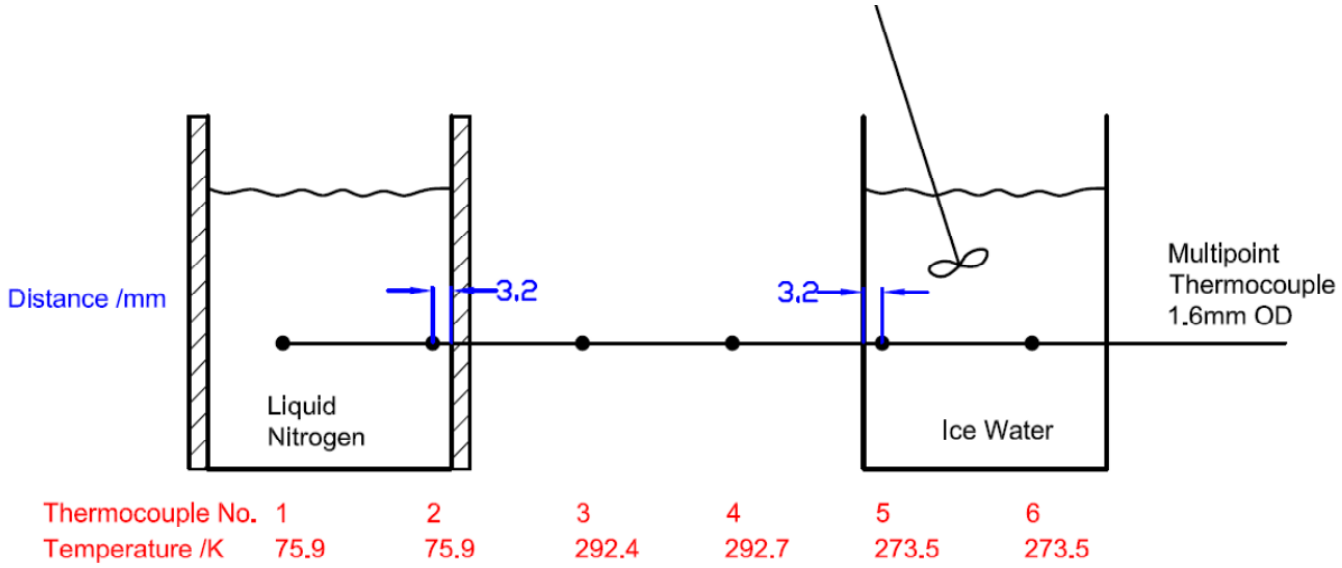

Figure V-3. Experimental investigation for thermal diffusion along the multipoint thermocouple.

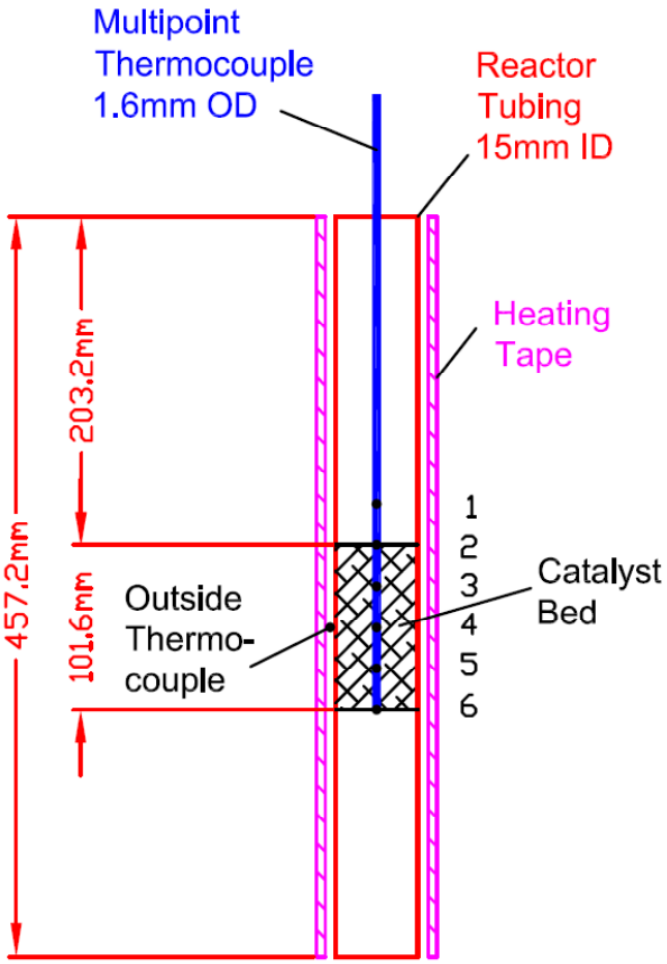

Figure V-4. The location of catalyst bed and thermocouple in the 15mm ID reactor; Outside thermocouple used for PID control of heating tape; Multipoint thermocouple with 25.4mm interval between points

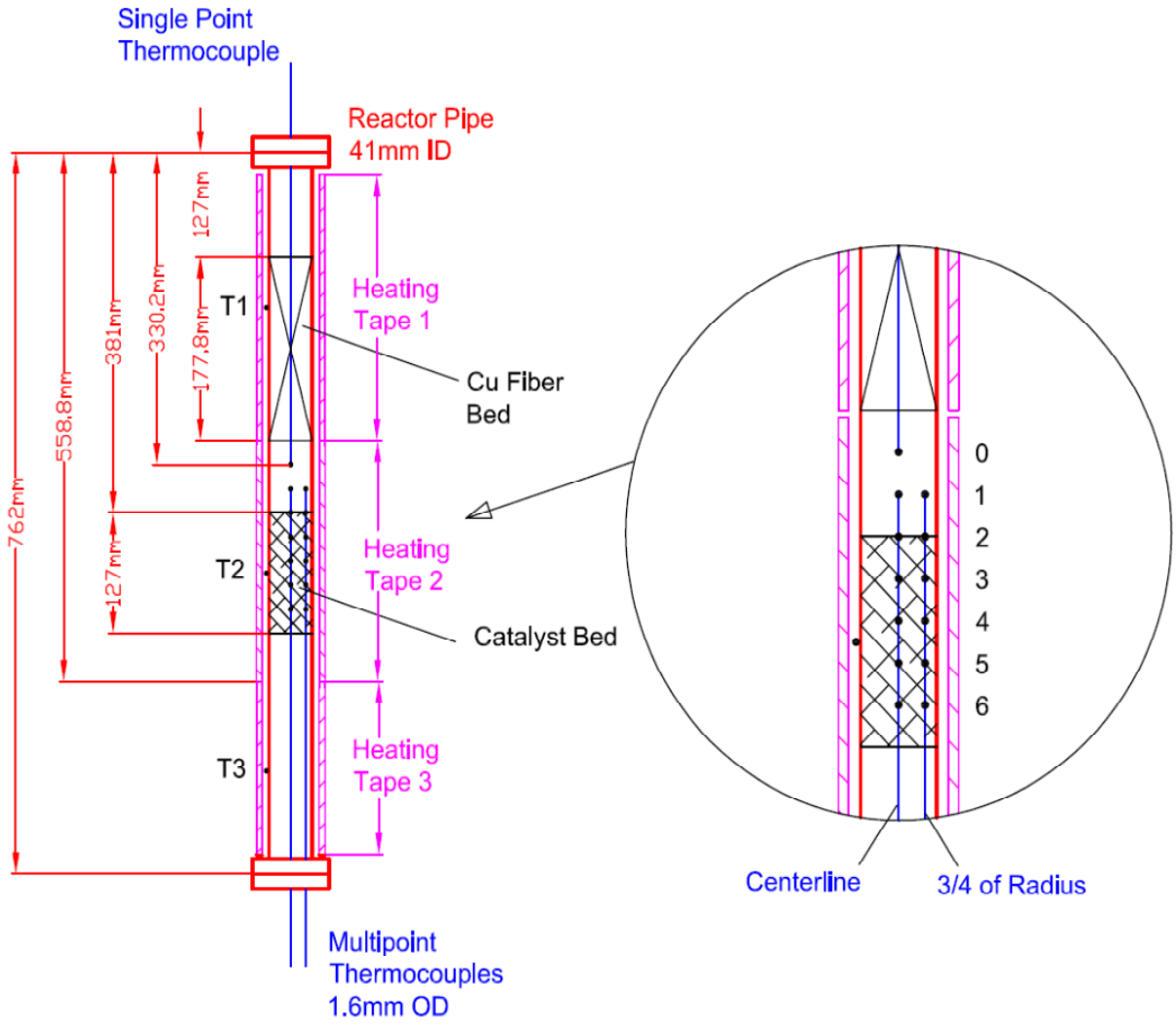

Figure V-5. The location of catalyst bed and thermocouples in the 41mm ID reactor; Outside thermocouple T1,T2 and T3 for PID control of heating tape 1, 2 and 3, respectively; Multipoint thermocouples with 25.4mm interval between points

V.2.2 Catalyst preparation and characterization

A 2.9M cobalt nitrate aqueous solution was used to prepare a catalyst with 15 wt% cobalt metal on γ-alumina particles (Alfa, pore volume 1.14cc/g, surface area 250m2/g, and 149-177μm) by incipient wetness impregnation. The catalyst was then dried at 383K in an oven overnight and calcined in air at 623K for 3h. After the installation of the catalyst bed inside the tubular reactors, the catalyst was reduced in situ with flowing hydrogen at 648K for 16h. The cobalt loading on the catalyst was determined using inductively coupled plasma–atomic emission spectroscopy (ICP–AES, Varian, Victoria, Australia).

Temperature programmed reduction (TPR) was carried out using 0.2g of the calcined catalyst with a mixture of 5% hydrogen in flowing argon at 15sccm. A thermal conductivity detector (TCD) was used to determine the consumption of hydrogen. The temperature was ramped at a rate of 10K/min from room temperature up to 1023K.

Nitrogen adsorption-desorption isotherms of the fresh alumina support and the calcined catalyst were measured on an Autosorb-1 (Quantachrome Instruments) at 77K. Samples were degassed at 473K for 3h prior to the isotherm measurements. The total surface area was calculated via the Brunauer-Emmett-Teller (BET) equation. The pore size distribution was determined from the Barrett-Joyner-Halenda (BJH) adsorption pore size distribution method.

Hydrogen chemisorption isotherms were recorded on an Autosorb-1 at 313K. A sample of the calcined catalyst (0.25g) was evacuated at 423K for 1h and then reduced in flowing hydrogen at 648K for 16h. After reduction, the sample was evacuated for 1h at 648K and 30min at 423K before cooling to 313K. At this temperature, the chemisorption isotherm was

recorded in the pressure range of 80-800mmHg. Both the first adsorption isotherm and the weak reversible second adsorption isotherm were recorded and the amount of strongly chemisorbed hydrogen was determined from the difference. The stoichiometric ratio of cobalt to H_2 was set to be 2:1, and the average cobalt metal crystallite size (d_{cry}) was estimated based on the assumption of spherical uniform cobalt metal particles and the reduced cobalt fraction from TPR results [137]. The following equations were used:

$$Disp\ (\%) = \frac{number\ of\ Co^0\ atoms\ on\ surface}{(total\ Co\ atoms\ in\ sample) \times (fraction\ reduced)} \times 100$$

$$d_{cry}(nm) = 96/Disp\ (\%) \qquad \text{(V-4)}$$

X-ray diffraction (XRD) was conducted using a Bruker D8 with monochromatized Cu/K_α radiation. Using the Scherrer equation [138], the average size of the Co_3O_4 crystallites in the calcined catalyst was estimated from the peak of Co_3O_4 at $2\theta=36.8°$. Lanthanum hexaboride was used as the standard material to determine the instrumental line broadening.

V.2.3 Reactor packing

To assemble the MFEC material, calcined catalyst particles were loaded into a sintered fiber matrix. The particles were dispersed on the fiber matrix, and were subsequently entrapped inside the inter-locked network of fibers. Circular disks were punched to be 106% of the inner diameter of the reactor tubes. A 1.6mm hole was made at the center of the disks, another 1.6mm hole was made at a distance of 15.4mm from the center. These holes were used to insert multipoint thermocouples. The MFEC discs entrapped with the Co/Al_2O_3 catalyst particles were then stacked into the reactor. For the packed bed, the calcined catalyst particles were

packed inside the reactor directly with quartz wool at both ends. The packed bed was diluted to the same catalyst density as the MFEC (catalyst 30vol.%, copper 7.4vol.%, void 62.6vol.%) with fresh alumina of the same size (149-177μm).

V.2.4 FTS reaction

After in situ reduction of the catalyst, the catalyst beds were cooled to the desired temperature and syngas with a H_2/CO ratio of 2:1 was fed to the reactor at 20bar. The outlet stream from the FTS reactors went sequentially to a hot trap and a cold trap. The residual gas after the cold trap was introduced to an on-line GC (Agilent 6890) with a packed column (Hayesep-DB 100/120). A TCD detector enabled the analysis of CO, CO_2 and C_1-C_6 concentrations with nitrogen used as the internal standard. In the same GC, there was also a capillary column (DB-5) with a flame ionization detector (FID) which was used for the analysis of liquid compounds (C_6-C_{28}) and trace concentrations of uncondensed C_5-C_{10} in the residual gas. Mass balance results were typically +8.9% deviation on carbon and -4.6% deviation on oxygen. The chain growth probability factor (α) was then regressed from the product distribution, as shown in Figure V-6.

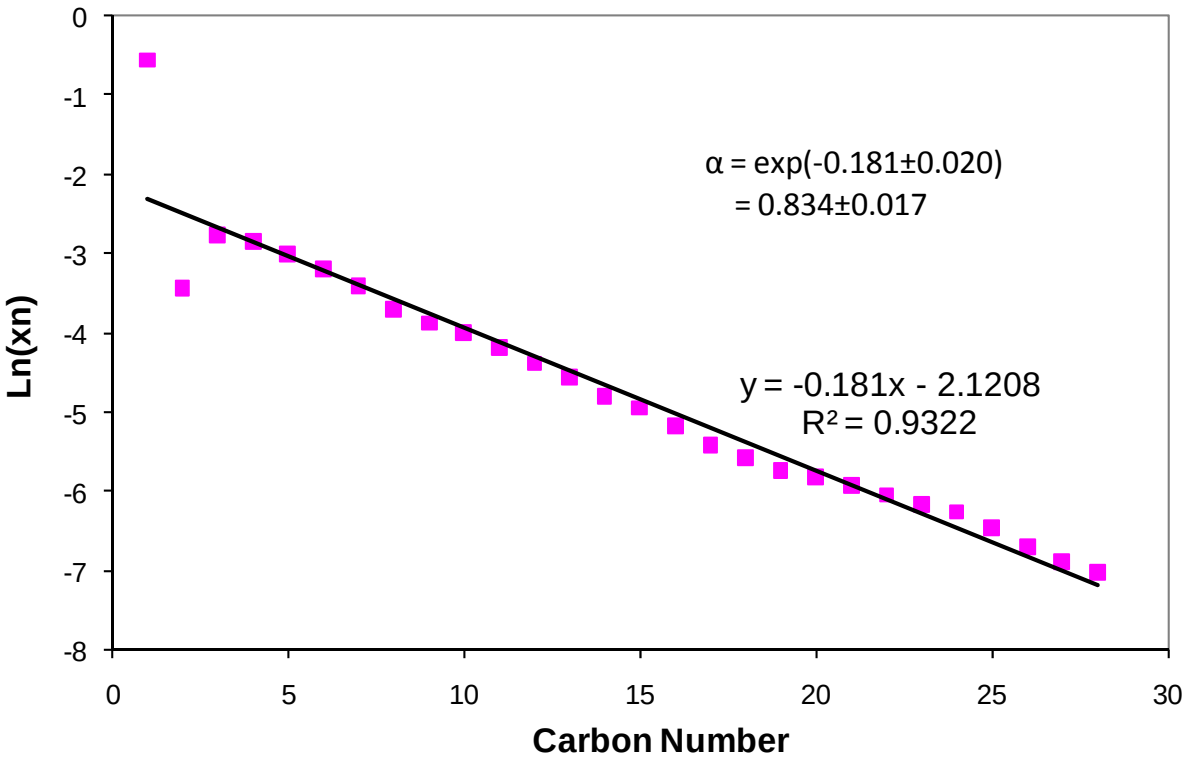

Figure V-6. The determination of the chain growth probability factor (α) according to ASF model

V.3 Results and discussion

V.3.1 Catalyst Characterization

The ICP–AES results showed that the cobalt loading on Co/Al_2O_3 was 14.2%. The total surface area of the fresh alumina was determined by N_2 adsorption-desorption isotherms, as listed in Table V.2. TPR showed that the percentage of the reducible cobalt in the catalyst was

56.4%. The crystallite sizes of Co_3O_4 in the calcined catalyst and cobalt metal dispersion after reduction were estimated using XRD and H_2 chemisorption, respectively.

Table V.2 Characterization results

	Surface area m^2/g	Pore volume cm^3/g	Averge pore diameter nm
Techniques	BET	Incipient impregnation	BET
Fresh Al_2O_3	246	1.04	13.8
	Reduction %	Crystal size of Co^0 /nm	Crystal size of Co_3O_4 /nm
Techniques	TPR	H_2 chemisorption	XRD
15% Co/Al_2O_3	56.4	9.1	13.8

V.3.2 Metal selection for the fiber of MFEC

Stainless steel (SS), nickel and copper fibers (IntraMicron, Auburn AL) were tested for use in the MFEC structures. A summary of results is shown in Table V.3. All MFECs provided a higher void volume percentage (geometrical void between particles) than a packed bed made of traditional extrudates. The small catalyst particles entrapped inside the MFEC facilitated the intraparticle diffusion of reactants and products, so a high effectiveness factor for the FTS reaction was obtained. However, nickel MFEC was found to have a serious problem due to nickel carbonyl formation, which consumed the nickel fibers (Figure V-7). Furthermore, nickel metal from the decomposition of nickel carbonyl deposited on the surface of downstream tubes and apparatuses. Stainless steel and copper fibers did not provide evidence for carbonyl formation during the course of this investigation (e.g., 6 days at reaction condition). The effective thermal conductivity of SS MFEC did not appear to be high enough to handle the highly exothermic nature of the FTS reaction. Unlike SS and nickel fibers, copper fibers were

stable under FTS conditions and had superior heat transfer properties. The chemical stability of copper fibers under FTS conditions was further confirmed by ICP-AES tests, showing that the copper contents in both the oil phase and the water phase from the FTS products generated by copper MFEC were below the detection limit (<0.1ppm). There was no other indication of copper migration within the system, and post-reacted copper MFEC was in good condition. Therefore, copper fibers were chosen to prepare the MFEC structures for the evaluation in FTS.

Figure V-7. Spent SS, Cu, and Ni MFEC structures. SS and Cu fibers were stable, Ni fibers showed significant deterioration

Table V.3 Comparison of different MFECs with Packed bed

	Void	Effectiveness factor[a] for particle size	Thermal conductivity[b] W/m-K	Stability
Packed Bed 1	0.36	0.13 for 4.8mm	0.16	good
Packed Bed 2	0.36	0.87 for 162μm	0.16	good
SS MFEC	0.76	0.87 for 162μm	1.09	good
Ni MFEC	0.77	0.87 for 162μm	3.77	bad
Cu MFEC	0.63	0.87 for 162μm	9.05	good

Note: a, effectiveness factors were obtained using the experimentally determined kinetics with n^{th} order reaction [140],
b, data from [111].

V.3.3 Overall Heat Transfer Coefficient Calculation

In order to examine the heat transfer characteristics of MFEC, the overall heat transfer coefficient (U) of copper MFEC was compared with that of an alumina packed bed. The overall heat transfer coefficient is given by Dixon's equation [137]:

$$\frac{1}{U} = \frac{1}{h_w} + \frac{r_t}{3k_{er}} \frac{Bi+3}{Bi+4} \tag{V-5}$$

The radial effective thermal conductivity (k_{er}) and the inside wall heat transfer coefficient (h_w) were experimentally determined in nitrogen gas. As shown in Figure V-8, the overall heat transfer coefficient of the copper MFEC was much higher than that of the alumina packed bed for a tubular reactor up to 127mm in diameter. The overall heat transfer coefficient of the packed bed declined rapidly as the reactor diameter increased. In contrast to the packed bed, the overall heat transfer coefficient of the copper MFEC maintained a relatively high level up to a 127mm ID tubular reactor. It was found that the ratio of the overall heat transfer coefficient of the copper

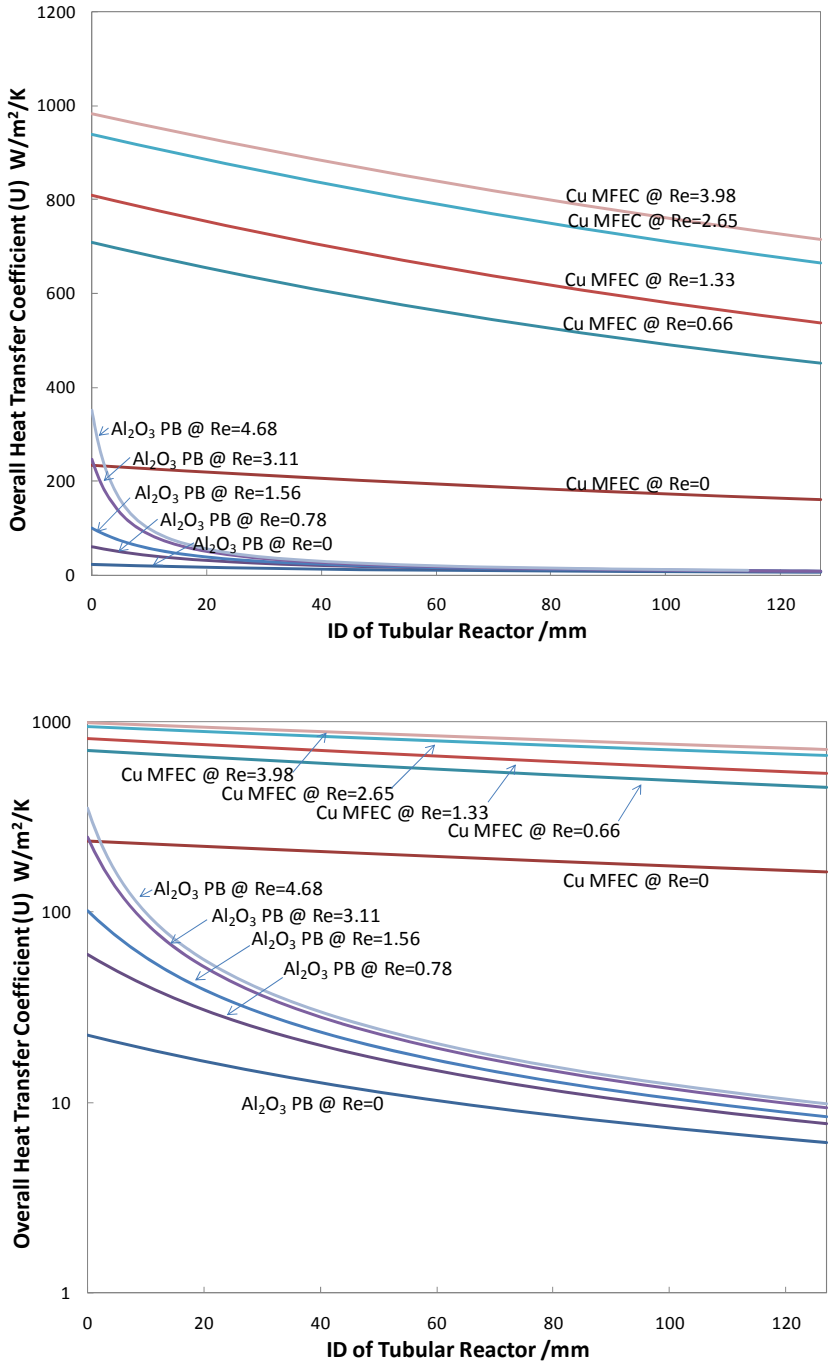

Figure V-8. Overall heat transfer coefficient of alumina packed bed (180-250μm diameter) and copper MFEC (7.4vol.% copper fibers with 12μm diameter, 30vol.% alumina particles with 180-250μm diameter)

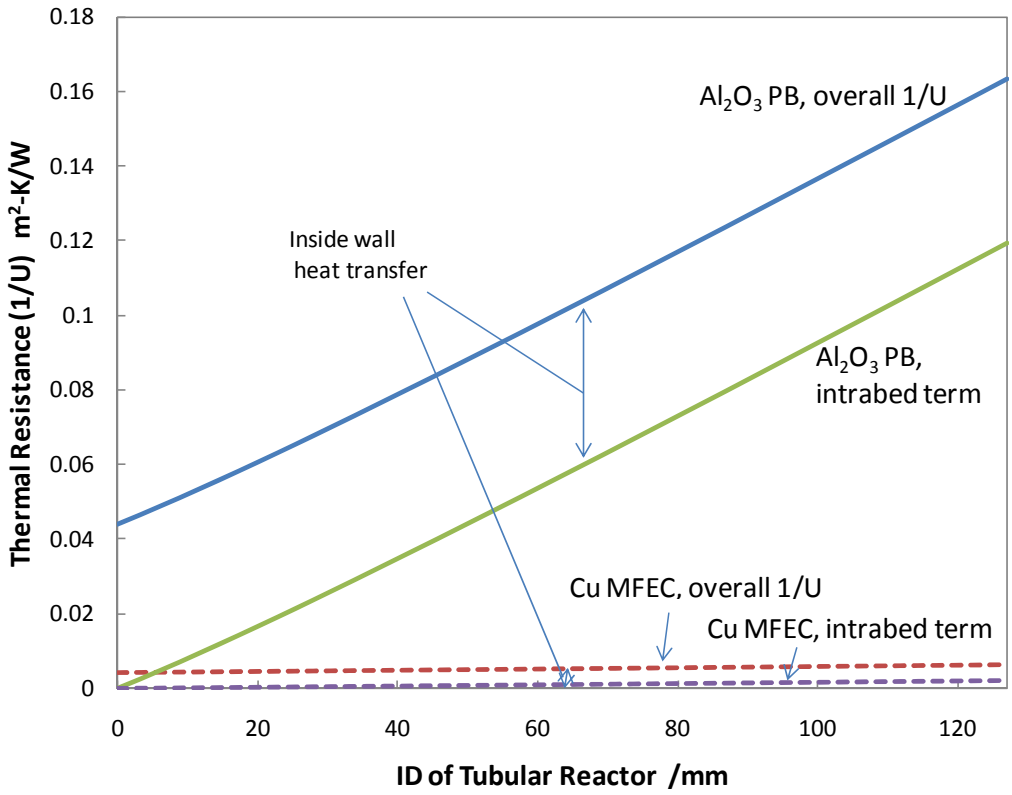

Figure V-9. The thermal resistance of alumina packed bed (180-250µm diameter) and copper MFEC (7.4vol.% copper fibers with 12µm diameter, 30vol.% alumina particles with 180-250µm diameter) with stagnant N_2 gas (Re=0)

MFEC to that of the packed bed in stagnant gas was 15.6:1 for the 15mm ID reactor and 22.3:1 for the 41mm ID reactor. Additionally, the overall heat transfer coefficient for copper MFEC increased considerably with higher gas velocities, but was almost stationary for a packed bed.

The overall thermal resistance (1/U) and the intra-bed thermal resistance are shown in Figure V-9. The thermal resistance from the inside wall heat transfer was assumed to be

constant and the reactor diameter only influenced the intra-bed thermal resistance. For the alumina packed bed, the inside wall thermal resistance term limited the heat transfer in the 15mm ID reactor. However, the intra-bed thermal resistance increased rapidly with increasing reactor diameter and became the major component of the overall thermal resistance. For example, the intra-bed thermal resistance was 73% of the overall value in a 127mm ID tubular packed bed reactor. For copper MFEC, both the inside wall thermal resistance and the intra-bed thermal resistance were much smaller than that of the packed bed. For a 127mm ID tubular copper MFEC reactor, the inner wall thermal resistance still dominated, accounting for 68.8% of the overall thermal resistance. Therefore, efforts to further improve the heat transfer characteristics of copper MFEC should be targeted at reduction of the inside wall thermal resistance.

Due to the absence of the data pertaining to the effective thermal conductivity and the inside wall heat transfer coefficient of these materials under FTS conditions, additional heat transfer analysis of the catalyst beds was done using thermal parameters from measurements with flowing nitrogen. The effective thermal conductivity of the alumina packed bed increased slightly with the gas thermal conductivity. However, this increase is not significant compared to the effective thermal conductivity of copper MFEC (Table V.4). For the MFEC structure, the sintered metal fiber matrix is the primary contribution to the effective thermal conductivity, which is almost independent of the gas. Therefore, the overall heat transfer coefficient shown in Figure V-8 will approximately represent the heat transfer behavior inside FTS reactors.

Table V.4 Effective thermal conductivity of Al_2O_3 packed bed in different gases

Al_2O_3 packed bed	10~90μm		149~177μm	
Gas	Air	He	N_2	Syngas
k of gas[a] W/m-K	0.025	0.15	0.026	0.104
k_e of packed bed[b] W/m-K	0.114	0.18	0.16	0.201[c]

Note: a, data from [140]
b, data from [111] and [141]
c, estimated from Eq. V-6

$$\frac{k_{e1\ in\ gas\ 1} - k_{e1\ in\ gas\ 2}}{k_{gas\ 1} - k_{gas\ 2}} = \frac{k_{e2\ in\ gas\ 3} - k_{e2\ in\ gas\ 4}}{k_{gas\ 3} - k_{gas\ 4}} \tag{V-6}$$

Equation (6) was developed in order to estimate the effective thermal conductivity of a packed bed with gas in it. The slope between the effective thermal conductivity of the packed bed and the thermal conductivity of the gases was assumed to be the same for all particle sizes.

V.3.4 Mears Criterion

From the standpoint of the overall heat transfer coefficient, it is clear that the heat transfer inside an FTS reactor will be significantly improved using copper MFEC. Evaluation of the thermal severity in an FTS fixed bed was estimated by the Mears criterion (M.C.) [142,143]. This criterion was obtained by comparing the heat generation of the reaction with the ability of the catalyst bed to transfer heat away from the reaction zone toward the reactor wall. The M.C. is given in the following equation:

$$M.C. = R_{FTS} \cdot |\Delta H| \cdot \frac{E_a \cdot r_t^2}{R \cdot k_{er} T_w^2} \left(1 + \frac{4k_{er}}{U \cdot r_t}\right) \leq 0.4 \tag{V-7}$$

Table V.5 The overall heat transfer coefficients and Mears criterions

	15mm ID reactor		41mm ID reactor	
	Packed bed[a]	Cu MFEC	Packed bed[a]	Cu MFEC
GHSV (h^{-1})	5000	5000	2750	2750
Re	0.526	0.353	0.362	0.243
U (W/m^2-K)	29.6	461.1	15.8	352.9
Reaction Rate[b] mol of CO/mol of cobalt/s	0.0014	0.0014	0.0047	0.0047
M.C.	5.8	0.3	113.1	4.0

Note: a, Packed bed was diluted with inert alumina to same catalyst volumetric loading as copper MFEC (i.e., catalyst 30vol.%);

b, Reaction rate used for the calculation of M.C., reaction rate at 225°C wall temperature for the 15mm ID reactor and 245°C wall temperature for the 41mm ID reactor.

The radial temperature profile through the catalyst bed is nearly uniform when this criterion is fulfilled (i.e., $M.C. \leq 0.4$). As the M.C. value increases, a higher temperature deviation through the catalyst bed is expected. The M.C. values of a diluted packed bed and copper MFEC in both the 15 and 41mm ID reactors were determined based on the experimental conditions shown in Table V.5. The activation energy of this catalyst was estimated to be 63kJ/mol based on micro-reactor studies. In this study, the Reynolds number (Re) is determined by:

$$Re = \frac{\rho v D_p}{\mu(1-\varepsilon)} \quad \text{(V-8)},$$

where D_p is the equivalent diameter of the sample, given by

$$\frac{1}{D_p} = \frac{S_p}{6V_p} = \sum \frac{y_i}{\varphi_i D_i} \quad \text{(V-9)}$$

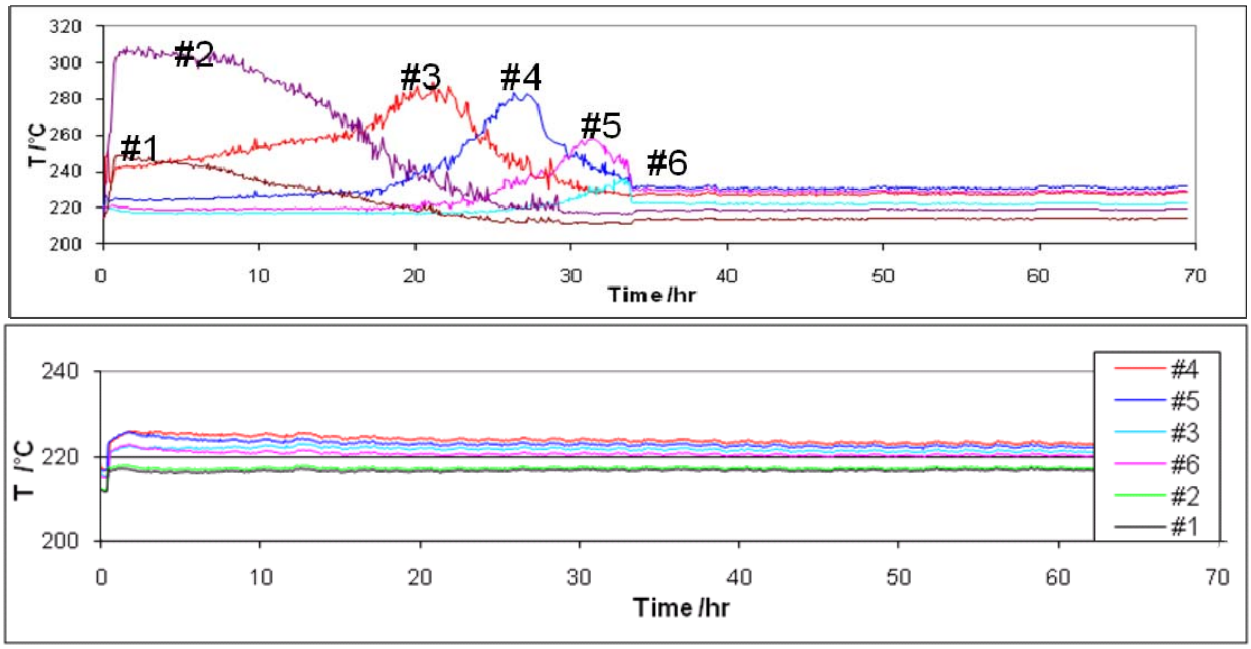

Figure V-10. Temperature profiles of the packed bed (upper, undiluted) and the copper MFEC during the startup; Locations of thermocouple No 1 to 6 shown in Figure V-2; Co/Al_2O_3 catalyst loading, 64vol.% for packed bed, 30vol.% for MFEC

V.3.5 Startup of the 15mm ID reactor

For the startup study, a packed bed made of catalyst particulates without inert alumina dilution was compared with copper MFEC. After in situ reduction and cooling to 225°C, syngas was fed to the catalyst bed at a gas hourly space velocity (GHSV) of 5000/h. The temperature profile at the centerline of the catalyst bed was recorded every 5min for 6 days and CO conversion was analyzed by the online GC every 2h. As shown in Figure V-10, the temperature profiles at the centerline of the packed beds and the copper MFEC were quite different. In the packed bed, a hot spot of about 80°C appeared at the beginning of the startup

and then moved downstream and decreased over time, perhaps due to catalyst conditioning and catalyst deactivation. It took a total of 1.5 days to reach a steady temperature distribution in the packed bed. However, for the copper MFEC, no hot spot developed during the startup period and a steady temperature distribution was reached almost immediately.

V.3.6 Deactivation of the Catalyst

During the startup period for the packed bed, the catalyst activity and product selectivity were found to be strongly dependent on the temperature profile. If a hot spot existed, the catalyst activity (CO conversion) was high (Figure V-11). This behavior constituted a thermal runaway that caused most of the CO to be converted to methane. When the hot spot attenuated and a steady state was reached in the packed bed, the specific catalyst activity (mol of CO/mol of Cobalt/s) declined to about 1/3 of that of copper MFEC. Copper MFEC maintained a relatively stable catalyst activity through the entire 6 day run. Besides the obvious steady state benefit, copper MFEC demonstrated the ability to dampen thermal excursions which occur during startup and other transients.

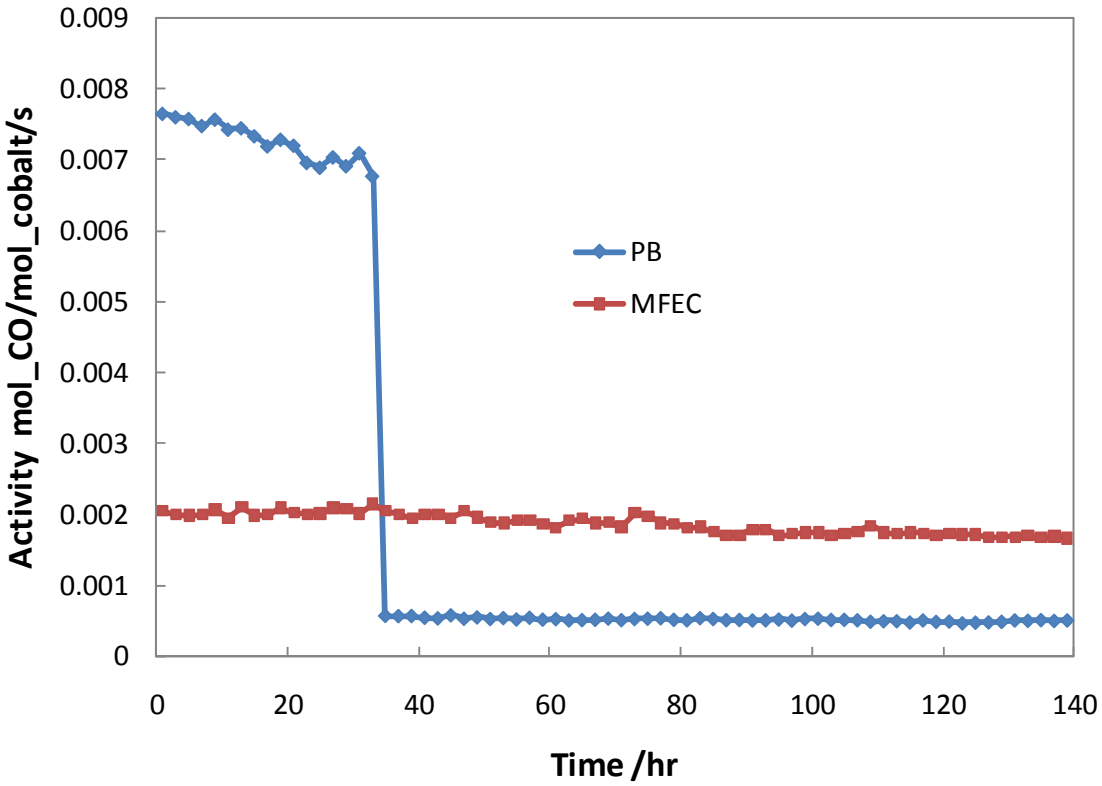

Figure V-11. Catalyst activity in the packed bed (upper, undiluted) and the copper MFEC during the startup; Co/Al_2O_3 catalyst loading, 64vol.% for packed bed, 30vol.% for MFEC

The severe reduction of the catalyst activity in the packed bed resulted from deactivation of the catalyst. This was due to the high temperature of the hot spot in the moving runaway zones. High temperature usually accelerates re-oxidation, carbon deposition, and sintering of cobalt crystallites. As a consequence, this resulted in a rapid deactivation of the catalyst. The re-oxidation of active cobalt sites was verified by XRD. The XRD patterns of fresh alumina, calcined catalysts, and spent catalysts from the packed bed and copper MFEC

are presented in Figure V-12. All samples showed the reflection peaks of γ-alumina at: 2θ=45.9° and 66.9°. The characteristic peaks of the

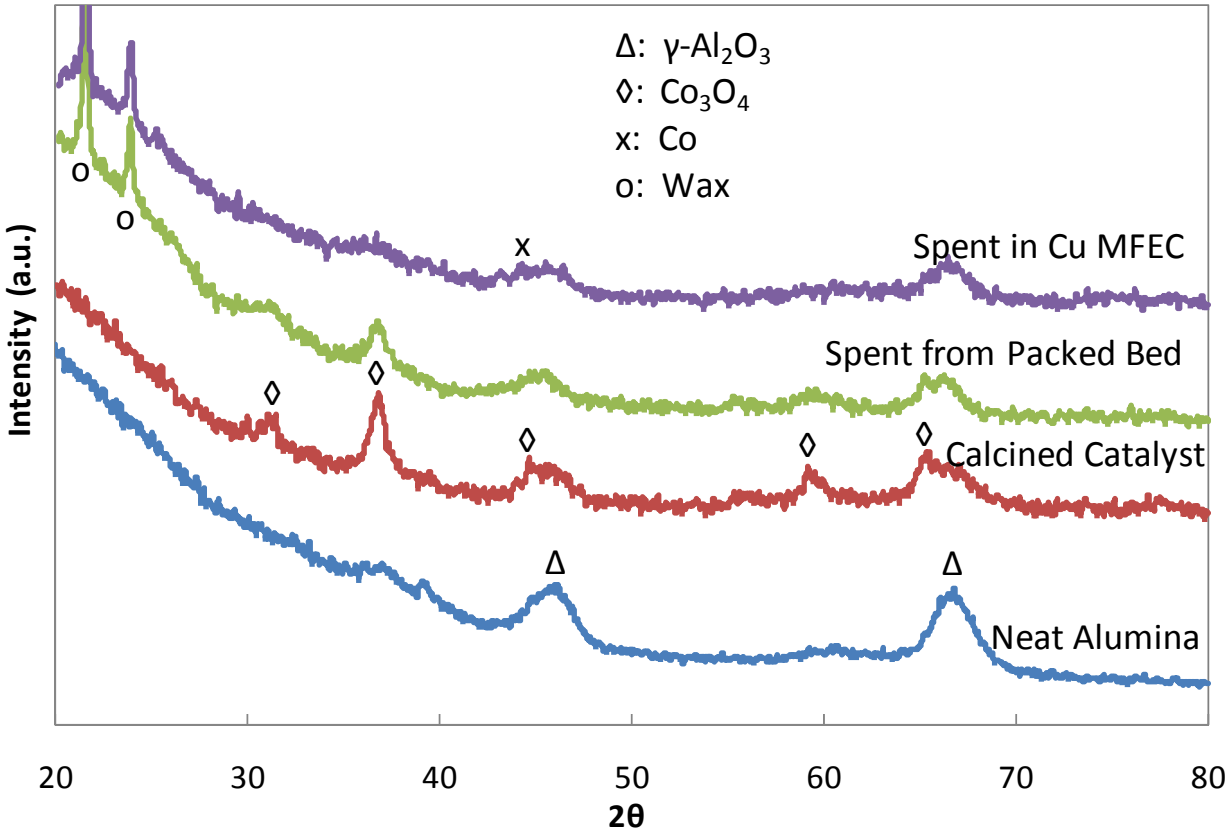

Figure V-12. XRD patterns of calcined catalyst and spent catalysts from FTS

spinel-type Co_3O_4 were observed in the reflection peaks at: 2θ=31.3°, 36.9°, 45°, 59.4° and 65.4°, and the peak for cobalt metal was at 2θ=44.2°. The spent catalysts also showed sharp reflection peaks of heavy wax at: 2θ=21.6° and 23.8°[144]. Peaks for Co_3O_4 were observed in the pattern of spent catalyst from the packed bed, but they were not significant in the spent catalyst from the copper MFEC. With the protection of heavy wax wrapping the spent catalyst and isolating cobalt metal from rapid air exposure during handling, the Co_3O_4 in the catalyst

from the packed bed was attributed to deactivation caused by the hot spot and the high level of CO_2 and H_2O present in the runaway zone. Compared to the packed bed, the spent catalyst from the copper MFEC showed less re-oxidation and maintained much more stable catalyst activity.

V.3.7 Performance in the 15mm ID Reactor at Equivalent Catalyst Loadings

According to the volume percentage of catalyst particles in copper MFEC, the packed bed was diluted with inert alumina to the same catalyst density as the MFEC. Fischer-Tropsch synthesis was carried out using both the diluted packed bed and the copper MFEC structure. The experiments started from the lowest wall temperature of 225°C, and were sequentially collected at 235°C, 245°C, 255°C and, 235°C, one day at each wall temperature. The 235°C temperature run was repeated to determine any change in activity that occurred while operating at the higher temperatures. The ratio of the overall heat transfer coefficient for the copper MFEC to that of the packed bed in this reactor was 15.6:1 and the ratio of the M.C. value was 1:19.3 (Table V.5). As shown in Figure V-13, the maximum temperature deviation from the centerline to the reactor wall was always higher in the packed bed than in copper MFEC. At a wall temperature of 225°C, a temperature deviation of 5.7°C through the packed bed was observed but a nearly uniform temperature profile existed through the copper MFEC. It was also noticed that the maximum temperature deviation increased much faster with imposed increases in the wall temperature for the packed bed than for the copper MFEC. This resulted from the combination of higher CO conversion at higher temperatures and poor heat transfer characteristics of the packed bed. A hot spot developed in the packed bed when the wall

temperature approached 255°C. After running the wall temperature at 255°C for a day, the diluted packed bed encountered a significant drop in CO conversion for the run at 235°C on the next day (solid triangle separated in Figure V-14) compared with the initial run at 235°C. This suggested that catalyst deactivation occurred in the diluted packed bed when the hot spot developed. Alternatively, the CO conversion in the copper MFEC maintained almost the same value for both runs at 235°C (solid circle separated in Figure V-14, overlapping at 235°C), which implied that the copper MFEC provided better thermal stability and catalyst activity maintenance during this evaluation.

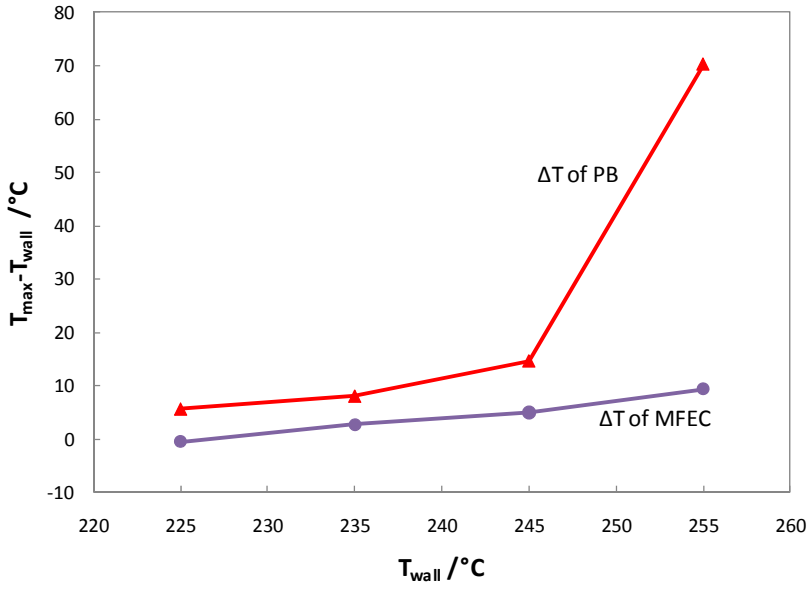

Figure V-13. Maximum temperature deviation for the diluted packed bed (Co/Al_2O_3 30vol.%, Neat Al_2O_3 34vol.%) and the copper MFEC (copper fibers 7.4vol.%, Co/Al_2O_3 30vol.%) in the 15mm ID reactor, 20bar, H_2/CO ratio of 2 and 5000/h GHSV

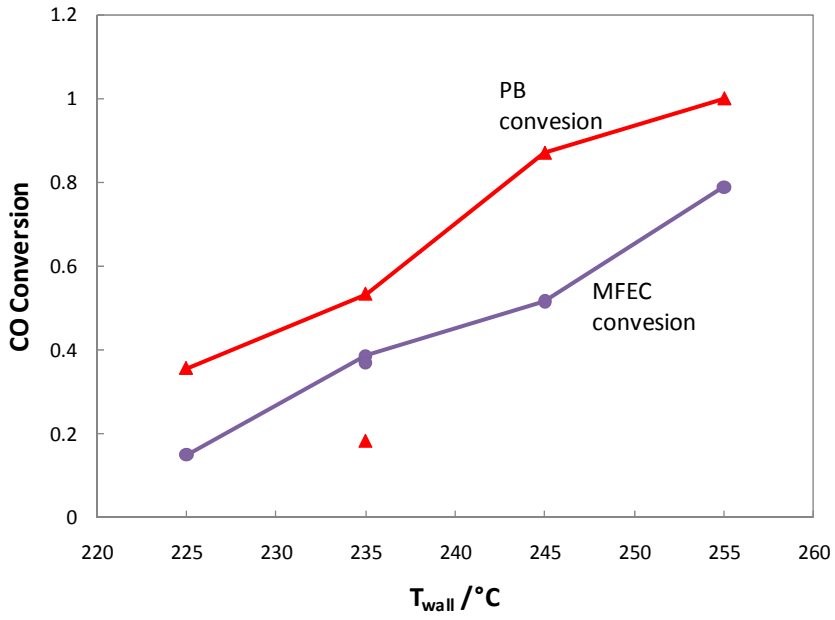

Figure V-14. CO conversion for the diluted packed bed (Co/Al_2O_3 30vol.%, Neat Al_2O_3 34vol.%) and the copper MFEC (copper fibers 7.4vol.%, Co/Al_2O_3 30vol.%) in the 15mm ID reactor, 20bar, H_2/CO ratio of 2 and 5000/h GHSV

The enhanced heat transfer capabilities of copper MFEC avoided the hot spot and enabled a uniform temperature profile inside the catalyst bed. Since the product selectivity of FTS strongly depends on the temperature of the active sites, the uniform temperature profile in turn provided higher selectivity to desired products. The α values and methane selectivity of the 15mm ID packed bed and copper MFEC are shown in Figure II-12. For the packed bed, the hot spot existing at 255°C caused 100% CO conversion, primarily to methane.

V.3.8 Performance in the 41mm ID Reactor

When the diameter of the reactor tube was increased, the overall thermal resistance of the packed bed increased considerably. Additionally, a larger reactor has a higher level of catalyst loading and heat generation, but a smaller surface to volume ratio. These characteristics introduce challenges for heat removal from packed catalyst beds. Consequently, a catalyst structure with enhanced heat transfer characteristics is necessary for safe operation of FTS in larger reactors at high volumetric reaction rates. Compared to the packed bed, the overall thermal resistance of the copper MFEC increased only slightly with the increase in the diameter of the reactor tube. This in turn meant that the overall heat transfer coefficient was still high in the 41mm ID reactor. The ratio of the overall heat transfer coefficient for the copper MFEC to that of the packed bed was 22.3:1 and the ratio of the M.C. value was 1:28.3 (Table V.5).

The diluted packed bed and MFEC bed were compared again in the following sequence of experiments. After the catalyst was reduced in situ and cooled to 210°C, syngas was introduced. All the external heating tapes were then turned off in the packed bed tests. The packed bed reactor exhibited autothermal ignition. The temperature profiles at the centerline and 3/4 of the radius are presented in Figure V-15. Due to the poor overall heat transfer characteristics of the packed bed

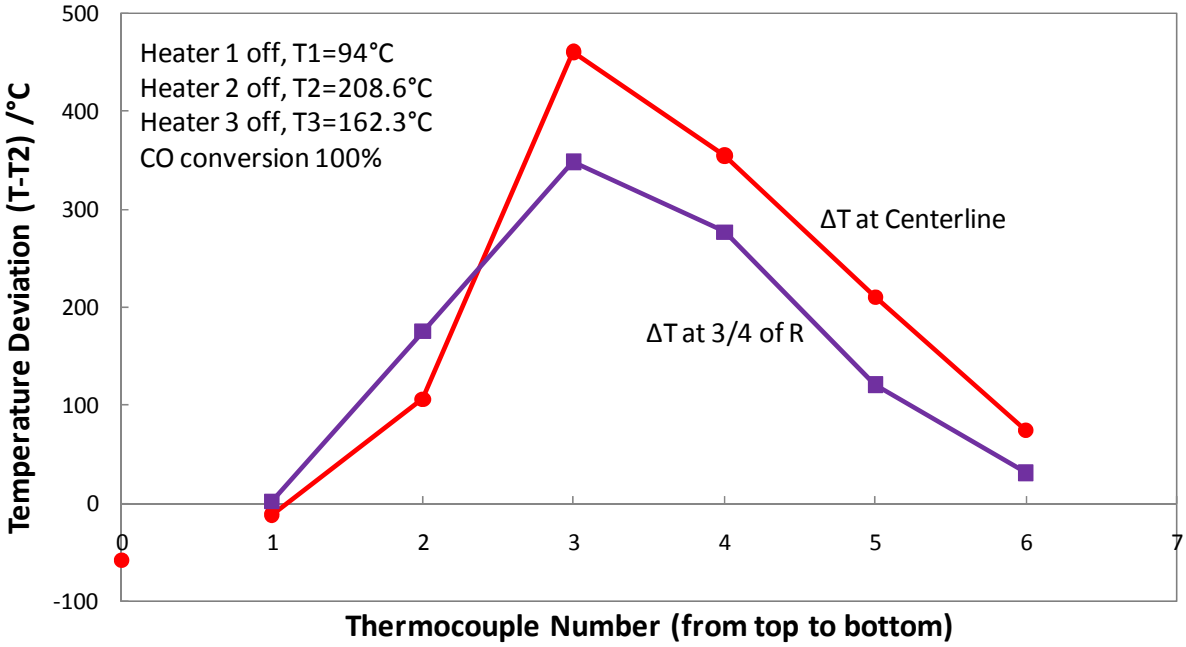

Figure V-15. Temperature profiles inside the packed bed (Co/Al_2O_3 30vol.%, Neat Al_2O_3 34vol.%) of the 41mm ID reactor, 20bar, H_2/CO ratio of 2 and 2750/h GHSV

structure, a very large temperature deviation developed in the radial direction. The high temperature accelerated the reaction and subsequently generated more heat until most of the reactants were consumed. The maximum centerline temperature reached 669°C inside the packed bed, with a temperature deviation of 460°C from the wall. This indicated a runaway state inside the catalyst bed. The CO conversion was 100% with most of the CO converted to methane and CO_2 through the methanation and water-gas-shift reactions, with only 3% converted to other hydrocarbons. The overall stoichiometry was:

$$CO + 2\,H_2 = 0.72\,CH_4 + 0.25\,CO_2 + \frac{0.03}{n}C_nH_{2n+2} + 0.5\,H_2O \quad (n \geq 2) \qquad \text{(V-10)}$$

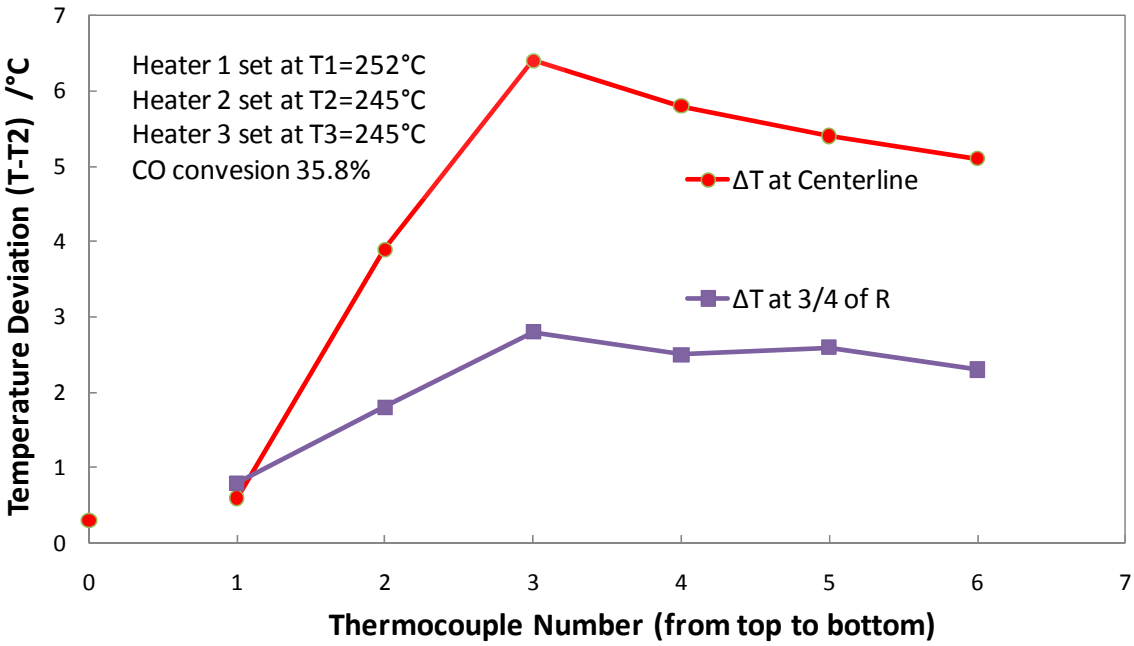

Figure V-16. Temperature profiles inside the catalyst bed of copper MFEC (copper fibers 7.4vol.%, Co/Al_2O_3 30vol.%) in the 41mm ID reactor, 20bar, H_2/CO ratio of 2 and 2750/h GHSV; Locations of thermocouples shown in Figure V-3

Copper MFEC provided a significant improvement in thermal stability compared with the diluted packed bed at the same catalyst volumetric loading and equivalent reaction conditions. Even with all external heating tapes on, the temperature profiles at the centerline and 3/4 of the radius in copper MFEC were much more uniform, as displayed in Figure V-16. The wall temperatures were set to be 252°C for heater 1, and 245°C for heaters 2 and 3. The temperature of the preheating section (heater 1) needed to be higher to ensure the gas heated up slightly above 245°C (No.0 in Figure V-5) before it entered the catalyst bed. Then, all the reaction heat contributed to the temperature increase of the catalyst bed from the wall

temperature. The maximum temperature at the centerline was 251.4°C with a 6.4°C deviation from the wall temperature, and the CO conversion was 35.8%. As shown in Figure V-17, the α values of copper MFEC at different wall temperature were also much higher, compared to that of the packed bed and were confirmed by Song's equation [54]. The uniform temperature profile inside the catalyst bed and the high α values suggest that copper MFEC can effectively remove heat from the reactor and avoid the hot spots that are possible during FTS operations.

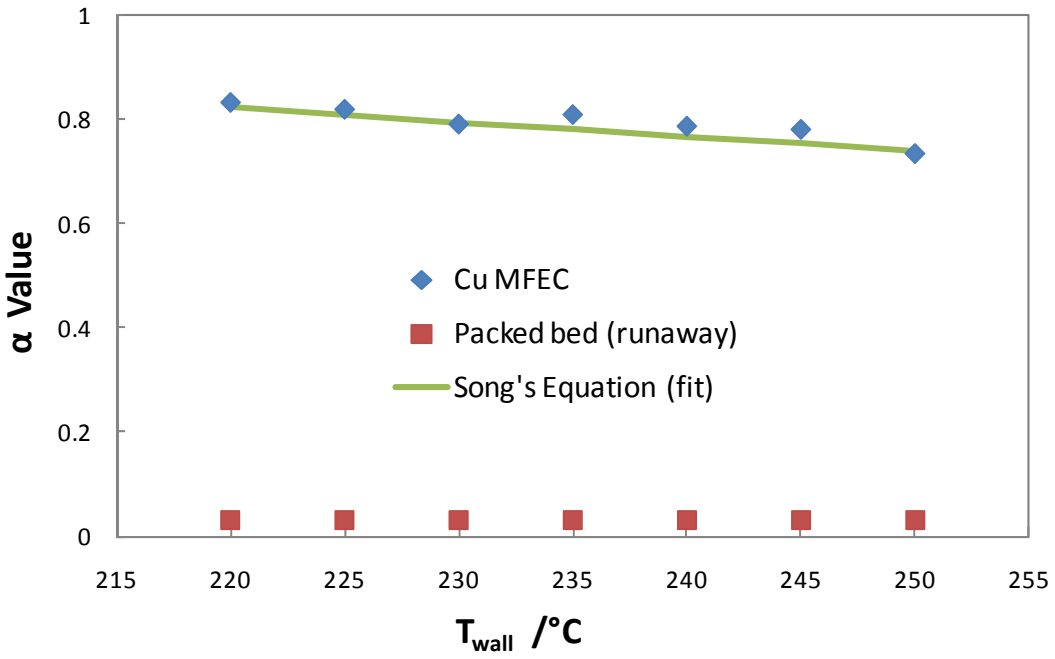

Figure V-17. The chain growth probability factor vs. reactor wall temperature for packed bed and copper MFEC in the 41mm ID reactor

V.4 Conclusions

The enhanced heat transfer characteristics of MFEC structures compared to those of a packed bed were demonstrated by comparing temperature profiles established within FTS reactors operated at equivalent particle size, catalyst loading, conversion and volumetric reactivity. In a 41mm ID reactor, the maximum temperature deviation from the centerline to the reactor wall was only 6.4°C for the copper MFEC, and 460°C for the packed bed. The uniform temperature profiles of copper MFEC resulted in higher selectivity to longer chain hydrocarbons and less catalyst deactivation. The use of copper MFEC avoided hot spot formation during startup, prevented thermal runaway, provided a wider operational temperature range and offered a possibility of using larger diameter reactors.

The utilization of small catalyst particulates within MFEC enhanced both the internal and external mass transfer rates thereby increasing the effectiveness factor. In the absence of other methodologies such as catalyst dilution, high GHSV to promote wash out of hot spots and alternative contacting schemes or reactor types; MFEC provides a unique means to achieve high volumetric reactivity and high conversion in a simple fixed bed arrangement in the absence of excessive pressure drop or high gas recycle and downstream separation requirements.

Acknowledgements:

This work was supported by US Navy under a U.S. Navy contract at Auburn University (N00014-09-C-0208) administered through the Office of Naval Research. The authors want to thank IntraMicron (Auburn AL, US) for technical support.

Chapter VI: Conclusions and Recommendations for Future Work

VI.1 Conclusions

Conclusions for the work on the enhanced heat transfer characteristics of MFEC and the application of MFEC in Fischer-Tropsch Synthesis are presented at the end of the chapters (II-VI). An overview of all research activities conducted will be listed here. This study has led to the experimental determination of thermal parameters of novel catalyst materials, prediction model for the thermal conductivity, heat transfer behavior on micro scale, and the application of them in FTS process. Some of the notable achievements of this work are listed below:

1) Thermal parameters of Cu, Ni, and stainless steel MFEC were experimentally determined in both stagnant nitrogen gas and steady state nitrogen flow.
2) In stagnant nitrogen gas, the radial effective thermal conductivity of copper MFEC was 56-fold of that of alumina PB in a stagnant gas, while the inside wall heat transfer coefficient was 10 times that of alumina PB.
3) With the same volumetric loading of copper, or even higher in PB, the radial effective thermal conductivity of Cu MFEC was much greater than that of PB.
4) The axial effective thermal conductivity of MFEC was much lower than the radial effective thermal conductivity.

5) The flowing gas greatly increases the radial effective thermal conductivity of copper MFEC.
6) A practical model taking the junction factor of fibers into account was proposed to predict the radial effective thermal conductivity of MFM or MFEC
7) The junction factor can be easily determined by measuring the material's electrical resistance. So this model provides a feasible method to determine the thermal conductivity of MFM.
8) The high sintering temperature and the longer sintering time improved the junction factor and the effective thermal conductivity of MFM.
9) The effects of additional copper being loaded onto Cu MFM were evaluated by electroplating and the impregnation method.
10) The temperature distributions of the packed bed and the MFEC in a micro scale were demonstrated by CFD results.
11) CFD approach was utilized to estimate the thermal resistance of the gas in micro gaps in the resistance network model.
12) In the MFEC structure, it was found that 97.2% of the total heat flux was transported by the continuous fiber cylinders.
13) It was suggested that the continuous metal fibers were the primary conduction path for the heat transfer inside the MFEC. This was the fundamental function of fibers on improving the thermal conductivity in a stagnant gas or flowing gas with a low Reynolds number.

14) In flowing gas cases, the temperature distribution directly illustrated the enhanced heat transfer characteristic of the MFEC. The combination of a high heat transfer capacity along the continuous fibers and a large geometric surface area from using small fiber diameters resulted in a rapid increase of effective thermal conductivity of MFEC with gas velocity.
15) The overall heat transfer coefficient of copper MFEC in a tubular reactor was much higher than that of packed bed.
16) In the application of FTS process, the enhanced heat transfer characteristic of copper MFEC significantly reduced the temperature deviation between the centerline of the catalyst bed and the reactor wall.
17) The hot spot and runaway state in the packed bed were entirely prevented in the copper MFEC.
18) Compared to the packed bed in FTS, a high selectivity of heavy products of FTS was achieved by utilizing copper MFEC, and the rapid deactivation of the catalyst was also inhibited.
19) The combination of the enhanced heat transfer characteristic of the microfibrous matrix and the small internal mass transfer resistance in the copper MFEC demonstrated a wider operation temperature range, a possibility to use larger size reactors, a high reaction effectiveness factor, a high thermal stability and a high selectivity for heavy products in FTS process.

It was shown that the conductive metal MFEC, especially copper MFEC, has an excellent ability to serve as a catalyst carrier with an enhanced heat transfer characteristic for use with highly exothermic and highly endothermic reactions/processes.

VI.2 Recommendations for Future Work

VI.2.1 Catalyst characterization of the spent catalyst of FTS process

The high temperature of the hot spot in packed bed led a rapid deactivation of the catalyst. The XRD spectra showed the re-oxidation of the cobalt active sites is one of the mechanisms. Other possible mechanisms that cause the huge decrease of the catalyst activity in packed bed are still needed to be verified. TEM, XPS and Oxygen titration techniques would be able to do that.

VI.2.2 Improvement of the inside wall heat transfer

The CFD simulation results (Figure IV.13 and 14) and the overall thermal resistance of copper MFEC (Figure VI.9) showed that the inside wall heat transfer of the MFEC was the determining term in the overall heat transfer coefficient. Therefore, further effort to improve the heat transfer qualities of the MFEC structure should be focused on reducing the inside wall thermal resistance. For example, pressure applied at the edges of the catalyst bed against the reactor wall can reduce the contact resistance. Melting some metal fins on the inner wall of the reactor also can improve the inside wall heat transfer.

VI.2.3 CFD model with reactions

CFD approach to study the mass transfer and heat transfer of catalyst beds can provide the information from a micro scale to a macro scale. This study showed the heat transfer of packed bed and MFEC in a micro scale, but without any reaction. The CFD model of catalyst bed with chemical reactions should be able to show more information in a micro scale, which can help us to deeply understand the mass transfer and heat transfer properties of the catalyst beds.

VI.2.4 Application of MFEC in other reactions

Most of the results in this study were focused on the heat transfer phenomena of the MFEC structures. Only one application of this materials was investigated to prove the excellent ability to serve as a catalyst carrier with an enhanced heat transfer characteristic. There are hundreds of reactions with the highly exothermic nature and highly endothermic nature, such as Methanol Synthesis, Dimethyl Ether (DME) synthesis, and Steam Reforming. The combination of the enhanced heat transfer characteristic of the microfibrous matrix and the small internal mass transfer resistance of the MFEC should be able to reduce the centerline temperature of the catalyst bed, allow the fine temperature controlling cross the catalyst bed, and enable to scale up the reactors.

References

1. Fischer, F. and Tropsch, H., Hydrocarbons, De: Addn. to 484337 (1925a) C.A. 24, 1119

2. Fischer, F. and Tropsch, H., The synthesis of petroleum at atmospheric pressures from gasification products of coal, Brennstoff-Chemie, 7 (1926c), 97-104

3. Anderson, R.B., In P.H. Emmett(editor), Catalysis, 4 (1956), Reinhold

4. Stranges, A.N., In AICHE 3rd Topical Conference on Natural Gas Utilization, New Orleans, 2004, 635-646

5. Fischer, F. and Pichler, H., Ges. Abh. Kenntn. Kohle 13 (1937), 407

6. Fischer, F. and Pichler, H.,. Brennstoff-Chemie, 20 (1939), 41

7. Dry, M.E., in Anderson, J.R. and Boudart, M.(editors), Catalysis Science and Technology, 1 (1981), Springer, Berlin

8. Dry, M.E., Practical and theoretical aspects of the catalytic Fischer-Tropsch process, Applied Catalysis A, 138 (1996), 319-344

9. Steynberg, A.P. and Dry, M.E., Fischer-Tropsch Technology, Studies in Surface Science and Catalysis, 152 (2004)

10. Kieth, P.C., Gasoline from natural gas, The Oil and Gas Journal, May, 16, 1946

11. Arnold, J.H. and Kieth, P.C., In ACS meeting, Advances in Chemistry, 120 (1951)

12. Groueff, S., Manhattan project: the untold story of the making of the atomic bomb, Little, Brown and Co., Boston, 1967

13. Krishna, R. and Sie, S.T., Design and scale-up of the fischer-tropsch bubble column slurry reactor, Fuel Processing Technology, 64 (2000), 73-105

14. Davis, B.H., Fischer-Tropsch Synthesis: overview of reactor development and future potentialities, Topics in Catalysis, 32 (2005), 143-168

15. Guettel, R., Kunz, U. and Turek, T., Reactors for fischer-tropsch synthesis, Chemical Engineering & Technology, 31 (2008), 746-754

16. Kölbel, H. and Tillmetz, K.D., Model studies of the interaction of carbon monoxide and hydrogen on transition matals: Role of chemisorption complexes in primary reactions, Journal of Catalysis, 34 (1974), 307-316

17. Elbashir, N.O.M., Utilazation of supercritical fluids in the fischer-tropsch synthesis over cobalt-based catalytic systems, PHD dissertation, College of engineering, Auburn University, Auburn, AL, 2004

18. Henrici, G. and Olive, O.S., Angew. Chem., Int. Ed. Engl. 15 (1976), 136

19. Friedel, R.A. and Anderson, R.B., Composition of synthetic liquid fuels, I, product distribution and analysis of C5-C8 paraffin isomers from cobalt catalyst, Journal of American Chemical Society, 72 (1950), 1212-1215

20. Herrington, E.F.G., The Fischer-Tropsch synthesis considered as a polymerization reaction, Chemistry and Industry, London UK, 1946, 346-347

21. Dry, M.E., Catalytic aspects of industrial Fischer-Tropsch synthesis, Journal of Molecular Catalysis, 7 (1982), 133-144

22. Wojciechowski, B.W., Kinetics of Fischer-Tropsch synthesis, Catalysis Reviews, 30 (1988), 629-702

23. Dictor, R.A. and Bell, A.T., Fischer-Tropsch synthesis over reduced and unreduced iron oxide catalysts, Journal of Catalysis, 97 (1986), 121-136

24. Iglesia, E., Reyes, S.C. and Madon, R.J., Transport-enhanced α-olefin readsorption pathways in Ru-catalyzed hydrocarbon synthesis, Journal of Catalysis, 129 (1991), 238-256

25. Komaya, T. and Bell, A.T., Estimates of rate coefficients for elementary process occuring during Fischer-Tropsch synthesis over Ru/TiO2, Journal of Catalysis, 146 (1993), 237-248

26. Kuipers, E.W., Scheper, C., Wilson, J.H., 1996. Vinkenburg, I.H., Oosterbeek, H., Non-ASF product distributions due to secondary reactions during Fischer-Tropsch synthesis, Journal of Catalysis, 158 (1996), 288-300

27. Laan, Van Der and Beenackers, A.A.C.M. Kinetics and selectivity of Fischer-Tropsch synthesis: a literature review, Catal. Rev.-Sci. Eng., 41 (1999), 255-318

28. Kölbel, H. and Ralek, M., The Fischer-Tropsch synthesis in the liquid phase, Catal. Rev.-Sci. Eng., 21 (1980), 255-274

29. Sie, S.T. and krishna, R., Fundamentals and selection of advanced Fischer-Tropsch reactors, Applied Catalysis A, 186 (1999), 55-70

30. Storch, H.H., Golumbic, N. and Anderson, R.B., The Fischer-Tropsch and related synthesis, John wiley & Sons, New York, 1951

31. Kölbel, H., In: Chimie organique, eds. K. Winnacker and L. Küchler, Part 3, Editions Eyrolles, Paris, 1966, 627-740

32. Storch, H.H., Technical paper 642, US Bureau of Mines: Washington, DC, 1942

33. Storch, H.H., The Fischer-Tropsch and related processes for synthesis of hydrocarbons by hydrogenation of carbon monoxide, Advances in Catalysis, 1 (1948), 115-156

34. Ministry of fuel and power, Report on the petroleum and synthetic oil industry of Germany, His Majesty's Stationery Office, London, 1947

35. Sie, S.T., Process development and scale up: Case history of the development of a Fischer-Tropsch synthesis process, Reviews in Chemical Engineering, 14 (1998), 109-157

36. Hoogendoorn, J.C. and Salomon, J.M., Sasol: World's Largest Oil-from-coal Plant, British chem. Eng. 1957, 238

37. Dry, M.E. and Erasmus, H.B.W., Update of the sasol synfuels process, Annu. Rev. Energy, 12 (1987), 1-12

38. Schulz, H., Short history and present trends of Fischer-Tropsch synthesis, Applied Catalysis A, 186 (1999), 3-12

39. Van Vuuren, D.S., Fischer-Tropsch synthesis in slurry reactors: summary and analysis of the state of the art, CSIR CENG 1982, 432

40. Hoogendoorn, J. C., Gas from coal with Lurgi gasification at Sasol. In: clean Fuels from Coal. Institute of Gas Technology Symposium, Chicago, 1973, September 10-14, 353

41. Duvenhage, D.J. and Singles, T., Synthol reactor technology development, Catalysis Today, 71 (2002), 301-305

42. Krishna, R. and van Baten, J.M., A strategy for scaling up the Fischer Tropsch bubble column slurry reactor, Topics in Catalysis, 26 (2003), 21-28

43. Espinoza, R.L., Steynberg, A.P., Jager, B. and Vosloo, A.C., Low temperature Fischer-Tropsch synthesis from a sasol perspective, Applied Catalysis A, 186 (1999), 13-26

44. Yokota, L. F.K. and Fujimoto, K., Characterization of mass transfer in supercritical phase Fischer–Tropsch synthesis reaction, Topics in Catalysis 2 (1995), 267–283

45. Abbaslou,R.M.M., Mohammadzadeh, J.S.S., Dalai, A.K., Review on Fischer–Tropsch synthesis in supercritical media, Fuel Processing Technology, 90 (2009), 849-856

46. Huang, X. and Roberts, C.B., Selective Fischer–Tropsch synthesis over an Al2O3 supported cobalt catalyst in supercritical hexane, Fuel Processing Technology 83 (2003), 81– 99

47. Hilmen, A.M., Bergene, E., Lindvag, O.A., Schanke, D., Eri, S., Holmen, A., Fischer-Tropsch synthesis on monolithic catalysts of different materials, Catalysis Today, 69 (2001), 227-232

48. Deugd, R.M., Kapteijin, F., Moulijin, J.A., Using monolithic catalysts for highly selective Fischer-Tropsch synthesis, Catalysis Today, 79-80 (2003), 495-501

49. Visconti, C.G, Tronconi,E., Lietti, L., Groppi, G., Forzatti, P., Cristiani, C., Zennaro, R., Rossini, S., An experimental investigation of Fischer–Tropsch synthesis over washcoated metallic structured supports, Applied Catalysis A, 370 (2009), 93–101

50. Donnelly, T. J., Satterfield, C. N., Product distributions of the Fischer-Tropsch synthesis on precipitated iron catalysts, Appl. Catal. 52 (1989), 93-114

51. Lox, E. S.; Froment, G. F., Kinetics of the Fischer−Tropsch reaction on a precipitated promoted iron catalyst. 1. Experimental procedure and results, Ind. Eng. Chem. Res. 32 (1993), 61

52. Thompson, G.J., Riekema, M.L., Vickers, A.G., Comparison of Fischer-Tropsch reactor systems, Phase 1: final report, DOE Contract, 1981,UOP: Des Plaines, IL.

53. Yermakova, A. and Anikeev, V.I., Thermodynamic calculations in the modeling of multiphase processes and reactors, Ind. Emg. Chem. Res., 39 (2000), 1453

54. Song, H.S., Ramkrishna, D., trinh, S. and Wright, H., Operatimg strategies for Fischer-Tropsch reactors: a model-directed study, Korean J. Chem. Eng., 21 (2004), 308-317

55. Eliason S.A.; Bartholomew C.H., Reaction and deactivation kinetics for Fischer-Tropsch synthesis on unpromoted and potassium-promoted iron catalysts, Applied Catalysis A, 186 (1999), 229-243

56. Leib, T. B. and Kuo, J. C. W., Modeling the Fischer-Tropsch synthesis in slurry bubble-column reactors, Paper presented at the AIChE Annual Meet., San Francisco, Calif. Nov. 25-30, 1984

57. Rautavuoma, A.O.I., Baan, V.D.H. S., Kinetics and mechanism of the Fischer-Tropsch hydrocarbon synthesis on a cobalt and alumina catalyst, Applied Catalysis, 1 (1981), 247.

58. Steen, E.V. and Schulz, H., Polymerisation kinetics of the Fischer-Tropsch CO hydrogenation using iron and cobalt based catalysts, Applied Catalysis A, 186 (1999), 309-320

59. Atwood, H.E. and Bennett, C.O., Kinetics of the Fischer-Tropsch reaction over Iron, Ind. Eng. Chem. Process Des. Dev., 18 (1979), 163–170

60. Kölbel,H., Die Fischer-Tropsch Synthesis, In winnacker-küchler chemische technologie, vol. 3: Organische Technologie I, Karl Hauser Verlag, Munich, 1959, 439-520

61. Bartholomew, C.H., Mechanisms of catalyst deactivation, Applied Catalysis A, 212 (2001), 17-60

62. Moulijn, J.A., van Diepen, A.E., Kapteijn, F., Catalyst deactivation: is it predictable? - What to do?, Applied Catalysis A, 212 (2001), 3-16

63. Bian, G.Z., Fujishita, N., Mochizuki, T., Ning W.S. and Yamada, M., Investigations on the structural changes of two Co/SiO2 catalysts by performing Fischer–Tropsch synthesis, Applied Catalysis, 252 (2003), 251-260

64. Lee, D.K., Lee, J.H., Ihm, S., Effect of carbon deposits on carbon monoxide hydrogenation over alumina-supported cobalt catalyst, Applied Catalysis, 36, 199-207

65. Saunders, A.O., 1932., Phil. Mag., 13 (1988), 1186

66. Schumann, T.E.W. and Voss, V., Heat flow through granulated material, Fuel. 13 (1934), 249-256

67. Bala, K., Pradhan, P.R., Saxena, N.S. and Saksena, M.P., Effective thermal conductivity of copper powders, J. Phy. D: Appl. Phys. 22 (1989),1068-1072

68. Sharma, C.S. and Hughes, R., The thermal conductivity of porous catalyst compacts, The Camadian Journal of Chemical Engineering, 54 (1976), 358-363

69. Mcelroy, D.L., Weaver, F.J., Longest, A.W. and Yarbrough, D.W., US DOE, 1988, Contract DE-AC05-840R21400

70. Bunnell, D.G., Irvin, H.B., Olson, R.W., Smith, J.M., Effective thermal conductivities in gas-solid systems, Industrial and Engineering Chemistry Research & Development, 41 (1949), 1977-1998

71. Dixon, A.G., Thermal resistance models of packed bed effective heat transfer parameters, AICHE J., 31 (1985), 826

72. Demirel, Y., Sharma, R.N., Al-Ali, H.H., On the effective heat transfer parameters in a packed bed, International Journal of Heat and Mass Transfer, 43 (2000), 327-332

73. Bey, O. and Eigenberger, G., Gas flow and heat transfer through catalyst filled tubes, International Journal of Thermal Sciences, 40 (2001), 152-164

74. Wen, D. and Ding Y., Heat transfer of gas flow through a packed bed, Chemical Engineering Science, 61 (2006), 3532-3542

75. Perry, R.H., Green, D.W., Perry's Chemical Engineers' Handbook, Mcgraw-Hill Companies, 1999

76. Lemmon, E.W. and Jacobsen, R.T., Viscosity and thermal conductivity equations for nitrogen, oxygen, argon and air, International Journal of Thermophysics, 25 (2004), 21-69

77. Philippe, R., Lacroix, M., Dreibine, L., Pham-Huu, C., Edouard, D., Savin, S., Luck, F., Schweich, D., Effect of structure and thermal propertied of a Fischer-Tropsch catalyst in a fixed bed, Catalysis Today, 147S (2009), S305-S312

78. Pangarkar, K., Schildhauer, T.J., et al., Structured packing for multiphase catalytic reactors, Ind. Eng. Chem. Res. 47 (2008), 3720-3751

79. Pangarkar, K., Schildhauer, T.J., et al., Experimental and numerical comparison of structured packings with a randomly packed bed reactor for Fischer-Tropsch synthesis, Catalysis Today, 147s (2009), s2-s9

80. Tronconi, E., Groppi, G., Boger, T., Heibel, A., Monolithic catalysts with high conductivity honeycomb supports for gas/solid exothermic reactions: characterization of the heat-transfer properties, Chem. Eng. Sci., 59 (2004), 4941-4949

81. Giani, L., Groppi, G., Tronconi, E., Mass transfer characterization of metallic foams as supports for structured catalysts, Ind. Eng. Chem. Res., 44 (2005), 4993-5002

82. Scala, C. von, Wehrli, M.G., Heat transfer measurements and simulation of KATAPAK-M catalyst supports, Chem. Eng. Sci. 54 (1999), 1375-1381

83. Tatarchuk, B.J. , M.F. Rose, A. Krishnagopalan, J.N. Zabasajjia, D. Kohler, Mixed fiber composite structure, US Patent 5,096,663, March 17, 1992

84. Tatarchuk, B.J., Rose, M.F., Krishnagopalan, A., Zabasajjia, J.N., Kohler, D., Mixed fiber composite structures high surface area high conductivity mixtures, US Patent 5,304,330, April 19, 1994

85. Murrell, L.L., Dautzenberg, F.M., Overbeek, R.A., Tatarchuk, B.J., Reactor, US Patent 20020068026, June 6, 2002

86. Tatarchuk, B.J., Yang, H., Kalluri, R., Cahela. D.R., Microfibrous entrapped catalysts for optimizing and controlling highly exothermic and highly endothermic reactions, US Patent, Provisional number 12/940792

87. Meffert, M.W., Preparation and characterization of sintered metal microfiber-based composite materials for heterogeneous catalyst application, PHD dissertation, College of engineering, Auburn University, Auburn, AL, 1998

88. Duggirala, R.K., Roy, C.J., Kalluri, R., Yang, H., Cahela, D.R., Tatarchuk, B. J., Computational fluid dynamics simulations of desulfurization using datalytic particles embedded in a matrix of sinter-bonded microfibers, Submitted to Elsevier 7 Jan. 2008

89. Kalluri, R.R., Cahela, D.R., Tatarchuk, B.J., Microfibrous entrapped small particle adsorbents for high efficiency heterogeneous contacting, Separation and Purification Technology, 62(2008), 304–316

90. Yang, H., Cahela, D.R., Tatarchuk, B.J., A study of kinetic effects due to using microfibrous entrapped zinc oxide sorbents for hydrogen sulfide removal, Chemical Engineering Science, 63 (2008), 2707–2716

91. Duggirala, R.K., Roy, C.J., Yang, H., Kalluri, R.R., Cahela, D.R., Tatarchuk, B.J., Simulation of heterogeneous H2S removal in microscale gas flows. In: Abstracts of Papers, 232nd ACS National Meeting, September 2006. 10–14, San Francisco, CA, USA

92. Zhu, W.H., Flanzer, M.E., Tatarchuk, B.J., Nickel–zinc accordion-fold batteries with microfibrous electrodes using a papermaking process, Journal of Power Sources, 112 (2002), 353–366

93. Ryan Sothen, Novel packaging designs for improvements in air filter performance, PHD dissertation, College of engineering, Auburn University, Auburn, AL, 2009

94. Waddams, A.L., The flow of heat through granular materials, Journal of The Society of Chemical Industry, 63 (1944), 337-340

95. Burke, S.P., Schuman, T.E. and Parry, V.F., Fuel, 10, 1931, 249

96. Collier, A.P., Hayhurst, A.N., et al. The heat transfer coefficient between a particle and a bed of much large particles, Chemical Engineering Science, 59 (2004) 4613-4620

97. Laguerre, O., Amara, S.B., Flick, D., Heat transfer between wall and packed bed crossed by low velocity airflow, Applied Thermal Engineering, 26 (2006), 1951-1960

98. Borkink, J.G.H., Westerterp, K.R., Influence of tube and particle diameter on heat transport in packed beds, AIChE Journal, 38 (5), 703-715

99. Moreira, M.F.P., Ferreira, M.C., Freire, J.T., Evaluation of pseudohomogeneous models for heat transfer in packed beds with gas flow and gas-liquid concurrent downflow and upflow, Chemical Engineering Science, 61 (2006), 2056-2068

100. Anderson, J.D., Computational fluid dynamics the basics with applications, McGraw Hill, 1995

101. Bjorck, A., Numerical methods for least squares problems, SIAM, 1996

102. Kozlov, V.A., Toporova, V.V., Powder Metallurgy and Metal Ceramics, V12 (1973), 9-12

103. Mischke, R.A. and Smith, J.M., Ind. Eng. Chem. Fundamen., 1 (1962), 288-292

104. Bala, K., Pradhan, P.R., J. Phys. D: Appl. Phys., 22 (1989), 1068-1072

105. Dixon, A.G., Dongeren, J.H., The influence of the tube and particle diameters at constant ratio on heat transfer in packed bed, Chemical Engineering and Processing, 37 (1998), 23-32

106. Wen, D., Ding, Y., Heat transfer of gas flow through a packed bed, Chemical Engineering Science, 61 (2006), 3532-3542

107. Boger, T., Herbel, A.K., Heat transfer in conductive monolith structures, Chem. Eng. Sci., 60 (2005), 1823-1835

108. Jacobs, G., Ribeiro, M.C., et al., Group 11(Cu, Ag, Au) promotion of 15%Co/Al2O3 Fischer-Tropsch syntheisi catalysts, Applied Catalysis A, 361(2009), 137-151

109. Li, J., Yang, J., Wang, M, Lu, Y., He, M., A microreactor based on sinter-locked microfibrous media with open porous structure for nitration of benzene, Chinese Journal of Catalysis, 28 (2007), 931-933.

110. Tang, Y., Chen, L., Wang, M., Li, J., Lu, Y., Microfibrous entrapped ZnO-CaO/Al_2O_3 for high efficiency hydrogen production via methanol steam reforming, Particuology, 8 (2010) 225-230.

111. Sheng, M., Yang, H., Cahela, D.R., Tatarchuk, B.J., Novel catalyst structures with enhanced heat transfer characteristics, J Catal, 281 (2011), 254-262

112. Lee, J.-S., Yano, T., Fabrication of short-fiber-reinforced SiC composites by polycarbosilane infiltration, J. Eur. Ceram. Soc., 24 (2004), 25-31

113. Dul'new, G.N., and Muratova, B.L., Thermal conductivity of fibrous systems, J. Eng. Phy. 14 (1968), 29-35

114. Mantle, W.J., Chang, W.S., Effective thermal conductivity of sintered metal fibers, Energy Conversion Engineering Conference, Proceedings of the 24 Intersociety, 1989, 1871-1877

115. Bahrami, M., Yovanovich, M.M., Culham, J.R., Effective thermal conductivity of rough spherical packed beds, International Journal of Heat and Mass Transfer, 49 (2006), 3691-3701

116. Slavin, A.J., Londry, F.A., Harrison, J., A new model for the effective thermal conductivity of packed beds of solid spheroids: alumina in helium between 100 and 500˚C, International Journal of Heat and Mass Transfer, 43 (2000), 2059-2073

117. Powell, P.W., Correlation of metallic thermal and electrical conductivities for both solid and liquid phase, Int. J. Heat Mass Transfer 8 (1965), 1033-1045

118. Koh J.C., and Fortini, A., Prediction of thermal conductivity and electrical resistivity of porous metallic materials, Int. J. Heat Mass Transfer, 16 (1973), 2013-2022

119. Calis, H.P.A., Nijenhuis, J., Paikert, B.C., Dautzenberg, F.M., Bleek, C.M., CFD modeling and experimental validation of pressure drop and flow profile in a novel structured catalytic reactor packing, Chemical Engineering Science, 56 (2001), 1712-1720

120. Kolaczkowski, S.T., Chao, R., Awdry, S., and Smith, A., Application of a CFD code(Fluent) to formulate models of catalytic gas phase reactions in porous catalyst pellets, Chemical Engineering Research and Design, 85 (2007), A11, 1539-1552

121. Duran, J.E., Mohseni, M., Taghipour, F., Modeling of annular reactors with surface reaction using computational fuid dynamics(CFD), Chemical Engineering Science, 65 (2010), 1201-1211

122. Derkx, O.R., Dixon, A.G., Determination of the fixed bed wall heat transfer coefficient using computational fluid dynamics, Numerical Heat Transfer Part A 29 (1996), 777

123. Logtenberg, S.A., Dixon, A.G., Computational fluid dynamics studies of fixed bed heat transfer, Chemical Engineering and Processing, 37 (1998), 7-21

124. Logtenberg, S.A., Nijemeisland, M., Dixon, A.G., Computational fluid dynamics simulations of fluid flow and heat transfer at the wall-particle contact points in a fixed bed reactor, Chemical Engineering Science, 54 (1999), 2433-2439

125. Dixon A.G., Nijemeisland, M., Stitt, E.H., CFD Simulation of reaction and heat transfer near the wall of a fixed bed, International Journal of Chemical Reactor Engineering, A22 (2003), 1

126. Nijemeisland, M., Dixon, A.G., CFD study of fluid flow and wall heat transfer in a fixed bed of spheres, American Institute of Chemical Engineers Journal, 50 (2004), 906-921

127. Nijemeisland, M., Dixon, A.G., Comparison of CFD simulations to experiment for convective heat transfer in a gas-solid fixed bed, Chemical Engineering Journal, 82 (2001), 231-246

128. Nijemeisland, M., Dixon A.G., Stitt, E.H., Catalyst design by CFD for heat transfer and reaction in steam reforming, Chemical Engineering Science, 59 (2004), 5185-5191

129. Dixon, A.G., Taskin, M.E., Stitt, E.H., Nijemeisland, M., 3D CFD simulations of steam reforming with resolved intraparticle reaction and gradients, Chemical Engineering Science, 62 (2007), 4963-4966

130. Dixon, A.G., Taskin, M.E., Nijemeisland, M., Stitt, E.H., Wall-to-particle heat transfer in steam reformer tubes: CFD comparison of catalyst particles, Chemical Engineering Science, 63 (2008), 2119-2224

131. Romkes, S.J.P., Dautzenberg, F.M., Bleek, C.M., Calis H.P.A., CFD modeling and experimental validation of particle to fluid mass and heat transfer in a packed bed at very low channel to particle diameter ratio, Chemical Engineering Journal, 96 (2003), 3-13

132. Guardo, A., Coussirat, M., Larrayoz, M.A., Recasens, F., Egusquiza, E., Influence of the turbulence model in CFD modeling of wall-to-fluid heat transfer in packed beds, Chemical Engineering Science, 60 (2005), 1733-1742

133. Guardo, A., Coussirat, M., Recasens, F., Larrayoz, M.A., Escaler, X., CFD study on particle-to-fluid heat transfer in fixed bed reactors: Convective heat transfer at low and high pressure, Chemical Engineering Science, 61 (2006), 4341-4353

134. Kalluri, Ranjeeth Raddy, Microfibrous entrapped catalysts and sorbents: Microstructured heterogeneous contacting systems with enhanced efficiency, PHD dissertation, College of engineering, Auburn University, Auburn, Alabama, US, 2008

135. Ravi Kuma, Computational fluid dynamics simulation of chemically reacting gas flows through microfibrous materials, PHD dissertation, College of engineering, Auburn University, Auburn, Alabama, US, 2008

136. Yang, J., Wang, Q., Zeng, M., Nakayama, A., Computational study of forced convective heat transfer in structured packed beds with spherical or ellipsoidal particles, Chemical Engineering Science, 65 (2010), 726-738

137. Scherrer, P., Göttingen Nachrichten, 2 (1918), 98

138. Fogler, H.S., Elements of Chemical Reaction Engineering, Prentice Hall, 2005

139. Dixon, A.G., An improved equation for the overall heat transfer coefficient in packed beds, Chemical Engineering and Processing, 35 (1996), 323-331

140. Perry, R.H., Green, D.W., Perry's Chemical Engineers's Handbook, 7th ed, The McGraw Hill, 1999

141. Mischke, R.A. and Smith, J.M., I&EC Fundamentals, 1 (1962), 288-292

142. Mears, D.E., Diagnostic criteria for heat transport limitations in fixed bed reactors, Journal of Catalysis, 20 (1971), 127-131

143. Philippe, R., Lacroix, M., Dreibine, L., Pham-Huu, C., Edouard, D., Savin, S., Luck, F., Schweich, D., Catalysis Today, 147s (2009), s305-s312

144. Kim, S., Bae, J.W., Lee, Y., Jun, K., Effect of CO_2 in the feed stream on the deactivation of Co/γ-Al_2O_3 Fischer-Tropsch catalyst, Catalysis Communication, 9 (2008), 2269-2273

Appendix A

A.1 Matlab codes to regress thermal parameters of transient case

```
clear
clc
N=40;
data=zeros(220,5);datacal=zeros(220,4);datacal2=zeros(220,4);
load transientdata.mat
dt=0.5;  %unit second
ker=1;
hw=134.2632;
iterNR=1;
avgdelta=100;
iterNRmax=100;
Terr=1;
deltamax=0.1;
while Terr>deltamax && iterNR<iterNRmax
 [datacal,point]=transientTem(data,N,dt,ker,hw);
 delta=0.001*ker;
 [datacal2,point]=transientTem(data,N,dt,ker+delta,hw);
  for i=1:(point-3)
  SenCoef(i,1)=(datacal2(i+2,2)-datacal(i+2,2))/delta;  %central point
  SenCoef(point-3+i,1)=(datacal2(i+2,3)-datacal(i+2,3))/delta;  %half radial point
  SenCoef(i+2*(point-3),1)=(datacal2(i+2,4)-datacal(i+2,4))/delta;  %3 quater point
  end
  delta=0.01*hw;
  [datacal2,point]=transientTem(data,N,dt,ker,hw+delta);
  for i=1:(point-3)
  SenCoef(i,2)=(datacal2(i+2,2)-datacal(i+2,2))/delta;  %central point
  SenCoef(point-3+i,2)=(datacal2(i+2,3)-datacal(i+2,3))/delta;  %half radial point
  SenCoef(i+2*(point-2),2)=(datacal2(i+2,4)-datacal(i+2,4))/delta;  %3 quater point
  end
%--Build normal equations
ST95=2.000 ;  % student's t-distribution for 0.975(95%) and n=60
```

```
R2=0;
Terr=0;
Aneq=zeros(2,2),;
    Bneq=[0,0]';
    VarData=0 ;
 for i=1:(point-3)
    Aneq(1,1)=Aneq(1,1)+SenCoef(i,1)*SenCoef(i,1)+SenCoef(point-
3+i,1)*SenCoef(point-3+i,1)+SenCoef(i+2*(point-2),1)*SenCoef(i+2*(point-2),1);
    Aneq(1,2)=Aneq(1,2)+SenCoef(i,1)*SenCoef(i,2)+SenCoef(point-
3+i,1)*SenCoef(point-3+i,2)+SenCoef(i+2*(point-2),1)*SenCoef(i+2*(point-2),2);
    Aneq(2,1)=Aneq(2,1)+SenCoef(i,2)*SenCoef(i,1)+SenCoef(point-
3+i,2)*SenCoef(point-3+i,1)+SenCoef(i+2*(point-2),2)*SenCoef(i+2*(point-2),1);
    Aneq(2,2)=Aneq(2,2)+SenCoef(i,2)*SenCoef(i,2)+SenCoef(point-
3+i,2)*SenCoef(point-3+i,2)+SenCoef(i+2*(point-2),2)*SenCoef(i+2*(point-2),2);



    Bneq(1)=Bneq(1)+(data(i+2,2)-datacal(i+2,2))*SenCoef(i,1)+(data(i+2,3)-
datacal(i+2,3))*SenCoef(point-3+i,1)+(data(i+2,4)-datacal(i+2,4))*SenCoef(i+2*(point-2),1);
    Bneq(2)=Bneq(2)+(data(i+2,2)-datacal(i+2,2))*SenCoef(i,2)+(data(i+2,3)-
datacal(i+2,3))*SenCoef(point-3+i,2)+(data(i+2,4)-datacal(i+2,4))*SenCoef(i+2*(point-2),2);
      Terr=Terr+(data(i+2,2)-datacal(i+2,2))^2+(data(i+2,3)-
datacal(i+2,3))^2+(data(i+2,4)-datacal(i+2,4))^2;
      VarData=VarData+(data(i+2,2)-datacal(i+2,2))^2+(data(i+2,3)-
datacal(i+2,3))^2+(data(i+2,4)-datacal(i+2,4))^2;
    end
    Aneq
    Bneq
    Delparms=Aneq\Bneq
VarData=VarData/((point-3-2))
AInv=inv(Aneq);
AInv=AInv*VarData
    Terr=(Terr/(3*(point-3)))^0.5
     fact=iterNR/(30+iterNR);
    ker=ker+Delparms(1)*fact
    hw=hw+Delparms(2)*fact
for i=1:2
    ConfIntv(i)=ST95*AInv(i,i)^0.5;
end
krstddevcalc=ConfIntv(1)/ker
hstddevcalc=ConfIntv(2)/hw
if ker<0
    ker=-ker;
end
```

```
if hw<0
   hw=-hw;
end
if hw>10^3
   hw=100;
end
   if ker~=0
   avgdelta=abs(Delparms(1)/ker);
   else
   avgdelta=abs(Delparms(1));
   end

   if hw~=0
   avgdelta=avgdelta+abs(Delparms(2)/hw);
   else
   avgdelta=avgdelta+abs(Delparms(2));
   end
   iterNR=iterNR+1
end


function [ datacal,Point ] = TransientTem(data,N,dt,ker,hw)
AA=zeros(N-1,N-1); T1=[1:1:(N-1)]';T0=[1:1:(N-1)]'; T=[1:1:(N+1)]';
r1=0.0182372; r2=0.01905; dr=r1/N;
kw=400;
vCu=data(1,1)/100;
vAl=data(1,2)/100;
void=1-vCu-vAl;
%PCp=vCu*7480*460+(void)*1.061354*1003.5; %steel with air
PCp=vCu*8960*292.48+vAl*715.8*880+(void+vAl*0.816)*1.067*1009;  %CU
%PCp=vCu*7990*502+vAl*715.8*880+(void+vAl*0.816)*1.067*1009; %S.S
%PCp=vCu*8912*444.2+vAl*715.8*880+(void+vAl*0.816)*1.067*1009; %Nickel
remd=ker/PCp;
Bi=hw*r1/ker;
Ak=remd*dt/dr^2;
%initial value
T(:)=(data(2,2)+data(2,3)+data(2,4))/3;
Twater=data(2,5);
tim=data(3,1);
Point=3;
tt=0;
while  tt<tim
tt=tt+dt;
for i=3:N-1
```

```
            AA(i-1,i-2)=(-1+1/(i-1)/2)*Ak;
            AA(i-1,i-1)=1+2*Ak;
            AA(i-1,i)=(-1-1/(i-1)/2)*Ak;
            T0(i-1)=T(i);
        end
        AA(1,1)=1+4/3*Ak;
        AA(1,2)=-4/3*Ak;
        T0(1)=T(2);
        AA(N-1,N-2)=Ak*(1/(N-1)/2-1+(1+1/2/(N-1))*(1+Bi*log(1+(r2-
r1)/r1)*ker/kw)/(2*Bi/N+3*(1+Bi*log(1+(r2-r1)/r1)*ker/kw)));
        AA(N-1,N-1)=1+2*Ak-Ak*(1+1/2/(N-1))*4*(1+Bi*log(1+(r2-
r1)/r1)*ker/kw)/(2*Bi/N+3*(1+Bi*log(1+(r2-r1)/r1)*ker/kw));
        T0(N-1)=T(N)+(1+1/2/(N-1))*Ak*Bi*Twater*2/N/(2*Bi/N+3*(1+Bi*log(1+(r2-
r1)/r1)*ker/kw));
        T1=AA\T0;
        T(2:N)=T1;
        T(1)=T(2)*4/3-T(3)/3;
        if tt>=tim
            Twater=data(Point,5);
            datacal(Point,:)=[tt,T(1),T(21),T(31)];
           Point=Point+1;
           tim=data(Point,1);
        end
        end
```

A.2 Matlab codes to regress thermal parameters of steady state case

```
clear
clc
global r1 r2 dr dz Twater Tin flowrate
T1=zeros(41,21); T0=zeros(41,21); Topt=zeros(4,150); Tdetail=zeros(4,10);% T1 new temperatures, T0 old temperatures,
SenCoef=zeros(8,3);
r1=0.0182372; r2=0.01905; l=0.0682625;
dr=r1/40; dz=l/20;
ii=3;
load steadystatedata.mat
flowrate=data(ii,1);
Texp=data(ii,2:14);
Tcheck=[Texp(2),Texp(3),Texp(4),Texp(5),Texp(7),Texp(8),Texp(9),Texp(10),Texp(11),Texp(12)];
poi=[1,1,1,1,21,21,21,21,31,31];
poj=[6,11,16,21,6,11,16,21,11,21];
Fac=[3,1,1,1,3,1,1,1,1,1];
ni=10;
Tin=Texp(1);
Tin2=Texp(6);
Tout=Texp(4);
Twater=Texp(10);
for j=1:21
   for i=1:41
      if i<21
   T1(i,j)=Tin+(Tin2-Tin)*(i-1)/20+(Tout-Tin)/20*(j-1);
      else
   T1(i,j)=Tin2+(Tout-Tin)/20*(j-1);
      end
end
end
T0(:,:)=T1(:,:);
ke0=0.5;
void=0.6317;
Dp=70.42; %um
keax=ke0+0.5*0.270374*10^(-6)*0.717*0.0286*flowrate*Dp/r1^2/(1-void);
ker=7.3;
keax=0.4179;
hw=500;
 Tdetail(7:16,1,ii)=Tcheck';
ST95=2.306 ;  % student's t-distribution for 0.975(95%) and n=10-2
```

```
 TT3=T0;
iterNR=2;
avgdelta=100;
iterNRmax=50;
deltamax=0.001;
while avgdelta>deltamax && iterNR<iterNRmax
   Aneq=zeros(2,2); Bneq=zeros(2)'; SenCoef=zeros(ni,3);
   TT3=T1;
   T1=Temp2(T0,ker,keax,hw);
   delta=0.001*hw;
   T2=Temp2(T0,ker,keax,hw+delta);
   for i=1:ni
   SenCoef(i,1)=(T2(poi(i),poj(i))-T1(poi(i),poj(i)))/delta;
   end
   delta=0.01*ker;
   T0=TT3;
   T2=Temp2(T0,ker+delta,keax,hw);
   for i=1:ni
   SenCoef(i,2)=(T2(poi(i),poj(i))-T1(poi(i),poj(i)))/delta;
   end
   delta=0.01*kex;
   T0=TT3;
   T2=Temp2(T0,ker,keax+delta,hw);
   for i=1:ni
   SenCoef(i,3)=(T2(poi(i),poj(i))-T1(poi(i),poj(i)))/delta;
   end
Terr=0;
 for i=1:ni
    Aneq(1,1)=Aneq(1,1)+Fac(i)*SenCoef(i,1)*SenCoef(i,1);
   Aneq(1,2)=Aneq(1,2)+Fac(i)*SenCoef(i,1)*SenCoef(i,2);
   Aneq(1,3)=Aneq(1,3)+Fac(i)*SenCoef(i,1)*SenCoef(i,3);
   Aneq(2,1)=Aneq(2,1)+Fac(i)*SenCoef(i,2)*SenCoef(i,1);
   Aneq(2,2)=Aneq(2,2)+Fac(i)*SenCoef(i,2)*SenCoef(i,2);
   Aneq(2,3)=Aneq(2,3)+Fac(i)*SenCoef(i,2)*SenCoef(i,3);
   Aneq(3,1)=Aneq(3,1)+Fac(i)*SenCoef(i,3)*SenCoef(i,1);
   Aneq(3,2)=Aneq(3,2)+Fac(i)*SenCoef(i,3)*SenCoef(i,2);
   Aneq(3,3)=Aneq(3,3)+Fac(i)*SenCoef(i,3)*SenCoef(i,3);
   Bneq(1)=Bneq(1)+Fac(i)*(Tcheck(i)-T1(poi(i),poj(i)))*SenCoef(i,1);
   Bneq(2)=Bneq(2)+Fac(i)*(Tcheck(i)-T1(poi(i),poj(i)))*SenCoef(i,2);
   Bneq(3)=Bneq(3)+Fac(i)*(Tcheck(i)-T1(poi(i),poj(i)))*SenCoef(i,3);
   Terr=Terr+(Tcheck(i)-T1(poi(i),poj(i)))^2;
   Tdetail(i+7,iterNR,ii)=T1(poi(i),poj(i));
   end
   Aneq
```

```
    Bneq
    Delparms=Aneq\Bneq
    Terr=(Terr/ni)^0.5
    fact=iterNR/(30+iterNR);
    ker=ker+Delparms(2)*fact
    kex=kex+Delparms(3)*fact
    hw=hw+Delparms(1)*fact
    VarData=0
for i=1:ni
    VarData=VarData+(Tcheck(i)-T1(poi(i),poj(i)))^2;
end
VarData=VarData/(ni)
AInv=inv(Aneq)
AInv=AInv*VarData
for i=1:3
    ConfIntv(i)=ST95*AInv(i,i)^0.5;
end
krstddevcalc=ConfIntv(2)/ker
kxstddevcalc=ConfIntv(3)/kex
hstddevcalc=ConfIntv(1)/hw
Tdetail(1:7,iterNR,ii)=[ker,krstddevcalc,keax,kxstddevcal,hw,hstddevcalc,Terr]'
if ker<0
    ker=-ker;
end
if hw<0
    hw=-hw;
end
if hw>10^3
    hw=100;
end
if ker~=0
avgdelta=abs(Delparms(1)/hw);
else
avgdelta=abs(Delparms(1));
end
    if hw~=0
    avgdelta=avgdelta+abs(Delparms(2)/ker);
    else
    avgdelta=avgdelta+abs(Delparms(2));
    end
    iterNR=iterNR+1
end
```

```
function [ T1 ] = Temp2(T0,ker,keax,hw)
global r1 r2 dr dz Twater Tin flowrate
T1=zeros(41,21);
alfar=ker/1299.789/1.8;
alfax=keax/1299.789/1.8;
biel=hw*r1/ker;
dt=0.25*dr^2/alfar;
remd=1;
vz=flowrate/60/1000/3.1415926/r1^2;  %m/s
kk=0;
error=1;
while error>=0.00001;
for i=2:40
    for j=2:20
        T1(i,j)=T0(i-1,j)*alfar*dt/dr^2*(1-1/2/(i-1))+T0(i,j-
1)*(alfax*dt/dz^2+remd*vz*dt/2/dz)+T0(i,j)*(1-2*alfar*dt/dr^2-
2*alfax*dt/dz^2)+T0(i+1,j)*(alfar*dt/2/(i-1)/dr^2+alfar*dt/dr^2)+T0(i,j+1)*(alfax*dt/dz^2-
remd*vz*dt/2/dz);
    end
 end
T1(1,:)=4*T1(2,:)/3-T1(3,:)/3;
for i=1:41
   T1(i,21)=  4/3*T1(i,20)-T1(i,19)/3; %Texp(5)+(Texp(8)-Texp(5))/15*(i-1); %
end
T1(41,:)=(biel*Twater*2/40+(4*T1(40,:)-T1(39,:))*(1+biel*ker/400*log(1+(r2-
r1)/r1)))/(2*biel/40+3*(1+biel*ker/400*log(1+(r2-r1)/r1)));
% for tubing wall
T1(1,1)=Tin;%
T1(:,1)=T0(:,1);
error=0;
for i=1:41
   for j=1:21
      error=error+(T1(i,j)-T0(i,j))^2;
   end
end
error=(error/41/21)^0.5;
kk=kk+1;
T0(:,:)=T1(:,:);
end
end
```